

NUMERICAL INVESTIGATION OF MICROWAVE  
SCATTERING FROM BREAKING  
WATER WAVE CRESTS

By

YANZHONG LI

Bachelor of Science

University of Electronic Science and Technology of China  
Chengdu, China  
1990

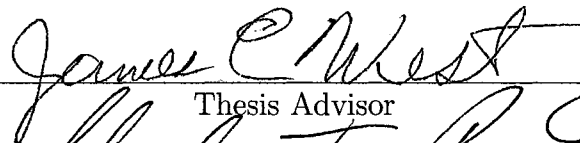
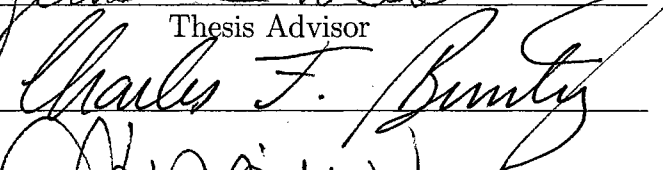
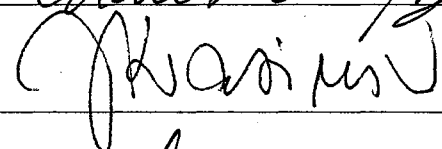
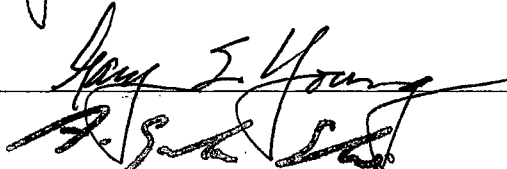
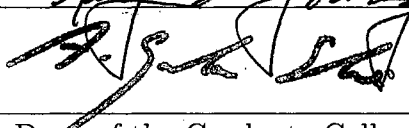
Master of Science

University of Electronic Science and Technology of China  
Chengdu, China  
1993

Submitted to the Faculty of the  
Graduate College of the  
Oklahoma State University  
in partial fulfillment of  
the requirements for  
the Degree of  
DOCTOR OF PHILOSOPHY  
May, 2005

NUMERICAL INVESTIGATION OF MICROWAVE  
SCATTERING FROM BREAKING  
WATER WAVE CRESTS

Thesis Approved:

  
\_\_\_\_\_  
Thesis Advisor  
  
\_\_\_\_\_  
  
\_\_\_\_\_  
  
\_\_\_\_\_  
  
\_\_\_\_\_  
Dean of the Graduate College

# Acknowledgments

I wish to extend my sincere gratitude to the individuals who assisted me in this research work and during my coursework at Oklahoma State University. In particular, I would like to express my appreciation to my advisor, Dr. James C. West, for his encouragement, guidance, inspiration and invaluable assistance over the last four years. He provided many helpful numerical routines and materials for this work. Dr. Zhiqin Zhao is also appreciated, this research is partially based on his work. I also wish to thank the other committee members, Dr. Keith A. Teague, Dr. Charles F. Bunting, Dr. Gary E. Young, and Dr. Jerzy S. Krasinski, for their many helpful suggestions and support during this effort.

This dissertation is dedicated to my beloved father Zunhe Li and my mother Zongyu Yuan, for their understanding and support during the long and difficult times that made my higher education possible. It is also dedicated to my parents-in-law, Zhenduo Wang and Xiuju Su. Thanks for their help, understanding and support. It is dedicated to my wife Yanrong and my daughter Hanming (Ellen), their unfailing love and encouragement have inspired me to reach this goal.

This work was supported by the U.S. Office of Naval Research through the Ship Structures and Systems S&T division under grant N00014-03-1-0134.

# Table of Contents

<b>1</b>	<b>Introduction</b>	<b>1</b>
1.1	Sea Spike Phenomena . . . . .	2
1.2	Theoretical Analysis of Surface Scattering . . . . .	4
1.2.1	Analytical Models and Numerical Techniques . . . . .	4
1.2.2	Test Surface Models . . . . .	6
1.2.3	Previous Work . . . . .	7
1.3	Study on Scattering from Breaking Wave Crests . . . . .	8
<b>2</b>	<b>Background</b>	<b>13</b>
2.1	Terminology . . . . .	13
2.2	LONGTANK Model Breaker Waves . . . . .	14
2.3	Surface Scattering Problem Definition . . . . .	15
2.4	Sea Surface Scattering Mechanisms . . . . .	17
2.5	Polarimetric Study . . . . .	21
<b>3</b>	<b>Review of Analytical Scattering Models</b>	<b>23</b>
3.1	Kirchhoff Approximation . . . . .	24
3.2	Small Perturbation Model . . . . .	24
3.3	Two-Scale Model for Deterministic Surfaces . . . . .	25
3.4	SSA and PPT . . . . .	28
3.5	Optical Models . . . . .	30
<b>4</b>	<b>Moment Method-based Numerical Techniques Review</b>	<b>33</b>
4.1	Preliminary Electromagnetic Theory . . . . .	34
4.2	Electromagnetic Field Integral Equations . . . . .	37
4.3	Moment Method for 2-D Scattering Problem . . . . .	39
4.4	Hybrid MM/GTD Technique . . . . .	42
4.5	RWG Vector Basis Function and 3-D MM . . . . .	44
4.5.1	RWG Vector Basis Function . . . . .	44
4.5.2	3-D Surface Moment Method . . . . .	46
4.6	Fast Multipole Method . . . . .	49

4.6.1	Introduction . . . . .	49
4.6.2	Element Grouping and Far Interaction Approximation . . . .	50
4.6.3	Physical Insight of FMM . . . . .	55
4.7	Multilevel Fast Multipole Algorithm . . . . .	57
4.7.1	Introduction . . . . .	57
4.7.2	Mathematical Derivation . . . . .	59
4.8	Surface Truncation and Edge Treatment . . . . .	61
4.9	Iterative Solver and Preconditioning . . . . .	63
4.10	Cube Element Grouping . . . . .	64
4.11	Test Case: Scattering from Impedance Flat Plate . . . . .	65
<b>5</b>	<b>Normal Backscattering Study</b>	<b>72</b>
5.1	Generation of 3-D Crest Test Surfaces . . . . .	73
5.2	2-D Scattering . . . . .	77
5.2.1	MM/GTD . . . . .	77
5.2.2	Prediction of EGO/GTD model . . . . .	78
5.3	3-D Crest Test Surface Scattering . . . . .	80
5.3.1	Backscattering . . . . .	80
5.3.2	The Relationship of 2-D and 3-D Backscattering . . . . .	82
5.3.3	3-D EGO Model . . . . .	84
5.3.4	Cross-section Curvature Effect on Scattering . . . . .	86
<b>6</b>	<b>Polarimetric Scattering</b>	<b>89</b>
6.1	Off-axis Backscattering from Surface 8 . . . . .	90
6.2	Off-axis Backscattering from Surface 12 . . . . .	92
6.3	Off-axis Backscattering from Surface 15 . . . . .	94
6.4	Off-axis Backscattering from Surface 18 . . . . .	95
6.5	Bistatic Scattering from Surface 12 and 18 . . . . .	99
<b>7</b>	<b>Backscattering from Multiple-jet Wave Crests</b>	<b>102</b>
7.1	Introduction . . . . .	102
7.2	Scattering Analysis of Multi-jet Wave Crests . . . . .	104
7.3	Scattering from Three-jet Crest Surfaces . . . . .	108
7.4	Scattering from Six-jet Crest Surfaces . . . . .	115
7.4.1	Jet Period . . . . .	115
7.4.2	Jet Magnitude . . . . .	116
7.5	Scattering from Series Multi-jet Surfaces with Identical Jet Features .	122
7.6	Scattering from Multi-jet Surfaces with Random-roughness Crests . .	128
<b>8</b>	<b>Summary and Conclusions</b>	<b>134</b>

# List of Figures

1.1	An example surface with multiple wave crests. . . . .	8
1.2	Illustration of the multiple reflection paths[1] . . . . .	9
2.1	Breaking wave surfaces generated by the LONGTANK hydrodynamic code (Full profiles). . . . .	14
2.2	Breaking wave surfaces generated by the LONGTANK hydrodynamic code (Expanded view of crests). . . . .	15
2.3	Surface scattering geometry in 3-D. . . . .	16
2.4	Bragg resonance principle. . . . .	18
2.5	Multipath reflection. Path $A - A_1 - A_2$ is ‘Single-bounce’ interactions; Path $B - B_1 - B_2 - B_3$ is ‘Double-bounce’ interactions; Path $C - C_1$ is the quasi-specular reflection. . . . .	20
2.6	Surface self-shadowing effect. Solid line is the incident ray; Dashed lines are the diffraction rays; Bold-faced section of the surface stands for the creeping waves. . . . .	20
4.1	Electromagnetic equivalence for finite conductivity scatter . . . . .	35
4.2	Scattering geometry of 2-D surface. . . . .	38
4.3	The approximation using piecewise constant subdomain functions. (a) Points and subdomains on the surface. (b)Pulse function. (3) Current approximation using pulse basis function. . . . .	41
4.4	Infinity edge extension in MM/GTD technique. . . . .	42
4.5	Triangular patch surface meshing. . . . .	44
4.6	Triangular pair associated with RWG basis function definition. . . . .	45
4.7	Vector relationship among elements and groups. . . . .	51
4.8	Relationship between vector $\mathbf{r}'$ , $\mathbf{r}$ , $\mathbf{x}$ and $\mathbf{d}$ . . . . .	51
4.9	Two levels structure in FMM technique. . . . .	58
4.10	Upward tree multilevel structure in MLFMA technique. . . . .	58
4.11	Illustration of 2-D resistive loading. . . . .	63
4.12	Demonstration of the cube grouping scheme. . . . .	65
4.13	The truncated flat sea surface. . . . .	66

4.14	Current distribution on the flat impedance plate with resistive edge loading . . . . .	67
4.15	Current distribution on the flat impedance plate with no resistive edge loading. . . . .	67
4.16	RCS of normal backscattering from the flat plate. . . . .	68
4.17	Off-axis backscattering RCS distribution. . . . .	69
4.18	Bistatic scattering RCS distribution of the flat plate. . . . .	70
4.19	Contours of the bistatic scattering RCS of the flat plate. . . . .	71
5.1	Pre-processed LONGTANK case 2.4 profiles. . . . .	74
5.2	Demonstration of the 3-D crest surface formation. . . . .	75
5.3	Test 3-D surfaces with various crest features . . . . .	76
5.4	Backscattering RCS of 2-D surfaces (MM/GTD) . . . . .	78
5.5	Backscattering of the 18 LONGTANK profiles (MM/GTD) [2]. . . . .	79
5.6	Geometry for reflection and diffraction by a crest structure. . . . .	79
5.7	EGO/GTD prediction of the backscattering from the 18 LONGTANK profiles (repeated from [2]). . . . .	80
5.8	Normal backscattering RCS of 3-D test surfaces (MLFMA) . . . . .	81
5.9	Comparison of synthesized 3-D RCS with MLFMA results. . . . .	83
5.10	Automatically searched reflection points when $\delta \leq 2^\circ$ . . . . .	85
5.11	Equivalent reflection points and their cross-section curves. . . . .	85
5.12	Comparison the 3-D EGO results with the reference of MLFMA. . . . .	86
5.13	The cross-section cut lines at reflection points. . . . .	87
5.14	The backscattering RCS of compressed surface 12. . . . .	87
6.1	RCS of off-axis backscattering from surface 8. . . . .	90
6.2	Position variation of specular reflection points on surface 8 . . . . .	91
6.3	RCS of off-axis backscattering from surface 12. . . . .	92
6.4	Position variation of specular reflection points on surface 12 . . . . .	93
6.5	RCS of off-axis backscattering from surface 15. . . . .	95
6.6	Position variation of specular reflection points on surface 15 . . . . .	96
6.7	RCS of off-axis backscattering from surface 18. . . . .	97
6.8	Position variation of specular reflection points on surface 18 . . . . .	98
6.9	Illustration of destructive interference mechanisms . . . . .	99
6.10	RCS of bistatic scattering from surface 12. . . . .	100
6.11	RCS of bistatic scattering from surface 18. . . . .	101
7.1	Interpolated LONGTANK case 2.4 profiles (11 to 18). . . . .	103
7.2	Illustration of the creation of multi-jet surface crests. . . . .	104
7.3	Multi-jet surfaces with marked reflection points ( $\delta \leq 4^\circ$ ). . . . .	105

7.4	RCS of backscattering from multi-jet surfaces. . . . .	106
7.5	3-D EGO results of multi-jet surfaces. . . . .	107
7.6	Illustration of 3-jet surface (Reference profile 13/12.5). . . . .	109
7.7	Illustration of reflection points on crest jets and in cavity regions. . .	109
7.8	Illustration of 3-jet surface (Reference profile 18/17). . . . .	110
7.9	Illustration of 3-jet surface (Reference profile 16/14). . . . .	111
7.10	Reflection points on the 2-jet surface in Figure 7.9(b) at different inci- dent angles. . . . .	112
7.11	Illustration of 3-jet surface (Reference profile 18/16). . . . .	113
7.12	Reflection points on the 2-jet surface in Figure 7.11(b) at different incident angles. . . . .	114
7.13	Six-jet surfaces (Ref. profile 13/12) with different jet period. . . . .	115
7.14	Six-jet surfaces (Ref. profile 18/17) with different jet period. . . . .	117
7.15	Six-jet surfaces (Ref. profile 13 at jet centers) with different ripple feature. . . . .	118
7.16	Comparison of the scattering from section A and C respectively. . .	119
7.17	Six-jet surfaces (Ref. profile 18 at jet centers) with different ripple feature. . . . .	120
7.18	Comparison of the scattering from section A and C respectively. . .	121
7.19	Series surfaces (Ref. profile 13/12) with identical jet size and period. .	123
7.20	RCS comparison of backscattering from multi-jet surfaces. . . . .	123
7.21	Series surfaces (Ref. profile 18/16) with identical jet size and period .	124
7.22	Reflection points on the 2-jet surface, at different incident angles. . .	125
7.23	Reflection points on the 4-jet surface, at different incident angles. . .	126
7.24	Illustration of the difference between the two synthesis procedures. .	126
7.25	Scattering from section A, B, and D respectively. . . . .	127
7.26	Comparison of 'B' and 'D' based synthesized scattering with MLFMA scattering. . . . .	128
7.27	Random-roughness crest surfaces (smooth) . . . . .	129
7.28	RCS of scattering from random-roughness crest surfaces (smooth) . .	130
7.29	Random-roughness crest surfaces (rough) . . . . .	131
7.30	RCS of scattering from random-roughness crest surfaces (rough) . . .	132



# Chapter 1

## Introduction

Great interest in the scattering of microwave signals from random rough surfaces began in World War II. Understanding of rough surface scattering has applications to remote sensing, oceanography, communications, material science, and optics. Microwave frequency scattering from the sea surface is of particular interest since it appears as clutter which can mask the target signals. Understanding the surface scattering process will aid in the development of methods to detect target signals from within the clutter. On the other hand, the sea surface scattering itself is the signal in remote sensing applications. The backscattering is correlated with meteorological and oceanographic conditions such as wind speed, wave state, and temperature. Understanding of the scattering mechanisms facilitates the extraction of oceanography and meteorology conditions from the measured scattering [3] [4] [5] [6] [7].

Sea surface backscattering is reasonably well understood when the radar wave is incident on the surface at moderate incidence angles ( $30^\circ - 60^\circ$ ). The scattering is dominated by the Bragg scattering mechanism in this region [8]. However as the incidence approaches grazing, the backscattering shows different characteristics. In particular, it is characterized by brief bursts of backscattering known as “sea spikes” [9]. Several scattering mechanisms have been proposed as the cause of sea spikes [10][11][12][13][14][15]. One of the most successful models is the back-reflection from

breaking waves [11][16]. The direct and multipath quasi-specular reflections from the overturning crest and the front face of breaking waves were thought to be an important factor to cause sea spike phenomena [14][2]. Studying on the mechanisms that lead to sea-spike scattering from breaking wave crests is the subject of this paper.

## 1.1 Sea Spike Phenomena

Bursts of strong backscattering often dominate the radar returns from sea surface when the incidence approaches grazing. This is termed the sea-spike phenomenon [17][18][19]. The target detection and tracking performance of high resolution radars is seriously affected by the sea spikes as strong radar clutter. Therefore, the efforts on clutter cancellation require good understanding of sea spike scattering mechanisms. When looking upwave, the horizontally polarized (HH: transmit/receive) backscattering differs from the vertically polarized (VV) backscattering by being sharper, spikier, and more intermittent [20][21][22][23]. Sea-spike returns can give HH scattering cross-sections up to 10 dB greater than the corresponding VV cross sections. This behavior usually is termed a “super event”.

The practical radar experiments usually provided upwave looking backscattering from real sea surfaces. The experimental data showed that VV’s sensitivity to surface features such as the small waves (ripples) associated with the wind-dependent fine structures of the sea, and HH’s sensitivity to surface features such as smooth reflecting surfaces (facets) associated with sharp wave crests (wedges) [23]. However, the conditions under which the experiments are performed cannot be controlled. The reliable ground truth measurements of the scattering surface are extremely difficult to obtain. Also, it is difficult to clearly identify the involved physical scattering mechanisms from the radar experimental results due to lots of surface features being included in its large observation view. Some laboratory test radar systems were developed to measure the backscattering from the water tanks which were specially designed to generate spe-

cific wave features [24][25][26]. Although the laboratory experiments were helpful to recognize the scattering mechanisms, they were expensive and inflexible compared with theoretical analysis using analytical models or numerical simulations.

Various analyses have been attempted to explain sea spike phenomena and the polarization-dependent contrast between VV and HH upwave backscattering (super event). Bragg resonance [27] is believed to be the mechanism which leads to strong backscattering from electromagnetically small-scale roughness surface at low grazing incidence. However, standard Bragg theory can not explain sea-spike phenomena, particularly when super-events occur. Experimental studies [27] have shown a correlation between sea spikes and wave breaking. Quasi-specular reflection from breaking waves was believed to be a major contributor to the backscattering at grazing incident angles [11][16]. On the other hand, as Trizna [15] pointed out, the different decorrelation times of the horizontal polarization and vertical polarization sea spikes suggests different sources of scattering for HH and VV. Several models have been presented to describe sea-spike scattering mechanism, such as wedge diffraction from steep wave crests [10], specular reflection from overturning waves [11][12], bounded and tilted Bragg-resonant waves on the crest of waves [13], and the interference of multipath scattering from the steep crest and tilted wave face [14] (including Brewster angle damping of the vertically polarized reflection from the wave face [15]). West's numerical backscattering from LONGTANK model wave crests indicated that the interference between the reflections from the convex and concave reflection points on an overturning wave crest can also lead to super events [2].

## 1.2 Theoretical Analysis of Surface Scattering

### 1.2.1 Analytical Models and Numerical Techniques

Generally speaking, theoretical scattering investigation includes the development of both analytical models and numerical simulation methods. Existing analytical models include the Kirchhoff approximation (KA) [8], the small-perturbation model (SPM) [28], the two-scale mode (TSM) [29], the small slope approximation (SSA) [30][31], and the phase perturbation technique (PPT) [32][33][34][35] etc. Analytical scattering theories are of great importance since they not only show how the variation of surface parameters will affect scattering behavior, but also provide physical insight that may not be available from experimental data alone. However, the approximations inherent in the development of the models lead to relatively strict application conditions. To overcome this limitation, numerical methods have been developed. The popularity of numerical methods has increased with the improvements of computer technology.

Numerical methods include both differential equation methods (DEM) and integral equation methods (IEM). As implied, DEM methods solve Maxwell's equations directly in differential form, usually yielding the electromagnetic fields directly. Typical examples are the finite difference time domain method (FDTD) [36] and the finite-element method (FEM) [37][38][39]. As a time domain method, FDTD has an advantage of directly obtaining broadband information about the scattering properties of a surface. However, to obtain the far scattered fields, a near- to far-field transformation must be employed since the fields are only available directly in the region of discretization [40]. FEM is well suited to inhomogeneous problems with complex geometries [37][38][39]. FEM requires the solution of a linear system with a sparse matrix. As with FDTD, special treatments must be used to find the far-field scattered fields away from the surface region [41][42][43][37]. The artificial mesh truncation (boundary) condition is an inherent problem for these techniques when

treating the scatterers with open geometries. Also, a drawback common to all DEM methods is the grid dispersion error incurred [44][45][46]. For example, in FDTD applications, the grid dispersion error causes a wave to have an incorrect phase velocity on a grid. This is a severe limitation for computation over large scatterers because the dispersion error is cumulative. The dispersion error can be suppressed using a higher grid density or choosing a higher order solver [47][48]. However, both measures will lead to higher computation cost.

IEM methods solve an equivalent integral equation representation of the fields. The moment method (MM) is the most common IEM technique, which is based on the electromagnetic equivalence theorem. The equivalent surface currents are the direct solutions of an IEM solver. The far scattered fields are then obtained through the radiation principle. An MM treatment of the field integral equation leads to a dense matrix system that must be solved. Direct solution of the linear system is of order  $O(N^3)$ , where  $N$  is the number of unknowns to be found. Iterative solution of the system can reduce the operation count to  $O(N^2)$ . However, the computation cost of even iterative solution is very high when a large surface scattering problem is solved. The required matrix-vector multiplies are the major computation load of an iterative solution. Therefore, algorithms to accelerate the matrix-vector multiply have been developed, including the fast multipole method (FMM) [49][50][51], the multi-level fast multipole algorithm (MLFMA) [52][53][54], the fast steepest descent path algorithm (FASDPA) [55][56], and the adaptive integral method (AIM) [57]. These acceleration methods improve the order of the MM solution stage to as low as  $O(N \log^2 N)$ , thus giving very efficient tools for large surface scattering computation. In practical applications, the MM-based solutions usually are thought of as the “exact” reference used to verify the validity of the analytical models.

### 1.2.2 Test Surface Models

Initial analytical studies of rough surface scattering focused primarily on single-valued surfaces derived from linear wave spectra. These are, in some sense, an approximation of the true ocean surface when a valid spectrum is used. Sample surfaces are easily generated using standard Fourier techniques. A popular wave spectrum is that introduced by Pierson and Moskowitz [58]. It is superior to the simpler Gaussian and power-law spectra that were previously used in that it accounts for wind speed. Analytical models may be formulated to give a statistical representation of the field scattered from a typical wave spectra, or the deterministic field associated with a particular sample surface. In the latter case, the statistics are estimated using the Monte-Carlo method applied to the fields scattered from the individual surfaces over an ensemble of realizations [59] [60]. Numerical methods only yield deterministic fields, so Monte-Carlo methods must be used. As the ensemble size increases, the results should converge to a desired statistical moment [61]. Note that since the individual sample surfaces are independently generated, the fields scattered from them are incoherent.

Recently, both analytical and numerical scattering models have been applied to non-linear, multivalued surfaces that were obtained through numerical hydrodynamic models [62] and direct measurement [63]. These non-linear surfaces typically provide a time-history of the wave evolution. The coherent fields scattered from these surfaces can therefore be used to find the Doppler shift in the backscatter. Moreover, the multivalued nature of the surfaces allow the prediction of quasi-specular back-reflection from steep and overturning features that are absent from linearly generated surfaces. These are thought to be particularly important at low-grazing angle illumination. The non-linear surfaces (both measured and generated) therefore provide a more realistic representation of the scattering.

### 1.2.3 Previous Work

Considerable work has previously been performed at Oklahoma State University addressing rough surface scattering, particularly focusing on the breaking wave scattering mechanism. A series of moment method (MM)-based numerical scattering codes have been implemented. These include a periodic surface solver MM [64] and a hybrid MM/GTD technique [65][66][65] for 2-D scattering, and a multilevel fast multipole algorithm (MLFMA) [67][68] technique for 3-D scattering. Special surface treatments were developed for application of these techniques to rough surfaces. For example, the application of the impedance boundary condition to both the electric field integral equation (EFIE) and the magnetic field integral field (MFIE) reduces the computational load when treating finite conductivity surfaces [69][70]. Edge extension of the surface was used with MM/GTD to suppress artificial edge diffraction from the modeled surface [71]. Resistive loading of the edges has also been implemented to control edge diffraction [1] [72]. Numerous numerical preconditioners have been implemented to accelerate the convergence of iterative solution methods. The numerical codes have been applied to several different types of surfaces, including random rough surfaces generated from linear roughness spectra [1], breaking wave histories generated from numerical hydrodynamic codes [70][73][2][1], and measured plunging and spilling breaker waves [74]. The validity of analytical models and scattering mechanisms has been discussed through comparison of the results of analytical models with the numerical “exact” results. Limitations of the standard two-scale model when surface self-shadowing occurs was identified [75]. Multi-path scattering was modeled using ray-optical techniques [76][1]. The scattering from breaking jets was modeled using an extension of geometrical optics [2]. Finally, the time dependence of the Doppler shift of the backscattered fields from crests was used to identify the “fast” and “slow” scattering mechanisms [74]. Overall, the work has focused on characterizing the limitations of classical approximate scattering models, and identifying and modeling the

scattering mechanisms for breaking waves.

### 1.3 Study on Scattering from Breaking Wave Crests

As mentioned before, strong sea spikes always appear in radar returns at low grazing angle, and are typically associated with breaking waves. The complicated backscattering is therefore due to a combination of various scattering mechanisms such as quasi-specular reflection, multipath scattering with Brewster angle dumping effect, and distributed-surface roughness. An example situation is shown in Figure 1.1, which represents a radar resolution cell in which several crests are breaking. The scattering from the entire surface may include direct quasi-specular back-reflection from individual jets, and also be affected by the multipath reflection between a jet and other surface points. Due to the complexity of the scattering process, predicting the backscattering is very difficult even when the exact scattering surface is known. Analytical models are formulated with approximations that limit their application to specific classes of surface features. For example, the Kirchhoff approximation can only be applied to surfaces where the radius of curvature is large compared to a radar wavelength, and distributed-roughness models assume single-valued surfaces that do not introduce multipath. As the sea surface includes features of all these types, no analytical model can alone predict the full scattered signal. On the other

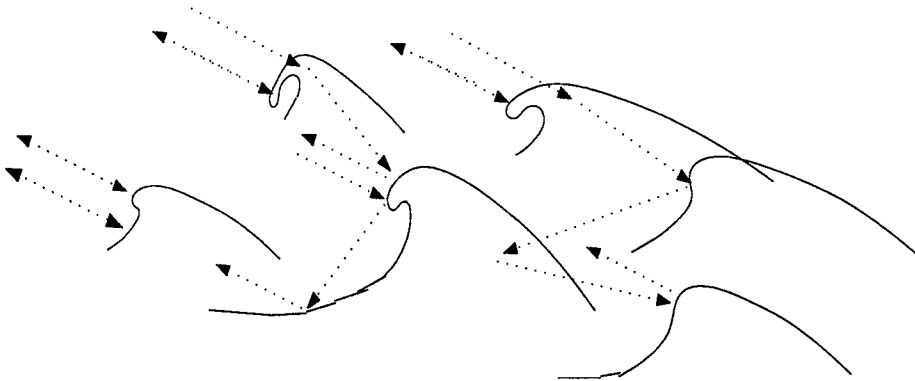


Figure 1.1: An example surface with multiple wave crests.



hand, numerical methods can treat any surface features simultaneously. However, computational resources greatly limit the size of the surface that can be modeled. It therefore is not possible to model full radar resolution cells at one time.

In stead of attempting to model the full surface simultaneously, a typical approach is to model individual scattering mechanisms separately with appropriate models. The results of each model can then be appropriately combined to predict the entire signal. This approach obviously requires that both the individual mechanisms and appropriate models be identified. Previous work toward this goal has been performed at Oklahoma State University. Figure 1.2 shows the two-dimensional wave profiles that were considered by West and Zhao[1]. Shown in part (a) is the direct quasi-specular back reflection, as well as a multipath reflection from the crest of the wave to the front face, and then back to the radar. Part (b) shows the multipath from the front face to the crest, back to the front face, and then to radar. West and Zhao analyzed these waves by isolating the crest scattering from the multipath by truncating the surface as show by the long-dashed line. The bi-static crest scattering was then found using the MM/GTD numerical techniques. This yielded the quasi-specular back reflection as well as the fields scattered toward the front face. The multipath effects were then included by applying the physical optics approximation to the scattered front-face field, and radiating the PO current to yield the single-

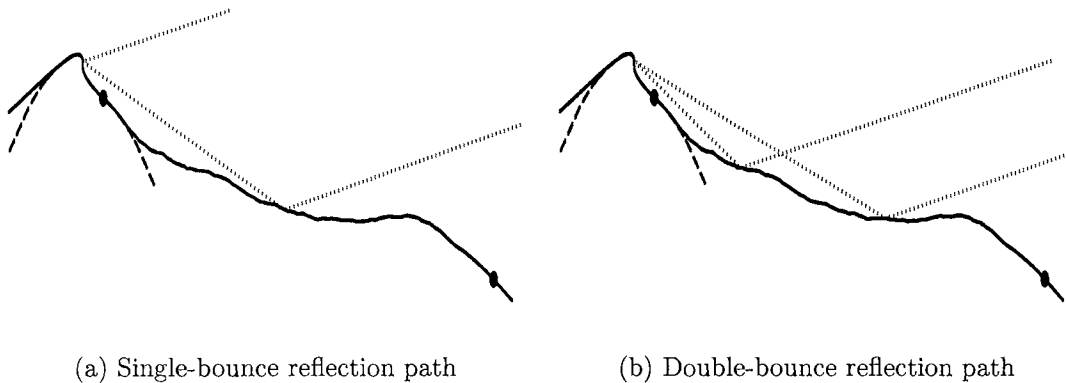


Figure 1.2: Illustration of the multiple reflection paths[1]

bounce multipath signal. Two consecutive applications of PO yielded the double-bounce multipath signal. Coherent addition of the direct and multi-path signals yielded scattering cross-sections that agree very well with those given by MM/GTD when applied to the full wave surface. Recently, experimental confirmation of the scattering mechanisms has been achieved [26]. The scattering from several waves can be coherently added to model the scattering from a full radar resolution cell.

The work of West and Zhao was limited to two-dimensional wave profiles that were uniform in the azimuthal direction. The results were therefore limited to up-wave/downwave looking scattering and cannot predict cross-polarized scattering. The breaking-wave scattering therefore is not fully modeled. It is therefore desirable to extend the techniques of West and Zhao to the full 3-D problem. Due to the complexities of the 3-D surfaces, it will be considerably more difficult to accurately represent the crest scattering even in the absence of multipath effects. The azimuthal non-uniformities of the crests lead to several scattering mechanisms. Thus, this paper will focus on understanding the 3-D wave crest scattering. MLFMA will be used to provide reference scattering from the crest. This will predict all scattering effects, including arbitrary azimuth and elevation illumination direction and cross-polarized scattering. The MLFMA scattering will then be compared to the analytical scattering model results to identify the scattering mechanisms. The multiple scattering points on single crests will also be isolated and characterized using geometrical optics. Ultimately, it is expected that the results will be combined with a 3-D multipath model.

Sample crests will be derived from the numerically generated LONGTANK series of 2-D profiles representing the time-evolution of a 1 m wavelength breaking wave. Each LONGTANK profile has a different crest shape which describes a specific stage of the wave formation. The scattering analysis begins by using the existing MM/GTD method to calculate the backscattering from each 2-D profile. This gives general

insight to the backscattering features of the sample two-dimensional profiles. The LONGTANK profiles are used to synthesize 3-D test surfaces. MLFMA using resistively loaded edges is used to find the scattering from these surfaces. The relationship between the original LONGTANK profile scattering and the 3-D surface scattering is then discussed. In particular, the effects of the radius of curvature of the wave in the azimuthal dimension on the Fresnel interference between the back-reflections from the jet and cavity region are considered. The 3-D extended geometrical optics (EGO) model is then applied on a test crest surface in order to verify the scattering mechanism.

Simple single-jet 3-D test surfaces based on LONGTANK model are first analyzed. The scattering from this type of surface is generally dominated by the reflection from a few specular points. In particular, super events may occur when the back-reflections from the convex jetting region of the surface and the concave cavity region under the jet interfere constructively at HH but destructively at VV, provided that the surface radii of curvatures at the specular reflection points are somewhat smaller than the electromagnetic wavelength [2]. For more complex wave crest cases, however, several jets may exist simultaneously, and the scattering phenomena will become more complicated. The interference between the back-reflections from many different jets or cavity regions between jets may play a significant role under specific geometrical conditions. Some 3-D multiple-jet test surfaces are also synthesized using the LONGTANK profiles, including the crests with multiple identical jet structures and the crests with random-jet ripples. The scattering from individual jet regions and the multiple interactions between different jet regions will be considered based on the associated computational results.

In Chapter 2, background material regarding the scattering geometry, breaking wave surfaces, scattering mechanisms, and polarimetric description of scattering is introduced. Chapter 3 gives a summary of the traditional analytical models used

for surface scattering analysis. In Chapter 4, the numerical techniques to be used are reviewed, including MM, MM/GTD, FMM, and MLFMA. The surface edge extension approaches and the resistive loading technique are also reviewed, which are applied in these numerical techniques to eliminate unexpected multipath reflections and attenuate the diffraction from surface edges. The scattering from a flat plate test case is then used to confirm the validity of the numerical routines. The analysis of the scattering from the 2-D LONGTANK model profiles, and synthesized single-jet 3-D crest test surfaces when looking upwave is given in Chapter 5. In Chapter 6, the scattering when looking away from the upwave direction is examined. Both monostatic and bistatic cases are considered. Various multiple-jet wave crests are synthesized in Chapter 7, the backscattering from these complex multiple-jet surfaces is then examined.

# Chapter 2

## Background

This chapter explains the terminologies and concepts used in this paper. First the breaking wave surfaces used to develop test cases are introduced, which are the breaking-wave series generated by the LONGTANK hydrodynamic code. This is followed by a description of the surface scattering geometry. Then known sea surface scattering phenomena and scattering mechanisms are summarized, including Bragg scattering, quasi-specular reflection, multipath reflection, and the surface self-shadowing effect. The concept of polarimetric scattering also is introduced.

### 2.1 Terminology

Historically, numerical treatment of rough surface scattering was first applied to surfaces that were uniform in the azimuthal dimension. This allows a two-dimensional (2-D) electromagnetic problem to be solved, which is computationally much less expensive than the 3-D problem. When single valued surfaces are considered, the roughness displacement for these surfaces can be expressed by  $z = f(x)$ , leading to the terminology “one-dimensionally rough” surface. Single-valued surfaces that are not azimuthally uniform may be described by  $z = f(x, y)$ , leading to the terminology “two-dimensionally rough”. This terminology is not meaningful for multivalued sur-

faces that cannot be described by a functional dependence. Instead, a terminology is adopted based on the order of the electromagnetic problem that must be solved. The 2-D problem treats surfaces that are uniform in one dimension, giving a 2-D scattering cross-section [77]. The 3-D problem, with a corresponding 3-D cross-section, is applied to the most general surfaces that have no assumption of uniformity.

## 2.2 LONGTANK Model Breaker Waves

The LONGTANK wave series to be used was generated numerically using a computational hydrodynamics technique by Wang *et al.* [62]. The LONGTANK code was developed to study wave groups, wave-wave interactions, wave deformation, wave breaking, and other nonlinear effects. The generated wave shapes are consistent with tank experiments and ocean observations. The case 2.4 series represents the temporal evolution of 2.3 m wavelength sea wave. The peak wave in the group, which is in the deformation phase of wave breaking, is followed for a time interval (180 ms) beginning close to the inception of the breaking process and ending with jet initiation at the crest of the wave. The first numerical study of the backscattering from this wave series was performed by Holliday *et al.* [78]. Figure 2.1 shows the 18 profiles in the case 2.4 series. Figure 2.2 shows an expanded view of the crests. Wave 1 shows some

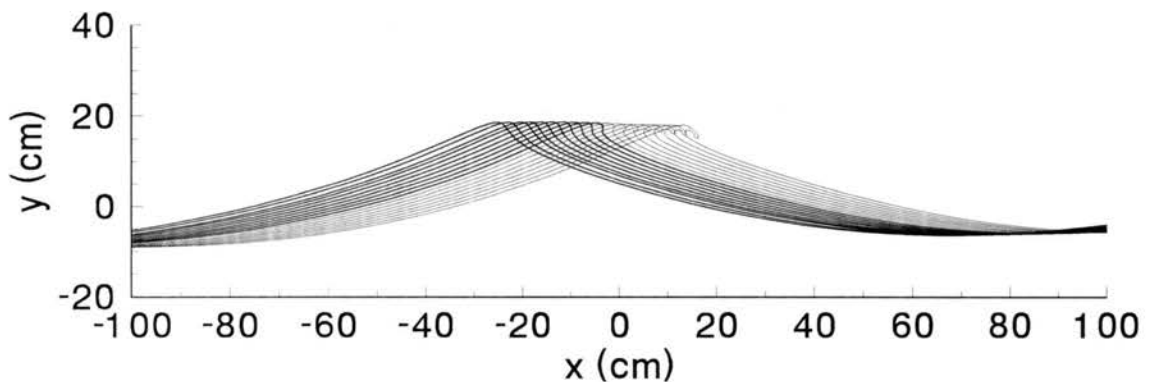


Figure 2.1: Breaking wave surfaces generated by the LONGTANK hydrodynamic code (Full profiles).

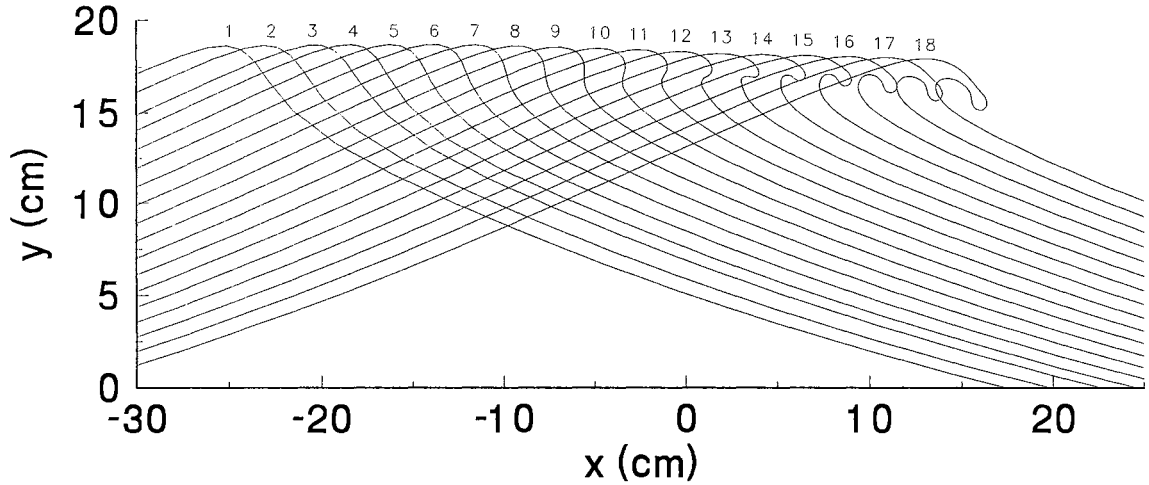


Figure 2.2: Breaking wave surfaces generated by the LONGTANK hydrodynamic code (Expanded view of crests).

steepening, while wave 12 shows the initial jet formation. The jetting and overturning occurs in wave 13 through 18. These profiles have been used in several electromagnetic studies [78][2], and have become a standard test for breaking-wave scattering studies.

## 2.3 Surface Scattering Problem Definition

Scattering takes place when an electromagnetic (EM) wave propagates and impinges on a target surface with constitutive properties that differ from that of the incident medium. The target is termed the scatterer. The three-dimensional scattering geometry is shown in Figure 2.3. In this figure,  $\mathbf{k}_i$  and  $\mathbf{k}_s$  are the incident and scattering direction vectors respectively,  $(\theta_i, \phi_i)$  give the elevation and azimuthal angles to the transmitter (incident source), while  $(\theta_s, \phi_s)$  correspond to the receiver direction (observation point).  $\mathbf{v}_i$  and  $\mathbf{h}_i$  are unit vectors in the vertical and horizontal directions along the incident wave direction. Similarly,  $\mathbf{v}_s$  and  $\mathbf{h}_s$  are the vectors along the scattered wave direction. Also,  $\mathbf{v}_r$  and  $\mathbf{h}_r$  give the vectors at the receiver antenna. The polarization of an EM wave is defined according to the direction of its electric field. If the electric field is perpendicular to the plane of incidence containing the

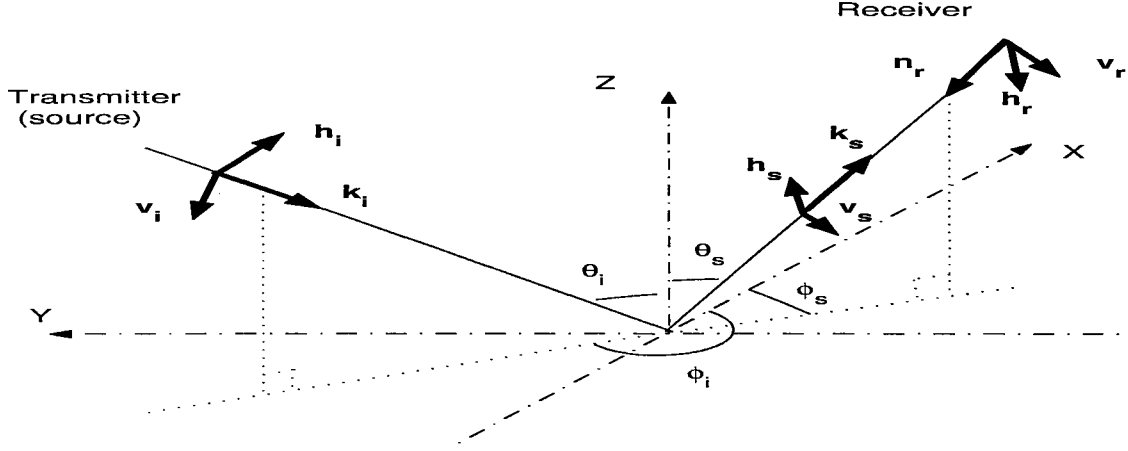


Figure 2.3: Surface scattering geometry in 3-D.

direction of propagation of the field and the mean surface normal, the polarization is termed horizontal (H-pol). The polarization is vertical (V-pol) if the electric field lies in the plane of incidence. In a scattering analysis, the polarization of the incident and scattered fields are usually to be specified together by **HH**, **HV**, **VH**, and **VV**. The first letter denotes the polarization of the incident field, and the second letter denotes the polarization of the scattered field. **HH** and **VV** give co-polarized scattering at horizontal and vertical polarization, while **HV** and **VH** give the cross-polarization scattering. When the scattering is treated as a 2-D electromagnetic problem (uniform in one dimension), no cross-polarized scattering is generated. Therefore, to observe the cross-polarization phenomena, the 3-D scattering problem must be solved.

The radar cross-section (RCS) is the equivalent area that intercepts the amount of incident power that when scattered isotropically produces the same power density at the receiver as that scattered by the actual scatterer. In a 2-D electromagnetic analysis, the RCS is defined by [77]

$$\sigma_{2-D} = \lim_{\rho \rightarrow \infty} \left[ 2\pi\rho \frac{|\mathbf{E}^s|^2}{|\mathbf{E}^i|^2} \right], \quad (2.1)$$

where  $\rho$  is the distance between scatterer and receiver, and the  $\mathbf{E}^i$  and  $\mathbf{E}^s$  are the



incident and scattered field respectively. The 3-D RCS is

$$\sigma_{3-D} = \lim_{r \rightarrow \infty} \left[ 4\pi r^2 \frac{|\mathbf{E}^s|^2}{|\mathbf{E}^i|^2} \right], \quad (2.2)$$

where  $r$  is the distance from scatterer to observation point. Note that (2.2) is polarization-dependent for 3-D surface scattering, which is decided by the polarization of the electric fields  $\mathbf{E}^i$  and  $\mathbf{E}^s$ . When the transmitter and receiver are co-located, the scattering is usually called backscattering, and the RCS is referred to as monostatic. The RCS is bistatic when the source and the observation point are at different locations. Scattering when the observations follow the direction that locally satisfies Snell's law of reflection is usually referred to as specular reflection.

## 2.4 Sea Surface Scattering Mechanisms

Sea-spike and super-events described in previous chapter are common scattering phenomena in breaking wave backscattering analysis when low grazing angle (LGA) incidence occurs. Several mechanisms have been identified as potential contributors to sea surface backscattering.

### • Bragg Scattering

Bragg scattering is a rough surface scattering phenomenon whose physical mechanism is similar to that of the Bragg resonance x-ray scattering from a crystal lattice. As shown in Figure 2.4, Bragg backscattering comes from the portion of the 2-D surface with a surface wavelength  $\Lambda$  such that  $2\Lambda \sin \theta_i$  is equal to an electromagnetic wavelength  $\lambda$  (or integer multiples of  $\lambda$ ). The resonance may be expressed by the Bragg condition

$$K = 2\pi/\Lambda = 2k \sin \theta_i, \quad (2.3)$$

where  $K$  is the Bragg-resonant surface wave number,  $k = 2\pi/\lambda$  is the radar wave number and  $\theta_i$  is the incident angle. For a general bistatic 3-D surface case, the

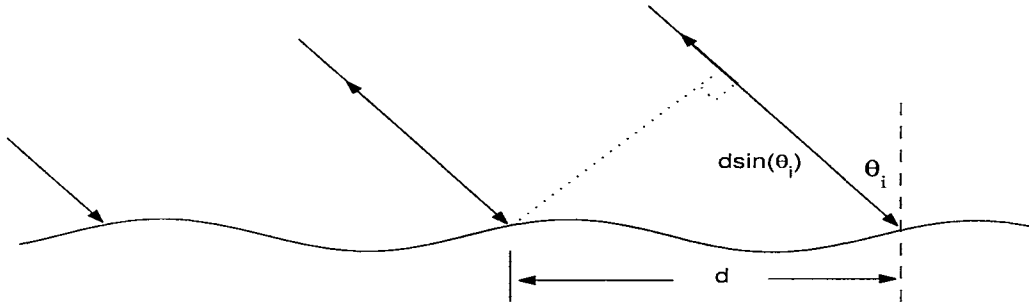


Figure 2.4: Bragg resonance principle.

Bragg-resonant surface wave number in x and y direction can be written as

$$\begin{aligned} K_x &= k \sin \theta_s \cos \phi_s - k \sin \theta_i , \\ K_y &= k \sin \theta_s \sin \phi_s . \end{aligned} \tag{2.4}$$

Note that the round trip scattering from the crests of the resonant wave add constructively, giving the strong resonant scattering. The resonance condition acts as a filter which selects the matched surface component from the continuous spectrum of the target surface. Because of this, Bragg scattering can be quite strong even though the Bragg-resonant wave energy is of very small amplitude.

The Bragg scattering is directly predicted by the small perturbation model, and second order Bragg resonance gives cross-polarized scattering. The sea surface scattering is dominated by Bragg scattering at moderate angles [27]. Bragg scattering from roughness that is bound to the crests of steep waves has been suggested as one of the mechanism which produce sea-spike events [79] [80], although this model has been recently questioned [81].

#### • Quasi-specular Reflection

According to Snell's reflection law, most of the energy incident upon a slightly rough surface will be reflected in the specular direction. Therefore, when the incidence illumination is not normal to the mean surface, the backscattered energy is usually much smaller than the scattering in the specular-reflection direction. However, if the

surface is very rough or the slopes at some points are sufficiently large, there may be points where the incident direction is approximately parallel to the local surface normal vector even with off-normal incidence. This leads to strong backscattering known as quasi-specular reflection (also termed as quasi-specular scattering) [82]. Overturning crests on breaking waves can lead to quasi-specular scattering even at high incidence angles. This has been suggested as a mechanism that leads to sea spikes [15] [29]. The quasi-specular reflection usually assumed to be independent of polarization (that is,  $HH=VV$ ), but recent work by West [1] showed they are different when an overturning jet exists with radii of curvature smaller than the EM wavelength on a breaking wave surface.

- **Multipath Reflection**

Experimental studies have shown that quasi-specular reflection can be related to wave breaking events, and can be a major contributor to the backscattering at grazing incidence angles [11][16]. However, traditional specular reflection models only predict  $HH/VV$  ratios up to 0 dB, but not the super-events where the  $HH/VV$  ratio can exceed 10 dB. However, overturning surface points can also introduce multi-path reflections. Figure 2.5 shows the multi-path reflections that lead to backscattering. The “single-bounce” multipath is shown as A-A1-A2 and the “double-bounce” path is B-B1-B2-B3. The quasi-specular reflection shown as C-C1. Experimental [83][84] studies have indicated that interference of the multi-path reflections can lead to sea-spike events. Wetzel [79] applied the multi-path interference model to analyze the scattering from the overturning section of the wave crest at LGA incidence. Trizna [15] added Brewster angle effects to the multipath at the bounce points and found that  $VV$  multipath is greatly damped due to the finite conductivity of the surface. This leads to reduced interference at  $VV$  compared to  $HH$  at low grazing angles, contributing to the sea spike effect. West [85] confirmed this numerically using the moment method with optical techniques to describe the multipath reflection.

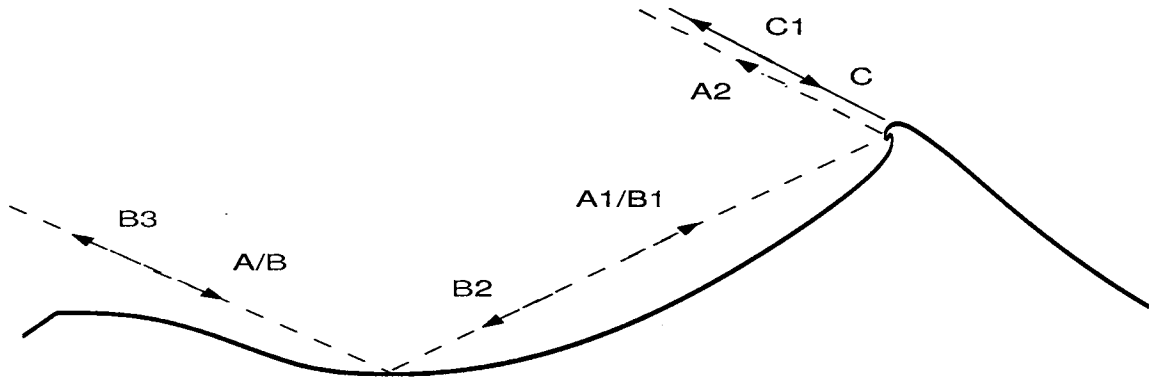


Figure 2.5: Multipath reflection. Path  $A - A_1 - A_2$  is ‘Single-bounce’ interactions; Path  $B - B_1 - B_2 - B_3$  is ‘Double-bounce’ interactions; Path  $C - C_1$  is the quasi-specular reflection.

### • Surface Self-shadowing

As the incidence angle increases (the grazing angle decreases), sections of the surface may be shadowed from the illumination by other more forward surface sections. Scattering models typically assume that the field within the shadowed region is exactly zero [86]. This results from the geometrical optics (or ray-optical) approximation. However, as shown in Figure 2.6, the shadow-region fields are not zero due to diffraction over the shadowing obstacle, due to either edge [87] or creeping wave diffraction [88]. To take the shadowing effects into consideration, some attempts based on optical shadowing functions have been used in the scattering models [89][90][79].

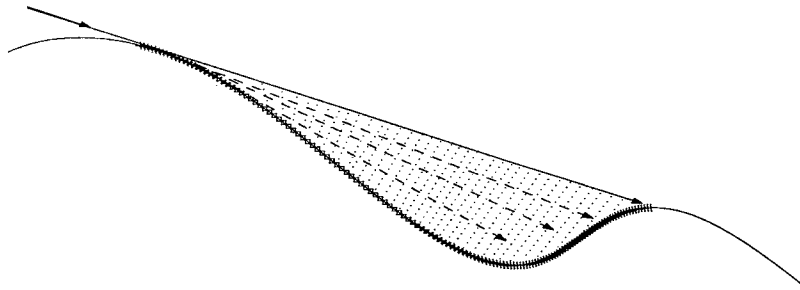


Figure 2.6: Surface self-shadowing effect. Solid line is the incident ray; Dashed lines are the diffraction rays; Bold-faced section of the surface stands for the creeping waves.

These simple corrections show acceptable results for the slightly shadowed cases since the dominant scattering is from the directly illuminated surface features. However, when the incidence approaches grazing, much of the surface is shadowed, and the relative contribution of the diffraction into the unlit regions becomes more significant. Simple corrections then fail to give good predictions. West *et al.* [75][71] numerically examined the effects of surface self-shadowing. They showed that shadowed roughness can significantly contribute to backscattering from perfectly conducting surfaces. Weakly shadowed roughness contributes to both HH and VV backscatter in that case, but deeply shadowed roughness only contributes to the vertically polarized backscattering. As the conductivity of the surface is reduced, the VV contribution of deeply shadowed roughness drops rapidly. Weakly shadowed roughness is still important, however.

## 2.5 Polarimetric Study

In 3-D surface scattering, cross-polarization components arise since the induced surface currents may flow in any direction. Therefore, depolarization is a typical phenomenon in 3-D surface scattering. In order to characterize depolarization phenomena, the polarimetric signature is defined to describe the different polarization states. The polarimetric signature can be described using different methods. Here, we follow the method presented by Airiau *et al.* [91] based on the description of average received power. In the scattering geometry shown in Figure 2.3, the perpendicular polarization vector pair  $(\mathbf{h}_r, \mathbf{v}_r)$  is defined as the receiving basis, and  $(\mathbf{h}_s, \mathbf{v}_s)$  is defined as the scattering basis. The average received power is  $P = \langle |V|^2 \rangle$ . The received voltage at the receiving antenna is expressed as

$$V = \mathbf{a}_r^T [S_A] \mathbf{a}_t, \quad (2.5)$$

where  $\mathbf{a}_t$  and  $\mathbf{a}_r$  are the polarization vectors of the transmitting antenna and of the receiving antenna respectively, and  $[S_A]$  represents the scattering matrix written in the receiving basis. Because a transform relationship exists between the receiving and scattering polarization bases [92] as

$$\begin{bmatrix} \mathbf{h}_r \\ \mathbf{v}_r \end{bmatrix} = \begin{bmatrix} -1 & 0 \\ 0 & 1 \end{bmatrix} \begin{bmatrix} \mathbf{h}_s \\ \mathbf{v}_s \end{bmatrix}, \quad (2.6)$$

the scattering matrix  $[S_A]$  can be expressed in the scattering basis  $[S]$  as

$$[S_A] = \begin{bmatrix} -1 & 0 \\ 0 & 1 \end{bmatrix} [S] = \begin{bmatrix} -S_{hh} & -S_{hv} \\ S_{vh} & S_{vv} \end{bmatrix}. \quad (2.7)$$

Then the expression for the average received power is given by

$$P = \left\langle [\mathbf{a}_h^r \ \mathbf{a}_v^r] \begin{bmatrix} -S_{hh} & -S_{hv} \\ S_{vh} & S_{vv} \end{bmatrix} \begin{bmatrix} \mathbf{a}_h^i \\ \mathbf{a}_v^i \end{bmatrix} [\mathbf{a}_h^{r*} \ \mathbf{a}_v^{r*}] \begin{bmatrix} -S_{hh}^* & -S_{hv}^* \\ S_{vh}^* & S_{vv}^* \end{bmatrix} \begin{bmatrix} \mathbf{a}_h^{i*} \\ \mathbf{a}_v^{i*} \end{bmatrix} \right\rangle \quad (2.8)$$

This expression is general for any target and any polarization. The expression for the received power is the polarimetric signature at a particular condition. For example, the co-polarization power is defined when  $\mathbf{a}_r = \mathbf{a}_t$ , and the cross-polarization power is defined when  $\mathbf{a}_r \perp \mathbf{a}_t$ .

In analytical scattering theory, the scattering cross-sections usually are defined as  $\sigma_{pq} = \langle |S_{pq}|^2 \rangle$  and  $\sigma_{pp'q'q'} = \langle S_{pq} S_{p'q'}^* \rangle$ , where  $p, q, p'$  and  $q'$  represent the polarization direction  $h$  or  $v$ . The definition of the scattering cross-section (RCS) in (2.1) and (2.2) shows that the polarization dependent scattering cross sections have the same physical significance as the polarimetric signature. Therefore, the concept of the scattering cross section is still used to discuss depolarization effects in this paper.

# Chapter 3

## Review of Analytical Scattering Models

As mentioned in Chapter 1, a common method to describe scattering from a random roughness surface is the two-scale model (TSM), (also called the composite surface model (CSM)). This model is the combination of two different scattering models: the Kirchhoff approximation (KA) and the small-perturbation method (SPM). KA predicts quasi-specular reflection, while Bragg-resonant scattering results from SPM scattering. KA is suitable for high frequency applications such that a surface appears smooth on the scale of the wavelength of the incident wave. SPM is applied to small-displacement, rapidly-changing surfaces. Therefore, the roughness on an arbitrary surface must first be separated into electromagnetically large-scale and small-scale components prior to the application of TSM. This is the primary limitation of TSM. The results of TSM have been shown to depend upon the roughness-separation approach used [93] [94] [95] [96]. Additional methods have been introduced to overcome this limitation. Two to be considered here are the small-slope approximation (SSA) and the phase-perturbation technique (PPT). Brief overviews of KA, SPM, TSM, SSA, and PPT are given below.

### 3.1 Kirchhoff Approximation

The Kirchhoff approximation (KA) is a scattering model based on the physical optics approximation. It approximates the current at a surface point by that which would be induced by the incident field on an infinitely extending plane of the same dielectric properties that is tangential to the surface at that point. The equivalent electric and magnetic surface currents are therefore approximated by

$$\mathbf{J}_{KA} = \begin{cases} (1 - \Gamma)\hat{n} \times \mathbf{H}^i & \text{illuminated area,} \\ 0 & \text{shadowed area,} \end{cases} \quad (3.1)$$

$$\mathbf{M}_{KA} = \begin{cases} -(1 + \Gamma)\hat{n} \times \mathbf{E}^i & \text{illuminated area,} \\ 0 & \text{shadowed area,} \end{cases} \quad (3.2)$$

respectively, where  $\Gamma$  is the surface reflection coefficient at normal incidence. For a perfectly conducting surface  $\Gamma = -1$ . These currents are then re-radiated into the far field to give the scattered field.

KA is valid only for gently undulating surfaces which have large radii of curvature relative to the electromagnetic wavelength so that the tangential plane approximation is valid. KA predicts quasi-specular reflection. Thorsos [97] investigated the validity of KA for random, one-dimensionally rough surfaces (the 2-D electromagnetic problem) with Gaussian roughness spectra. He showed that KA performs well with near normal incidence where quasi-specular reflection dominates, but performs poorly at low grazing.

### 3.2 Small Perturbation Model

The small perturbation model (SPM) was first developed by Rice [28] in 1951. SPM may be used for rough surface scattering analysis when the surface height variation is



much smaller than the incident wavelength. This algorithm treats the scattered fields as functions of the surface height and expands them in a perturbation series in the surface wave-number domain. When the roughness is sufficiently small, the fields may be accurately represented by a truncated perturbation series. The first-order SPM is widely used, which includes both the zeroth and first order terms of the perturbation series. SPM predicts the Bragg scattering.

For a one-dimensional randomly rough surface with dielectric constants  $\epsilon_r$  and  $\mu_r = 1$ , the mean scattering cross-section per unit length (the backscattering coefficient) for horizontal (HH) or vertical (VV) polarizations are given by [8]

$$\sigma_{pp}(\theta_i) = 4k^3\sigma^2 \cos^4 \theta_i |\alpha_{pp}|^2 W(2k \sin \theta_i) , \quad (3.3)$$

where the subscript  $pp$  stands for  $VV$  or  $HH$ ,  $k$  is the wave number of the incident field, and  $\sigma$  is the standard variance of the surface height.  $W$  is the normalized roughness spectrum that is the Fourier transform of the surface correlation coefficient and  $\alpha_{pp}$  is a polarization term [8] [98] which depends on the physical characteristics (permittivity, conductivity) of the surface and on the incidence and observation angles  $(\theta_i, \phi_i, \theta_s, \phi_s)$ .

Equation (3.3) shows that only roughness energy at a specific wave number contributes to the backscattering. This wave satisfies the Bragg resonant condition since its wave number is  $2k \sin \theta_i$ . Therefore, it is the Bragg resonance incited by the incident fields that generates the backscattering, so the first-order perturbation solution of SPM explicitly expresses the Bragg scattering phenomena.

### 3.3 Two-Scale Model for Deterministic Surfaces

The two scale model (TSM), also termed composite surface theory, was first suggested for acoustic scattering by Kur'yanov [99] and then applied to electromagnetic

scattering from rough surfaces. This model requires that the entire surface-roughness spectrum be decomposed into small-scale and large-scale roughness surface components. Scattering from small-scale disturbances can be described by SPM, whereas quasi-specular reflections from undulating large-scale roughness is described by KA. The large-scale components therefore act locally as planar, tilted facets.

The two-scale model is typically applied to rough surfaces after the statistical analysis applies the ensemble averaging to yield a scattering coefficient. The scale-separation is applied to the surface roughness spectrum, typically through low- and high-pass linear filtering. KA and SPM are statistically applied to the resulting large- and small-scale roughness, yielding scattering coefficients that are incoherently added to give the composite surface scattering coefficients. The tilting of the small-scale roughness by the large-scale roughness, which changes the local Bragg resonance condition, is usually included in the SPM analysis.

Brown [93] presented a deterministic representation of the zero order KA field and the first-order SPM field based on the boundary perturbation approach of Burrows [100]. In this, individual realizations of the rough surface are separated into large-scale and small-scale roughness components via some criteria. The zeroth-order scattering is computed from the large-scale surface using the deterministic KA which yields a coherent field. The first-order SPM result is calculated by perturbing the field from large-scale surface using the small-scale surface displacement, also giving a coherent field. Unlike the statistical SPM analysis, the deterministic TSM field is found from the coherent (phase-preserved) addition of the KA and SPM fields. This allows a direct comparison of the TSM result with the reference numerical field found from the same sample surface.

Deterministic TSM is applied by separating the composite surface  $\zeta(x, y)$  into large- and small-scale components so that

$$\zeta(x, y) = \zeta_l(x, y) + \zeta_s(x, y) . \quad (3.4)$$

For a perfectly conducting surface, the large-scale scattered (KA) field is given by

$$\delta^0 E_{pp'} = -j \frac{E_o k_o \delta_{pp'}}{2\pi r \cos \theta} \exp(-jk_o r) \iint \exp(-j2\mathbf{k}_i \cdot \mathbf{r}_o) dx dy , \quad (3.5)$$

while the first order SPM field is

$$\delta^1 E_{pp'} = \frac{E_o k_o^2}{\pi r} \exp(-jk_o r) \iint \Gamma_{pp'}(\zeta_{lx}, \zeta_{ly}) \cdot \exp(-j2\mathbf{k}_i \cdot \mathbf{r}_o) \zeta_s dx dy , \quad (3.6)$$

where

$$\Gamma_{pp'}(\zeta_{lx}, \zeta_{ly}) = \frac{2(\hat{n} \cdot \hat{e}_p)(\hat{n} \cdot \hat{e}_{p'}) + (\hat{n} \cdot \hat{k}_i)^2(\hat{e}_p \cdot \hat{e}_{p'})}{(\sqrt{1 + \zeta_{lx}^2 + \zeta_{ly}^2})^{-1}} , \quad (3.7)$$

$\hat{n}$  is the unit vector normal to the unperturbed large-scale surface,  $\mathbf{r}_o = x\hat{a}_x + y\hat{a}_y + \zeta_l\hat{a}_z$  is the position vector of a point on the unperturbed surface,  $\mathbf{k}_i$  is the incident wave vector,  $\hat{e}_p$  and  $\hat{e}_{p'}$  are the polarization unit vectors for the scattered and incident fields respectively, ( $\hat{e}_p$  and  $\hat{e}_{p'}$  are identical for co-polarized scattering and are orthogonal for the cross-polarized case), and  $\delta_{pp'}$  is the Kronecker delta function.

The backscattered electric field from a perfectly conducting surface with polarization  $p'$  for an incident field with polarization  $p$  is

$$E_{pp'} \approx \delta^0 E_{pp'} + \delta^1 E_{pp'} . \quad (3.8)$$

Typically  $p/p'$  correspond to vertical or horizontal polarization, although  $\hat{e}_p$  can take any value orthogonal to the incident vector.

For an imperfectly conducting surface, the scattered fields are modified by multiplying by a factor dependent upon the material properties:

$$E_{imp} = E_{PEC} \alpha_{pp'} , \quad (3.9)$$

where  $\alpha_{pp'}$  is a polarization dependent coefficient given by [101]

$$\alpha_{VV} = -(\epsilon_r - 1) \frac{\sin^2 \theta_i - \epsilon_r(1 + \sin^2 \theta_i)}{[\epsilon_r \cos \theta_i + \sqrt{\epsilon_r - \sin^2 \theta_i}]^2} \frac{\cos^2 \theta_i}{1 + \sin^2 \theta_i}, \quad (3.10)$$

$$\alpha_{HH} = -\frac{\cos \theta_i - \sqrt{\epsilon_r - \sin^2 \theta_i}}{\cos \theta_i + \sqrt{\epsilon_r - \sin^2 \theta_i}}, \quad (3.11)$$

where  $\theta_i$  is the local incident angle with respect to the external normal vector of the large-scale surface defined by  $\cos \theta_i = -\hat{n} \cdot \hat{k}_i$ .

As mentioned earlier, the surface separation is a critical step in the TSM implementation. Linear low-pass and a high-pass filters are usually employed to yield the large-scale and small-scale surface, respectively. A surface wave number threshold is used as the cutoff parameter for these filters. Unfortunately, a threshold that yields components that simultaneously meet requirements for KA and SPM does not always exist. Errors arise when inexact thresholds are used. This is one of the inherent drawbacks of TSM.

Despite the limitations, TSM has proven effective in predicting the scattering from rough surfaces at moderate grazing angles. However, the absence of surface self-shadowing is assumed in TSM, which leads to poor performance at small grazing angles where surface self-shadowing becomes significant. Various shadowing functions and iterative corrections have been proposed to improve LGA TSM [102]. However, both analytical and numerical investigation [103] [104] have shown that shadowing correction based on geometrical optics fails to properly account for both diffraction and multipath scattering into shadowed regions.

### 3.4 SSA and PPT

The small-slope approximation model (SSA) [105] is based on expansion of the field equations with respect to the slope of the surface. It reduces to KA and SPM when

applied to large-scale or small-scale surfaces individual, and gives a continuous transition between each. SSA therefore avoids the artificial scale-separation required by TSM. Hence, SSA is particularly appropriate for multi-scale surfaces.

Application of SSA requires that the incident angle and the scattering angle of all waves with significant amplitudes exceed RMS slope of the roughness. Modulation of Bragg scattering by large-scale tilt implicitly included in SSA [106]. Both the first- and second-order expansions in slope have been implemented in SSA. Detail derivations of SSA are found in [106] [107]. Broschat *et al.* [108] numerically investigated the range of validity of SSA when applied to surfaces whose roughness spectra were described by a Gaussian function.

SSA underestimates HH backscattering from the sea surface at large incidence angles when looking in the upwind and cross-wind directions. This is believed to result from scattering from steep breaking waves, which give large surface slopes. To compensate this, Voronovich and Zavorotny [109] added an additional term to the backscattering cross-section based on geometrical optics approximation. This assumes that breaking waves specularly reflect some energy back. This requires an estimate of the probability density function of steep waves, which is not well known. It also does not account for multipath scattering from the steep crests.

Another recently introduced scattering model is the phase perturbation technique (PPT) [32]. PPT is based on a perturbation expansion of a function related to the complex phase of the surface current density induced on the surface by the incident field. The truncated phase perturbation series expansion provides an approximation to all the higher-order terms of the classical perturbation expansion. The phase-perturbation expression for the reflected and backscattering coefficients also reduces to SPM and KA in the appropriate surface roughness limits [34]. However, PPT does not satisfy reciprocity, which compromises its validity at low grazing angles. Details of the complete derivation and numerical examples can be found in [33] [34] [110].

### 3.5 Optical Models

SPM is a low-frequency asymptotic model for rough surface scattering computation, while KA is a high-frequency model based on the physical optics approximation. Geometrical optics (GO) (or ray optics) arises as the infinite-frequency limit of physical optics. GO predicts only specular reflection, so that the application of GO is limited only to those surface sections which have large radii of curvature compared to the electromagnetic wavelength.

According to GO theory, the reflected electric field at a distance  $r$  from the reflection point  $Q_R$  can be expressed as [77]

$$\mathbf{E}^r(r) = \mathbf{E}^i(Q_R) \cdot \Gamma \sqrt{\frac{\rho_1^r \rho_2^r}{(\rho_1^r + r)(\rho_2^r + r)}} e^{-jkr}, \quad (3.12)$$

where  $\mathbf{E}^i(Q_R)$  is the incident field at the reflection point,  $\Gamma$  is the reflection coefficient at the reflection point, and  $\rho_1^r$  and  $\rho_2^r$  are the principal radii of curvature of the reflected wave front at the point of reflection. These principle radii of curvature are related to the curvature of the reflection surface at  $Q_R$  and the principal radii of the curvature of the incident wave front. For plane wave incidence, the principal radii of curvature of the incident wave front are infinite. Then,  $\rho_n^r$  can be expressed as

$$\rho_n^r = \frac{\rho_{a_n} \cos \theta_i}{2}, \quad n=1,2, \quad (3.13)$$

where  $\theta_i$  is the incident angle,  $\rho_{a_n}$  is the radius of curvature of the reflection surface at  $Q_R$ . The radii of curvature are defined to be positive for convex curvature and negative for concave curvature at the reflection point. (3.12) is the electric field reflected by the specular reflection point on a 3-D surface. For a 2-D surface, one dimension of the surface is uniform, so the radius of curvature in this dimension is

infinity. (3.12) then reduces to 2-D GO:

$$\mathbf{E}^r(r) = \mathbf{E}^i(Q_R) \cdot \Gamma \sqrt{\frac{\rho_1^r}{\rho_1^r + r}} e^{-jkr}. \quad (3.14)$$

Classical GO is valid only when the curvature of the surface is large compared with the incident field wavelength. The correction factor to GO reflected fields proposed by Voltmer [111] and used by Stutzman and Thiele [112] allows the model to maintain accuracy as the radii of curvature decreases somewhat below a wavelength [111]. The corrected method was called as the extended GO (EGO) by West [2]. For backscattering from a PEC cylinder, the correction factor is

$$M = \begin{cases} 1 + j \frac{11}{16(k\rho_a)} - \frac{353}{512(k\rho_a)^2} & \text{VV} \\ 1 - j \frac{5}{16(k\rho_a)} + \frac{127}{512(k\rho_a)^2} & \text{HH} \end{cases}, \quad (3.15)$$

where  $k = 2\pi/\lambda$  is the electromagnetic wave number.

The geometrical theory of diffraction (GTD) is the ray optical model that predicts the diffractive scattering from discontinuities in surface derivatives [77]. According to GTD theory, the diffracted field scattered by the discontinuities is given by

$$\mathbf{E}^d(r) = \mathbf{E}^i(Q_D) \cdot \bar{D} \cdot A e^{-jkr}, \quad (3.16)$$

where  $\mathbf{E}^i(Q_D)$  is the incident field at the diffraction point  $Q_D$ ,  $\bar{D}$  is the diffraction coefficient and  $A$  is a spatial attenuation factor. For plane wave incidence on a 2-D surface,  $A = 1/\sqrt{r}$ . GTD diffraction coefficients have been derived for diffraction from the edges [2], curvature discontinuities[87], and creeping diffraction around smooth cylinders [113].

West [2] included the diffractive backscattering from the inflection point between the jet and cavity regions of the LONGTANK series profiles where the curvature transitions from convex to concave. When combined with EGO reflection, this represented

the dominant scattering mechanisms through profile 12.



# Chapter 4

## Moment Method-based Numerical Techniques Review

The moment method (MM) is commonly applied in surface scattering numerical computations. MM obtains the induced current distribution by solving a linear system of equations which is set up through an approximate expansion based on a set of basis functions. A simple subdomain basis function set can be used for 2-D surface scattering. Non-physical edge diffraction incited by surface truncation is one of critical factors that affect surface scattering analysis. A modified basis function set was developed in MM/GTD to avoid the edge diffraction problem. The RWG vector basis function was specially defined for 3-D surface scattering problems. In order to reduce computational complexity of solving the dense matrix linear system that results from an MM expansion, the fast multipole and multilevel fast multipole expansion techniques have been developed. In this chapter, these techniques and surface edge treatment approaches derived to avoid non-physical edge diffraction are reviewed. A brief introduction of iterative solvers and the preconditioning approaches used to solve the MM linear system is also presented. The induced current distribution on a flat plate and its scattering phenomena are then considered in order to examine the validity of the numerical techniques and formulate the concepts involved

in bistatic electromagnetic scattering.

## 4.1 Preliminary Electromagnetic Theory

The electromagnetic fields within a homogeneous medium are radiated by electric and magnetic current sources, designed  $\mathbf{J}$  and  $\mathbf{M}$  respectively. Vector potentials are defined within the region to relate the current sources to the radiated fields. The magnetic vector potential  $\mathbf{A}$  and the electric vector potential  $\mathbf{F}$  are defined by the integration of Green's function over the current sources as

$$\mathbf{A}(\mathbf{r}) = \frac{\mu}{4\pi} \int_s \mathbf{J}(\mathbf{r}') \frac{e^{-jkR}}{R} dS' = \mu \int_s \mathbf{J}(\mathbf{r}') G(\mathbf{r}, \mathbf{r}') dS', \quad (4.1)$$

$$\mathbf{F}(\mathbf{r}) = \frac{\epsilon}{4\pi} \int_s \mathbf{M}(\mathbf{r}') \frac{e^{-jkR}}{R} dS' = \epsilon \int_s \mathbf{M}(\mathbf{r}') G(\mathbf{r}, \mathbf{r}') dS', \quad (4.2)$$

where

$$G(\mathbf{r}, \mathbf{r}') = \frac{e^{-jkR}}{4\pi R} = \frac{e^{-jk|\mathbf{r}-\mathbf{r}'|}}{4\pi|\mathbf{r}-\mathbf{r}'|},$$

$k = \omega\sqrt{\mu\epsilon}$ ,  $R = |\mathbf{r} - \mathbf{r}'|$ , and  $\mathbf{r}$ ,  $\mathbf{r}'$  are vector positions of source and observation point respectively. The radiation fields are found from the vector potentials  $\mathbf{A}$  and  $\mathbf{F}$  using

$$\mathbf{E} = -j\omega\mathbf{A} - \nabla\Phi_e - \frac{1}{\epsilon}\nabla \times \mathbf{F}, \quad (4.3)$$

$$\mathbf{H} = -j\omega\mathbf{F} - \nabla\Phi_m + \frac{1}{\mu}\nabla \times \mathbf{A}, \quad (4.4)$$

where  $\Phi_e = -\frac{1}{j\omega\mu\epsilon}\nabla \cdot \mathbf{A}$  and  $\Phi_m = -\frac{1}{j\omega\mu\epsilon}\nabla \cdot \mathbf{F}$  are called scalar potentials.

The source of a scattered field is the re-radiation of the current induced on or within the scatterer by the incident field. With a perfect electric conductor, an electric surface current is induced on the surface. With a general finite conductivity scattering medium, a physical surface current does not exist. Instead a volume current is induced throughout the scatterer. Although the numerical techniques are available,

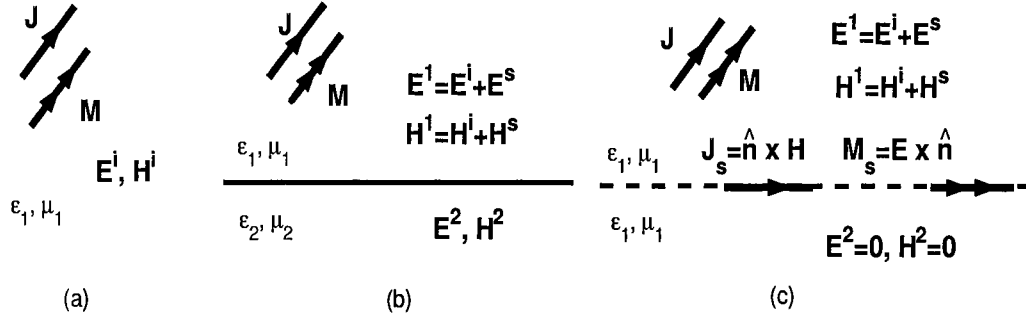


Figure 4.1: Electromagnetic equivalence for finite conductivity scatter .

the calculation of the volume current induced within a scatterer is numerically expensive. Instead, an electromagnetically equivalent problem is usually solved. The equivalence theorem is applied as shown in Figure 4.1. Part (a) of the figure shows the electric and magnetic source current  $\mathbf{J}$  and  $\mathbf{M}$  radiating into free space, thus providing the incident field  $\mathbf{E}^i$  and  $\mathbf{H}^i$ . The scattering surface added in part(b) induces the scattered field  $\mathbf{E}^s$  and  $\mathbf{H}^s$ . Part (c) shows the equivalent problem, in which identical constitutive parameters (permittivity  $\epsilon_1$  and permeability  $\mu_1$ ) appear above and below the interface, so that the physical boundary disappears. Instead, equivalent surface currents on the virtual boundary that meet the boundary conditions

$$\mathbf{J}_s = \hat{\mathbf{n}} \times (\mathbf{H}^i + \mathbf{H}^s), \quad (4.5)$$

$$\mathbf{M}_s = -\hat{\mathbf{n}} \times (\mathbf{E}^i + \mathbf{E}^s), \quad (4.6)$$

are found, where  $\mathbf{J}_s$  and  $\mathbf{M}_s$  are the equivalent electric and magnetic surface currents. These equivalent surface currents, as well as original source currents ( $\mathbf{J}$  and  $\mathbf{M}$ ), give the total (incident plus scattered) fields above the surface and zero fields within the scatterer. Once the equivalent surface currents are known, the scattered fields, and thus the RCS is easily computed. Therefore, the goal of the surface scattering problem

becomes finding the equivalent surface currents. The equivalent boundary condition described in (4.5), (4.6) can be expressed by the electric field integral equation (EFIE) and the magnetic field integral equation (MFIE). Moment method-based numerical techniques are suitable solvers for these integral equations. Note that the equivalence principle can only be applied to homogeneous scatterers, which always holds for the rough surface scattering cases considered in this paper.

Various methods have been developed to reduce the computational complexity of finding the surface currents. Glisson [114] showed that if the scatterer has a large dielectric constant and conductivity, the impedance boundary conditions of Senior [115] can be used to directly relate the magnetic surface current to the electric surface current. When the conditions

$$|N| \gg 1, \quad |Im(N)k\rho_l| \gg 1 \quad (4.7)$$

are met everywhere on the surface, where  $k$  is the electromagnetic wave number,  $N$  is the complex refractive index of the scattering medium, and  $\rho_l$  is the radius of curvature of the surface, the energy refracted into the scatterer will propagate nearly normal to the surface. The surface current densities can then be related by

$$\mathbf{M}_s = -Z_s \hat{n} \times \mathbf{J}_s, \quad (4.8)$$

where  $Z_s$  is the intrinsic wave impedance of the lossy dielectric,  $\hat{n}$  is the unit vector normal to the surface,  $\mathbf{J}_s$  and  $\mathbf{M}_s$  are the electric and magnetic surface current densities respectively. Since  $\mathbf{M}_s$  and  $\mathbf{J}_s$  are now related only by a constant, one need only solve for one (typically,  $\mathbf{J}_s$  for high conductivity surfaces). West [66][116] implemented impedance boundary conditions in the MM/GTD code.

## 4.2 Electromagnetic Field Integral Equations

Once the equivalent surface current  $\mathbf{J}_s$  and  $\mathbf{M}_s$  have been found, the scattered fields  $\mathbf{E}^s$  and  $\mathbf{H}^s$  can be calculated via the equations (4.1) to (4.4). Now substituting  $\mathbf{E}^s$ ,  $\mathbf{H}^s$  into the electromagnetic field boundary conditions of (4.5) and (4.6) gives

$$\hat{n} \times \mathbf{E}^i = \hat{n} \times \left\{ j\omega \mathbf{A} + \nabla \Phi_e + \frac{1}{\epsilon} \nabla \times \mathbf{F} \right\}, \quad (4.9)$$

$$\hat{n} \times \mathbf{H}^i(\mathbf{r} = \mathbf{r}') = \mathbf{J}_s(\mathbf{r}') - \lim_{\mathbf{r} \rightarrow S} \left\{ \hat{n} \times \left( \frac{1}{\mu} \nabla \times \mathbf{A} \right) - \hat{n} \times [j\omega \mathbf{F} - \nabla \Phi_m] \right\}. \quad (4.10)$$

Equation (4.9) is termed the electric field integral equation (EFIE), and (4.10) is the magnetic field integral equation (MFIE). The MFIE is valid only for closed surfaces. When PEC surfaces are under consideration,  $\mathbf{M}_s=0$ , thus  $\mathbf{F}=0$ ,  $\Phi_m=0$ . The integral equations therefore reduce to

$$\hat{n} \times \mathbf{E}^i = \hat{n} \times \{ j\omega \mathbf{A} + \nabla \Phi_e \}, \quad (4.11)$$

$$\hat{n} \times \mathbf{H}^i(\mathbf{r} = \mathbf{r}') = \mathbf{J}_s(\mathbf{r}') - \lim_{\mathbf{r} \rightarrow S} \left\{ \hat{n} \times \left( \frac{1}{\mu} \nabla \times \mathbf{A} \right) \right\}. \quad (4.12)$$

The simpler two-dimensional scattering geometry is first considered, the geometry of which is shown in Figure 4.2. The 2-D surface is in the XY plane. The incident field can be either horizontally or vertically polarized. For horizontally polarized incidence ( $TM^z$  mode), the corresponding induced surface currents are  $J_z$  in the transverse direction and  $M_l$  in the tangential direction respectively, where the transverse direction is normal to the XY plane, the tangential direction is in the XY plane and tangential to the surface at the points in question. The scattered electric fields are expressed as

$$E_z^s(J_z(l'), \rho) = -\frac{k\eta}{4} \int_c J_z(l') H_0^{(2)}(k|\rho - \rho'|) dl' = -L_E[J_z(l')], \quad (4.13)$$

$$E_z^s(M_l(l'), \rho) = \frac{1}{2} M_l(l') + j\frac{k}{4} \oint_c M_l(l') [\hat{n}' \cdot \left( \frac{\rho - \rho'}{|\rho - \rho'|} \right)] H_1^{(2)}(k|\rho - \rho'|) dl', \quad (4.14)$$

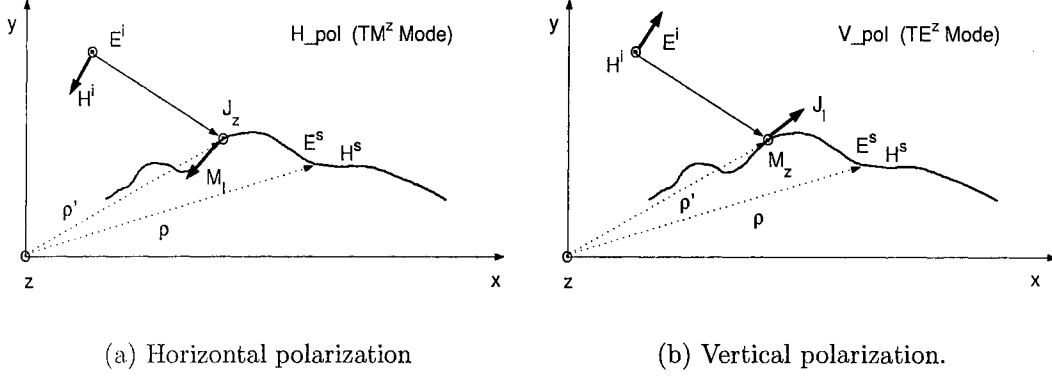


Figure 4.2: Scattering geometry of 2-D surface.

where  $\rho'$  is the vector from the origin to a source point on the surface,  $\rho$  is the observation point vector,  $k$  is the electromagnetic wave number,  $\eta$  is the intrinsic impedance of the medium above the surface.  $\hat{n}'$  is the unit vector normal to the surface at source point.  $\oint$  represents the principal value integral around the singularity at  $l = l'$ .  $H_n^{(2)}$  is the  $n$ th-order Hankel function of the second kind, which results from the infinite azimuthal integration of the 3-D Green's function, and represents the outward traveling EM waves.

When the impedance boundary condition (4.7) is satisfied, the relationship between  $M_s$  and  $J_s$  in (4.8) can be applied into (4.14) to give

$$\begin{aligned}
 E_z^s(M_l(l'), \rho) &= -\frac{1}{2}Z_s J_z(l') - j\frac{k}{4}\oint_c Z_s J_z(l') [\hat{n}' \cdot (\frac{\rho - \rho'}{|\rho - \rho'|})] H_1^{(2)}(k|\rho - \rho'|) dl' \\
 &= -Z_s L_M[J_z(l')].
 \end{aligned} \tag{4.15}$$

Inputting the scattered fields (4.13) and (4.15) into the electric field boundary condition (4.6) yields the EFIE

$$E_z^i = -E_z^s = L_E[J_z(l')] + Z_s L_M[J_z(l')]. \tag{4.16}$$

For vertically polarized incidence ( $TE^z$  mode), the induced surface currents are  $J_l$  and  $M_z$  respectively. Following similar procedures, the 2-D MFIE for impedance

boundary conditions is found to be

$$H_z^i = L_E[J_l(l')] + \frac{Z_s}{\eta^2} L_M[J_l(l')]. \quad (4.17)$$

Note that  $Z_s = 0$  for PEC surfaces, so the second terms on the right hand side of (4.16) and (4.17) disappear.

### 4.3 Moment Method for 2-D Scattering Problem

The EFIE of (4.16) and the MFIE of (4.17) can be generalized as

$$F_z(l)^i = L[J_s(l)], \quad (4.18)$$

where  $F$  stands for the incident field  $E_z^i$  or  $H_z^i$ , subscript  $s$  denotes the transverse direction  $z$  or the tangential direction  $l$ , and  $L[]$  is the linear integral operator. The moment method is applied by expanding the unknown current  $J_s$  as a weighted sum of known basis functions  $f_n(l)$  [117]

$$J_s(l) \approx \sum_{n=1}^N I_n f_n(l), \quad (4.19)$$

where the  $I_n$ 's are the unknown coefficients to be found via the moment method. Substituting (4.19) into (4.18) gives

$$F_z^i(l) \approx \sum_{n=1}^N I_n \{L[f_n(l)]\}. \quad (4.20)$$

The residual error is defined as

$$R(l) = F_z^i(l) - \sum_{n=1}^N I_n \{L[f_n(l)]\}. \quad (4.21)$$

A set of  $N$  weighted residuals are obtained by applying  $N$  testing functions to (4.21)

$$\langle w_m, R(l) \rangle = \langle w_m, F_z^i(l) \rangle - \sum_{n=1}^N I_n \{ \langle w_m, L[f_n(l)] \rangle \}, \quad (4.22)$$

where the inner product is defined as  $\langle f(l), g(l) \rangle = \int f(l) \cdot g(l) dl$ .

The moment method assumes that the residual error is minimized by setting  $\langle w_m, R \rangle = 0$ , giving

$$\sum_{n=1}^N I_n \{ \langle w_m, L[f_n(l)] \rangle \} = \langle w_m, F_z^i(l) \rangle. \quad (4.23)$$

(4.23) can be written in a matrix form

$$[Z_{mn}][I_n] = [V_m]. \quad (4.24)$$

(4.24) is now solved by using standard linear algebra techniques, yielding the approximate solution to the current. The far zone scattered fields can be found via the radiation equations as

$$E^s = -\frac{k\eta}{4} \int_c J_z(l') H_0^{(2)}(k|\rho - \rho'|) dl', \quad HH \text{ pol.} \quad (4.25)$$

$$H^s = j\frac{k}{4} \int_c J_l(l') [\hat{n}' \cdot (\frac{\rho - \rho'}{|\rho - \rho'|})] H_1^{(2)}(k|\rho - \rho'|) dl', \quad VV \text{ pol.} \quad (4.26)$$

The 2-D radar cross-section is then obtained from (2-1).

Equation (4.24) is a linear system of equations with a dense coefficient matrix. The system can be solved directly using LU factorization, requiring  $O(N^3)$  operations, where  $N$  is the number of unknowns. Iterative solution requires  $O(N^2)$  operations each iteration. Therefore, iterative solvers are often employed when the scattering from a large surface is computed using the moment method.

The choice of basis function sets is an important step in determining the final



accuracy of the moment method solution. Piecewise constant subdomain (pulse) functions are a common choice for the 2-D problem. The basis function in each subdomain is defined as

$$f_n(l) = \begin{cases} 1 & l_{n-1} \leq l \leq l_n, \\ 0 & \text{elsewhere.} \end{cases} \quad (4.27)$$

Dirac delta functions are typically used as testing functions applied at the center of each basis function. This forces the residuals to be exactly zero at discrete points, so this is often termed point matching. Figure 4.3 shows the piecewise constant approximation of current using the subdomain basis function. The far field scattering is found by integrating the currents. The accuracy improves with decreasing subdomain length. Basis function lengths of  $0.05\lambda$  have been shown to give sufficient accuracy, even with small scattering cross-sections[65] [118].

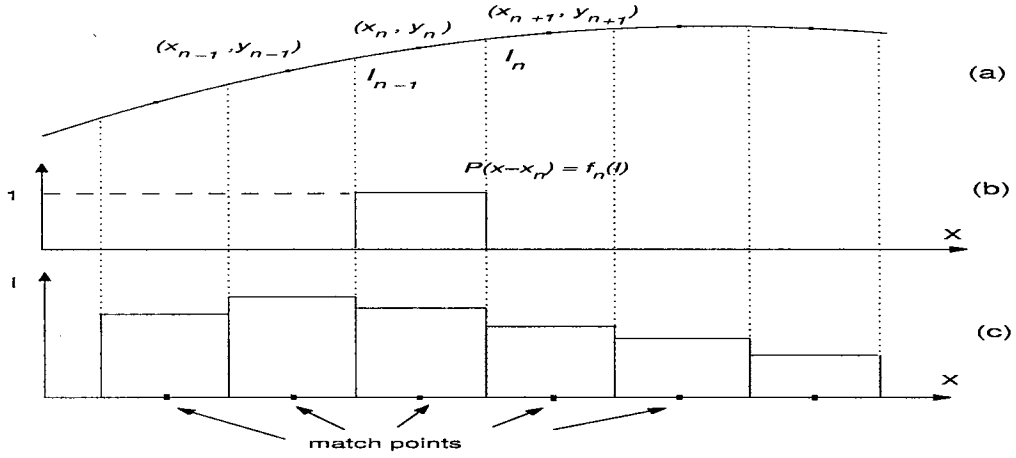


Figure 4.3: The approximation using piecewise constant subdomain functions. (a) Points and subdomains on the surface. (b) Pulse function. (3) Current approximation using pulse basis function.

## 4.4 Hybrid MM/GTD Technique

As mentioned, finite computer resources always require that the modeled surface be somehow truncated in a numerical scattering study. The truncation leads to non-physical edge diffraction, which both gives undesirable backscatter as well as affects the current across the surface. Therefore, the edge effects must somehow be reduced.

Different approaches have been used to suppress edge effects in moment method-based analyses. For example, Chen and West [64] used a periodic surface implementation of the moment method, which is well suited to 2-D periodic surface scattering analyses. West *et al.* [65][71] adapted the hybrid method that extends the moment method by using basis functions derived from the geometrical theory of diffraction (GTD) first developed by Buruside *et al.* [119] to scattering from rough surfaces with finite conductivity. This method allows the 2-D modeled surface to be extended to infinity, eliminating the edge effects. A brief overview is given here.

Figure 4.4 shows a surface that has been extended for the application of MM/GTD. The dotted line shows the truncated original rough surface, while the solid line represents interim curves and half-plane extensions. The modified surface does not include the non-physical edges. Standard MM pulse basis functions are used to represent the induced current in the MM region (between point A and point D). A single basis function derived from the GTD field is used to describe the unknown current in each

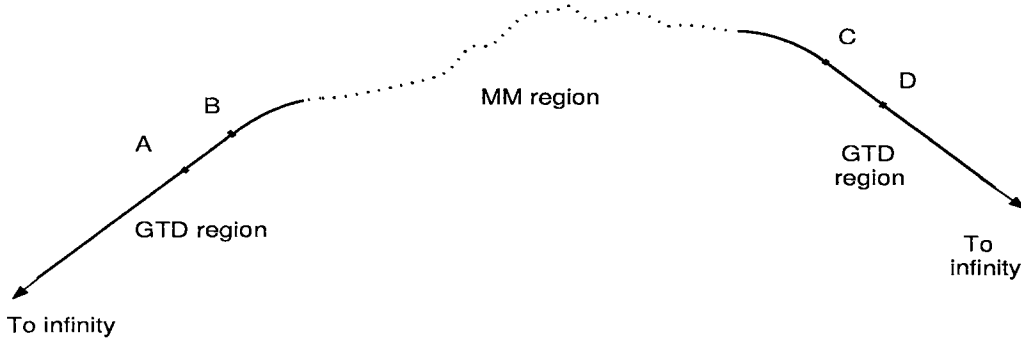


Figure 4.4: Infinity edge extension in MM/GTD technique.

of the GTD regions (outside of points A to D).

The total current in the GTD region is due to both the directly incident field  $\mathbf{H}^i$  and the fields diffracted from the connecting points B and C. The diffraction current is obtained by recognizing that far enough away from the diffraction point the diffracted field is ray optical [71]. The current in GTD regions can therefore be written as

$$\mathbf{J}_{GTD} = \mathbf{J}_d + \mathbf{J}_{PO}, \quad (4.28)$$

$$\mathbf{J}_d = \begin{cases} \hat{a}_z J_o \frac{e^{-jk\rho}}{\rho^{1.5}} & \text{HH,} \\ \hat{a}_l J_o \frac{e^{-jk\rho}}{\sqrt{\rho}} & \text{VV.} \end{cases},$$

$$\mathbf{J}_{PO} = (1 - \Gamma)\hat{n} \times \mathbf{H}^i,$$

where  $\mathbf{J}_d$  is the current induced by the diffraction, and  $\rho$  is the distance from the diffraction point to the observation point in the GTD region.  $\mathbf{J}_{PO}$  is the induced physical optics current due to the incident field  $\mathbf{H}^i$  (usually assumed to be zero in the shadowed region),  $\Gamma$  is the surface reflection coefficient at the interface, and  $J_o$  is an unknown coefficient that needs to be found by using the moment method. Hence, the current on the entire extended surface can be expressed as

$$\mathbf{J}_s = \begin{cases} \hat{a} \sum_{n=1}^N I_n f_n(l) & \text{for HH } \hat{a} = \hat{a}_z; \text{ for VV } \hat{a} = \hat{a}_l, \text{ MM region,} \\ \mathbf{J}_{GTD} = \mathbf{J}_d + \mathbf{J}_{PO} & \text{GTD regions.} \end{cases} \quad (4.29)$$

Substitution of (4.29) into an appropriate integral equation ((4.16) or (4.17)), and using point matching gives the moment method linear system to be solved to complete the solution.

## 4.5 RWG Vector Basis Function and 3-D MM

### 4.5.1 RWG Vector Basis Function

In Section 4.3, the moment method was introduced to numerically find the induced current along 2-D surface profiles. For 2-D problems, the currents may be treated as unknown scalar functions. A simple scalar basis function set can therefore be chosen. The 3-D problem requires that the current be treated as a vector function since the current is not constrained in one dimension. An appropriate vector basis function set must therefore be used in the moment method solution of the integral equation(4.9) or (4.10).

The surface of a 3-D target is usually well represented using a triangular patch discretization. An example of a spilling breaker surface [63] is shown in Figure 4.5.

Rao-Wilton-Glisson (RWG) basis functions were specially developed by Rao *et al.* [120][121] for use with triangular patch surface models. Each RWG basis function  $\mathbf{f}_n$  is associated with a pair of adjacent triangles, as shown in Figure 4.6. The triangles are referred to as  $T_n^+$  and  $T_n^-$ , and the length of the common edge (the  $n$ -th edge of the complete patch model) is  $l_n$ .  $\rho_n^+$  is the vector from the free vertex of  $T_n^+$  to the position vector  $\mathbf{r}$  on  $T_n^+$ , and  $\rho_n^-$  is the counterpart on  $T_n^-$ , directed to the free vertex

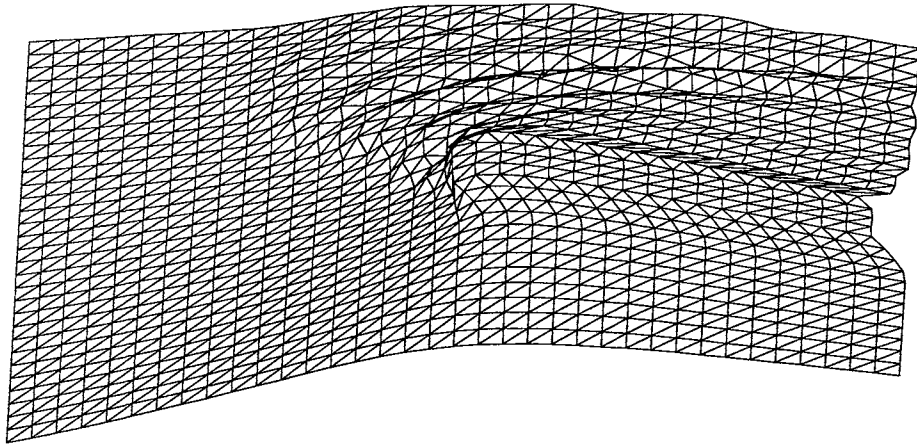


Figure 4.5: Triangular patch surface meshing.

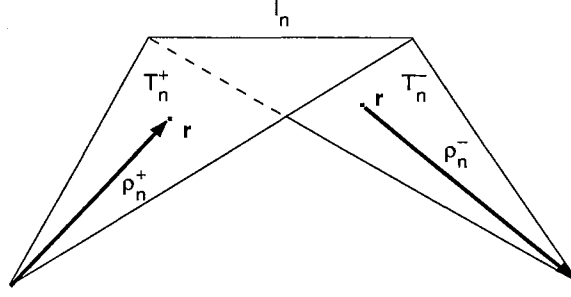


Figure 4.6: Triangular pair associated with RWG basis function definition.

of  $T_n^-$ . The RWG vector basis function  $\mathbf{f}_n$  is defined with respect to the common  $n$ -th edge as

$$\mathbf{f}_n(\mathbf{r}) = \begin{cases} \frac{l_n}{2A_n^+} \rho_n^+, & \mathbf{r} \text{ in } T_n^+, \\ \frac{l_n}{2A_n^-} \rho_n^-, & \mathbf{r} \text{ in } T_n^-, \\ 0 & \text{elsewhere.} \end{cases}, \quad (4.30)$$

where  $A_n^\pm$  is the area of triangle  $T_n^\pm$ . This definition of the RWG basis function forces the component of current normal to the  $n$ -th edge to be a constant associated with the size of the triangle pair connected by the edge, and the current is continuous across the edge.

The complete current on surface  $S$  thus can be approximated in terms of an expansion of the RWG basis functions for all interior edges

$$\mathbf{J} \approx \sum_{n=1}^N I_n \mathbf{f}_n(\mathbf{r}), \quad (4.31)$$

where  $N$  is the total number of interior edges of surface  $S$ , and the unknown coefficient  $I_n$  represents the normal component of the current density flowing across the  $n$ -th edge. The current tangential to the edge is approximated from the basis functions associated with the other two edges of triangular patch  $T_n^+$  and  $T_n^-$ . The total current on a triangular patch is the vector sum of three different basis function components associated with the three edges. Therefore, the current distribution over the entire surface can be described using these patch-based vector currents.

### 4.5.2 3-D Surface Moment Method

To apply the moment method to an impedance surface, the EFIE of (4.9) is rewritten as

$$E_{tan}^i(\mathbf{r}) = [j\omega\mathbf{A}(\mathbf{r}) + \nabla\Phi(\mathbf{r}) + \frac{1}{\epsilon}\nabla \times \mathbf{F}(\mathbf{r})]_{tan}, \quad \mathbf{r} \rightarrow S^-, \quad (4.32)$$

where  $\mathbf{r} \rightarrow S^-$  means that the equation is valid in the limit as  $\mathbf{r}$  approaches the surface  $S$  from the inside of the scatterer. From Glisson [114],

$$\lim_{\mathbf{r} \rightarrow S^-} [\frac{1}{\epsilon}\nabla \times \mathbf{F}(\mathbf{r})] = \lim_{\mathbf{r} \rightarrow S^-} [\frac{1}{4\pi}\nabla \times \int_S \mathbf{M}G dS'] = \frac{1}{2}\hat{n} \times \mathbf{M} - \frac{1}{4\pi} \oint_S \mathbf{M} \times G dS', \quad (4.33)$$

where  $\oint$  represents the Cauchy principal value integral,  $G$  is the free-space Green's function  $e^{-jkR}/R$ ,  $R = |\mathbf{r} - \mathbf{r}'|$ , and  $\mathbf{r}$  is a vector position on the surface. Applying the equivalent surface current relationship for an impedance boundary  $\hat{n} \times \mathbf{M} = Z_s \mathbf{J}$  and substituting (4.33) into (4.32), yields

$$\begin{aligned} E_{tan}^i = & [j\omega \frac{\mu}{4\pi} \int_S \mathbf{J}G dS' + \frac{1}{4\pi\epsilon} \nabla \int_S [\nabla' \cdot \mathbf{J}]G dS']_{tan} \\ & + [\frac{1}{2}Z_s \mathbf{J} + \frac{1}{4\pi} \oint_S Z_s(\hat{n}' \times \mathbf{J}) \times \nabla G dS']_{tan}. \end{aligned} \quad (4.34)$$

In order to suppress the edge diffractions, a resistive loading technique was introduced by Oh and Sarabandi[122]. An evaluation of resistive loading  $R(\mathbf{r})$  was given in [123], and will be introduced later. The addition of the resistive loading is accomplished by simply adding  $R(\mathbf{r})\mathbf{J}(\mathbf{r})$  to the right hand side of equation (4.34).

The moment method is applied by substituting (4.31) into (4.34). Galerkin's method, where the same function set used as the basis functions is used as the testing functions, is typically applied to RWG basis functions. The testing inner product is therefore defined as

$$\langle \mathbf{f}, \mathbf{g} \rangle = \int_S \mathbf{f} \cdot \mathbf{g} dS. \quad (4.35)$$

The definition in (4.30) leads to the useful approximate relationship

$$\int_{T_n^+ + T_n^-} \mathbf{f}_n dS \approx \frac{l_n}{2} (\rho_n^{c+} + \rho_n^{c-}) = l_n (\mathbf{r}_n^{c+} + \mathbf{r}_n^{c-}), \quad (4.36)$$

where  $\rho_n^{c\pm}$  is the vector between the free vertex and the centroid of  $T_n^\pm$  with  $\rho_n^{c-}$  directed towards and  $\rho_n^{c+}$  directed away from the vertex.  $\mathbf{r}_n^{c\pm}$  is the position vector of the centroid of  $T_n^\pm$ . After applying (4.36) and some approximations derived in [121] and [114], the corresponding testing terms can be obtained. Although the terms in (4.34) are complicated, they are linear integrodifferential operators, so each reduces to the sum of the products with respect to the unknown coefficient  $I_n$  after application of the RWG basis functions and Galerkin's method. Therefore, when setting the tested residual to zero, a linear system of equations is formed as

$$[Z_{mn}][I_n] = [V_m], \quad (4.37)$$

where

$$V_m = \langle \mathbf{E}^i, \mathbf{f}_m \rangle = l_m (\mathbf{E}_m^+ \cdot \frac{\rho_m^{c+}}{2} + \mathbf{E}_m^- \cdot \frac{\rho_m^{c-}}{2}), \quad (4.38)$$

$$\begin{aligned} Z_{mn} &= \langle j\omega \frac{\mu}{4\pi} \int_S \mathbf{J} G dS' + \frac{1}{4\pi\epsilon} \nabla \int_S [\nabla' \cdot \mathbf{J}] G dS', \mathbf{f}_m \rangle + \langle \frac{1}{2} Z_s \mathbf{J}, \mathbf{f}_m \rangle \\ &+ \langle \frac{1}{4\pi} \int_S Z_s (\hat{\mathbf{n}}' \times \mathbf{J}) \times \nabla G dS', \mathbf{f}_m \rangle \\ &= \sum_{n=1}^N I_n \{ l_m j\omega (\mathbf{A}_{mn}^+ \cdot \frac{\rho_m^{c+}}{2} + \mathbf{A}_{mn}^- \cdot \frac{\rho_m^{c-}}{2}) + \Phi_{mn}^- + \Phi_{mn}^+ \} \\ &+ \frac{1}{2} \sum_{n=1}^N I_n \{ \int_{T_m^+} Z_s [\mathbf{f}_n \cdot \mathbf{f}_m] dS + \int_{T_m^-} Z_s [\mathbf{f}_n \cdot \mathbf{f}_m] dS \} \\ &+ \frac{l_m}{2} \frac{1}{4\pi} \sum_{n=1}^N I_n \{ \int_s Z_s (\hat{\mathbf{n}}' \times \mathbf{f}_n) \times \nabla G(\mathbf{r}_m^{c+}, \mathbf{r}') dS' \cdot \rho_m^{c+} \\ &+ \int_s Z_s (\hat{\mathbf{n}}' \times \mathbf{f}_n) \times \nabla G(\mathbf{r}_m^{c-}, \mathbf{r}') dS' \cdot \rho_m^{c-} \}, \end{aligned} \quad (4.39)$$

and

$$\begin{aligned} \mathbf{A}_{mn}^\pm &= \frac{\mu}{4\pi} \int_s \mathbf{f}_n(\mathbf{r}') \frac{e^{-jkR_m^\pm}}{R_m^\pm} dS', \\ \Phi_{mn}^\pm &= \frac{-1}{4\pi j\omega\epsilon} \int_s \nabla'_s \cdot \mathbf{f}_n(\mathbf{r}') \frac{e^{-jkR_m^\pm}}{R_m^\pm} dS', \end{aligned}$$

$$R_m^\pm = |\mathbf{r}_m^{c\pm} - \mathbf{r}'|,$$

$$\mathbf{E}_m^\pm = \mathbf{E}^i(\mathbf{r}_m^{c\pm}),$$

and  $\mathbf{r}_m^{c\pm}$  are the centroid position vectors of  $T_m^\pm$ ,  $\rho_m^{c\pm}$  is the vector  $\rho_n^\pm(\mathbf{r})$  when  $\mathbf{r}$  is located at  $\mathbf{r}_m^{c\pm}$ .  $\mathbf{E}^i(\mathbf{r}_m^{c\pm})$  is the incident electric field at  $\mathbf{r}_m^{c\pm}$ .  $l_m$  is the length of the  $m$ -th edge.

With PEC surface scattering applications,  $Z_s = 0$  so the 3rd and 4th terms in the right side of (4.34) disappear. The integrations in the above equations are performed using the numerical quadrature techniques in [120].

Once the current distribution has been determined, the scattered fields are computed by the radiation equations. The far-field scattered electric field may be expressed as

$$\mathbf{E}^s = (-j\omega A_\theta - \frac{1}{\epsilon}jkF_\phi)\hat{\theta} + (-j\omega A_\phi + \frac{1}{\epsilon}jkF_\theta)\hat{\phi}, \quad (4.40)$$

where  $A_\phi$ ,  $A_\theta$  and  $F_\phi$ ,  $F_\theta$  are the components of  $\mathbf{A}$  and  $\mathbf{F}$  in the  $\phi$  and  $\theta$  direction respectively. The scattered electric field components are therefore given by

$$E_\theta^s = -jk\eta \frac{e^{-jkr}}{4\pi r} \int_s \mathbf{J} \cdot [\hat{\theta} + \frac{Z_s}{\eta}(\hat{\mathbf{n}}' \times \hat{\phi})] e^{jk(\hat{\mathbf{r}}' \cdot \mathbf{r})} dS', \quad (4.41)$$

$$E_\phi^s = -jk\eta \frac{e^{-jkr}}{4\pi r} \int_s \mathbf{J} \cdot [\hat{\phi} - \frac{Z_s}{\eta}(\hat{\mathbf{n}}' \times \hat{\theta})] e^{jk(\hat{\mathbf{r}}' \cdot \mathbf{r})} dS', \quad (4.42)$$

where  $\mathbf{r}$  is the unit vector pointing in the direction of the observation point. The polarization-dependent three-dimensional scattering cross-section then is found from [114]

$$\sigma_{\alpha\beta} = 4\pi r^2 \frac{|E_\alpha^s|^2}{|E_\beta^{inc}|^2}, \quad (4.43)$$

where  $\alpha$  and  $\beta$  represents either  $\theta$  or  $\phi$ .



## 4.6 Fast Multipole Method

### 4.6.1 Introduction

The moment method described in the previous section yields a system of  $N$  linear equations and  $N$  unknowns, where  $N$  is the number of interior edges in the triangular patch model.  $O(N^3)$  operations and  $O(N^2)$  memory storage are required to solve the matrix equation directly by LU factorization. Iterative solution requires  $O(N^2)$  operations per iteration. Doubling the dimensions of the 3-D scatterer increases the number of unknowns by a factor of four, thus increasing the number of interaction terms in the matrix by a factor of 16. The direct-solution order increases by a factor of 64, while iterative solution order increases by a factor of 16.

The primary computation expense of iterative solution is the evaluation of matrix-vector multiplies. Therefore, reduction of the complexity of this step yields more efficient solution. Wavelet transforms have been used in the moment method by choosing the multiresolution (MR) wavelet function to build the basis function set of MM [124][125][126]. The MR wavelet expansion can adaptively fit itself to the various length scales associated with the scatterer geometry. So this approach is best suited to the analysis of scatterers that contain a broad spectrum of length scale ranging from a subwavelength to several wavelengths. The moment-method matrix is sparsified by applying a threshold. Below the threshold, the elements of the matrix are set zero. Having a sparse matrix is appealing for linear system solutions to decrease storage requirements and execution time. However, there is no clear advantage to applying a wavelet transform on wavelike problems where the associated integral equations have an oscillatory kernel [127] [126]. Therefore, the applications of wavelet transform in the methods of moment is usually related to the electrostatic problems [128] [129].

For general scatterers, Coifman and Rokhlin *et al.* [50] proposed the fast multipole method (FMM) to reduce the computational expense of evaluating matrix-vector

multiplies. It divides the interaction matrix into near and far terms. The near terms are stored directly in a sparse matrix as in the standard moment method. The far interactions are computed each iteration using a multipole expansion that greatly reduces the number of computations and the memory needed to store the matrix information. A brief review of the fast multipole method is given here.

#### 4.6.2 Element Grouping and Far Interaction Approximation

The implementation of FMM is based on element grouping. The elements on a scatterer are first separated into different groups. The elements located in each group are electromagnetically near one another so the interaction between a pair of elements within the group is treated by the standard moment method. Two groups may also be near each other according to a specific criteria, so the interactions between elements which belong to two different near groups are also treated by standard MM. Otherwise, two groups are far from each other. The interactions between the elements of these groups are treated using a multipole expansion. The radiated fields from all elements within a group are simultaneously expanded in a plane wave expansion, relative to the center of the group. The entire expansion is then translated to the center of the other group simultaneously. Translating numerous elements simultaneously rather than individually gives FMM its speed advantage. Note that the radiation of an element must first be shifted to the center of the group before translation, and after translation is shifted to the desired receive element. This three step procedure is shown in Figure 4.7. The mathematical derivation of this procedure is now reviewed.

FMM is most easily introduced assuming scalar interactions between elements. The vector interactions will be added later. The scalar MM interaction matrix entry for two elements located at  $\mathbf{r}$  and  $\mathbf{r}'$  is

$$Z_{mn} = A \int d\mathbf{r} f_m(\mathbf{r}) \int d\mathbf{r}' f_n(\mathbf{r}') G(\mathbf{r}, \mathbf{r}'), \quad (4.44)$$

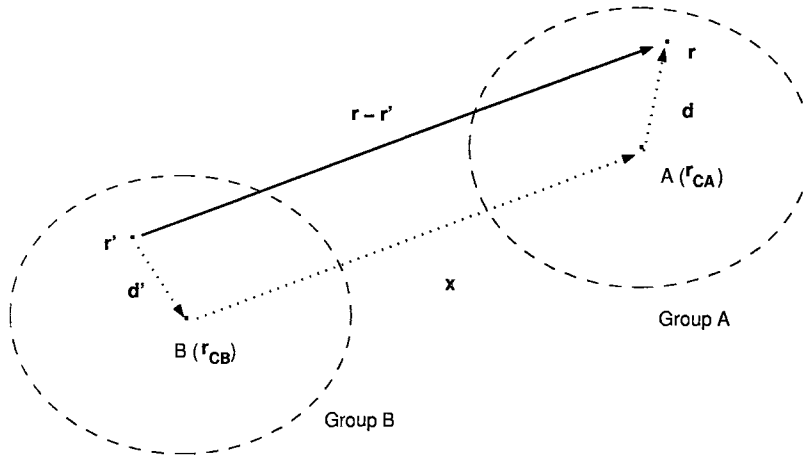


Figure 4.7: Vector relationship among elements and groups.

where  $G(\mathbf{r}, \mathbf{r}')$  is the scalar Green's function in (4.33), and  $A$  is a constant,  $f_m(\mathbf{r})$  and  $f_n(\mathbf{r})$  are the weighting and testing functions respectively. Using

$$\mathbf{r} - \mathbf{r}' = \mathbf{x} + \mathbf{d} \quad (4.45)$$

as defined in Figure 4.8, the Green's function is

$$G(\mathbf{r}, \mathbf{r}') = \frac{e^{-jk|\mathbf{r}-\mathbf{r}'|}}{|\mathbf{r}-\mathbf{r}'|} = \frac{e^{-jk|\mathbf{x}+\mathbf{d}|}}{|\mathbf{x}+\mathbf{d}|}. \quad (4.46)$$

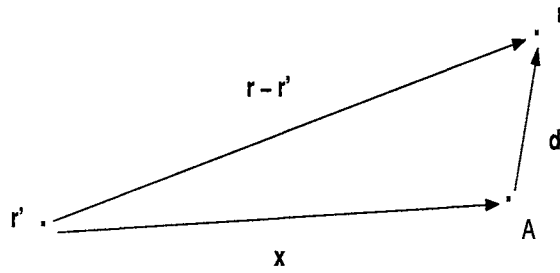


Figure 4.8: Relationship between vector  $\mathbf{r}'$ ,  $\mathbf{r}$ ,  $\mathbf{x}$  and  $\mathbf{d}$ .

The last term in (4.46) can be expressed by a series expansion in the form of Gegenbauer's addition theorem as [50] [130][131]

$$\frac{e^{-jk|\mathbf{x}+\mathbf{d}|}}{|\mathbf{x}+\mathbf{d}|} = \frac{-jk}{4\pi} \int d^2\hat{k} e^{-j\mathbf{k}\cdot\mathbf{d}} \sum_{l=0}^{\infty} (-j)^l (2l+1) h_l^{(2)}(k|\mathbf{x}|) P_l(\hat{k} \cdot \hat{\mathbf{x}}), \quad (4.47)$$

where  $h_l^{(2)}$  is the spherical Hankel function of the second kind, and  $P_l$  is the Legendre polynomial. (4.47) is valid when  $|\mathbf{d}| < |\mathbf{x}|$ . In a numerical implementation, only a finite number terms of the expansion are kept. Note that the series is a function of  $k|\mathbf{x}|$  and  $\hat{k} \cdot \hat{\mathbf{x}}$ . The truncated multipole series expansion is therefore denoted as  $T_L(k|\mathbf{x}|, \hat{k} \cdot \hat{\mathbf{x}})$ , and termed the translation operator. Thus,

$$T_L(k|\mathbf{x}|, \hat{k} \cdot \hat{\mathbf{x}}) = \sum_{l=0}^L (-j)^l (2l+1) h_l^{(2)}(k|\mathbf{x}|) P_l(\hat{k} \cdot \hat{\mathbf{x}}), \quad (4.48)$$

where  $L$  is the number of terms retained. Applying (4.48) into (4.47) yields

$$\frac{e^{-jk|\mathbf{x}+\mathbf{d}|}}{|\mathbf{x}+\mathbf{d}|} \approx \frac{-jk}{4\pi} \int d^2\hat{k} e^{-j\mathbf{k}\cdot\mathbf{d}} T_L(k|\mathbf{x}|, \hat{k} \cdot \hat{\mathbf{x}}). \quad (4.49)$$

Substituting (4.49) into (4.46), then into (4.44), yields

$$Z_{mn} = B \int d\mathbf{r} f_m(\mathbf{r}) \int d\mathbf{r}' f_n(\mathbf{r}') \int d^2\hat{k} e^{-j\mathbf{k}\cdot\mathbf{d}} T_L(k|\mathbf{x}|, \hat{k} \cdot \hat{\mathbf{x}}), \quad (4.50)$$

where  $B$  is a constant.

(4.50) only represents the interaction between two far elements since it applied the approximation relationship of (4.49), so it is also denoted as  $Z_{mn}^{far}$ .

Referring back to Figure 4.7, letting

$$\mathbf{x} = \mathbf{r}_{CA} - \mathbf{r}_{CB} \quad (4.51)$$

in (4.45) gives

$$\mathbf{d} = \mathbf{r} - \mathbf{r}' - \mathbf{x} = \mathbf{r} - \mathbf{r}' - (\mathbf{r}_{CA} - \mathbf{r}_{CB}) = (\mathbf{r} - \mathbf{r}_{CA}) - (\mathbf{r}' - \mathbf{r}_{CB}). \quad (4.52)$$

Substituting  $\mathbf{d}$  in (4.52) into (4.50) yields

$$\begin{aligned} Z_{mn} = B \int d^2 \hat{k} [ & \int d\mathbf{r} (f_m(\mathbf{r}) e^{-j\mathbf{k} \cdot (\mathbf{r} - \mathbf{r}_{CA})})] \\ & [\int d\mathbf{r}' (f_n(\mathbf{r}') e^{j\mathbf{k} \cdot (\mathbf{r}' - \mathbf{r}_{CB})})] T_L(k|\mathbf{r}_{AB}|, \hat{k} \cdot \mathbf{r}_{AB}). \end{aligned} \quad (4.53)$$

Shifting operators are now defined as

$$V_{fm\alpha}(\hat{k}) = \int d\mathbf{r} [f_m(\mathbf{r}) e^{-j\mathbf{k} \cdot (\mathbf{r} - \mathbf{r}_{CA})}],$$

$$V_{sm\alpha}(\hat{k}) = [V_{fm\alpha}(\hat{k})]^*.$$

(4.53) can now be written as

$$Z_{mn} = B \int d^2 \hat{k} [V_{fm\alpha}(\hat{k})] T_L(k|\mathbf{r}_{AB}|, \hat{k} \cdot \mathbf{r}_{AB}) [V_{sm\alpha'}(\hat{k})] \quad (4.54)$$

(4.54) shows the three-step procedure FMM uses to represent the interactions between the source element at  $\mathbf{r}'$  in group B to the observation element at  $\mathbf{r}$  in group A. The shift from the source element to the source group center  $\mathbf{r}_{CB}$  is represented by the shifting operator  $V_{sm\alpha'}(\hat{k})$ , the translation from  $\mathbf{r}_{CB}$  to the observation group center  $\mathbf{r}_{CA}$  is represented by the translation operator  $T_L(k|\mathbf{r}_{AB}|, \hat{k} \cdot \mathbf{r}_{AB})$ , and the shift from  $\mathbf{r}_{CA}$  to the observation element  $\mathbf{r}$  is represented by the second shifting operator  $V_{fm\alpha}(\hat{k})$ . Note that the translation operator need be applied once for all elements in two far groups, and the same translation operator can be used for all group pairs that are spaced same, giving the computational advantage of FMM. This advantage together with the sparsity of the near-interaction matrix greatly reduces

both the computational complexity and the memory. As mentioned before, FMM also includes near element interactions  $Z_{mn}^{near}$  separately, which can be obtained as the standard moment method does. Therefore, the final linear system of an FMM scheme can be described as

$$V_m = \sum_{near\ elements} Z_{mn}^{near} I_n + \sum_{far\ elements} Z_{mn}^{far} I_n \quad (4.55)$$

There is a tradeoff between the size of the groups and the computational efficiency. Larger groups force more interactions into the near/sparse matrix, which do not benefit from the FMM improvement. Large groups also require more terms be included in the multipole expansion since the coefficients of the combined multipole expansion at the group center need to preserve enough accuracy to represent the specific contribution from the individual elements. This requires the number of coefficients in the multipole expansion corresponding to each element be increased. A semi-empirical formula for the number of terms needed in the expansion was determined in [54].

$$L = 2k\rho_{max} + \frac{D}{1.6} \ln(2k\rho_{max} + \pi), \quad (4.56)$$

where  $k$  is the wave number,  $\rho_{max}$  is the maximum group radius among all groups, and  $D$  is the desired number of significant digits of accuracy. The criteria for determining if groups are near or far is

$$k|\mathbf{r}_{AB}| \begin{cases} \geq L, & \Rightarrow \text{group A and group B are far groups,} \\ < L, & \Rightarrow \text{group A and group B are near groups,} \end{cases} \quad (4.57)$$

where  $|\mathbf{r}_{AB}|$  denotes the distance between the centers of group A and B.

### 4.6.3 Physical Insight of FMM

The translation operator  $T_L()$  and the shifting operators  $V_{f\mathbf{m}\alpha}()$  and  $V_{s\mathbf{m}\alpha'}()$  are functions of the vector wave number  $\hat{k}$ , over which a continuous integration must be evaluated to obtain  $Z_{mn}$  in (4.54). The integration is numerically performed in FMM by Gauss-Legendre quadrature in the spherical  $\theta$  coordinate and by trapezoidal quadrature in the  $\phi$  coordinate [132]. In this, the function is sampled at discrete wave number samples of  $\hat{k}$ . The samples of wave number  $\hat{k}$  are uniformly spaced in the azimuthal dimension ( $\phi$  coordinate), allowing a trapezoidal quadrature rule on the interval  $[0, 2\pi]$ . In the elevation dimension ( $\theta$  coordinate), the samples of  $\hat{k}$  relate to the nodes of a Gauss-Legendre quadrature polynomial [132], allowing the Gaussian quadrature. Sampling theory requires at least  $2L$  samples in  $\phi$  dimension and  $L$  samples in  $\theta$  dimension [54]. The integration (4.54) is numerically evaluated as

$$\int d^2\hat{k} f(\hat{k}) = \int_0^{2\pi} \int_0^\pi f(\theta, \phi) \sin \theta d\theta d\phi = \sum_{i=1}^L \sum_{j=1}^{2L} \omega_i^g \omega_j^c f(\theta_i, \phi_j), \quad (4.58)$$

where  $\theta_i$  is a Gauss-Legendre point,  $\phi_i$  is an equally spaced point,  $\omega_i^g$  and  $\omega_j^c$  are their relative quadrature weights, respectively. The integration over  $\phi$  can therefore be implemented using an FFT, and the remaining part with respect to  $\theta$  requires explicit evaluation [54].

As mentioned, the derivations provided so far assumed a scalar Green's function. The radiated vector electric field is related to the vector current through the vector Green's function. (4.1) to (4.4) show that the vector fields are described by both vector and scalar potentials, and the potentials relate to vector current via scalar Green's function  $G(\mathbf{r}, \mathbf{r}')$ . The vector Green's function can therefore be expressed [50] as

$$\mathbf{G}(\mathbf{r} - \mathbf{r}') = (\mathbf{I} + \frac{1}{k^2} \nabla \nabla') G = \left( \delta_{jj'} - \frac{1}{k^2} \frac{\partial}{\partial r_j} \frac{\partial}{\partial r_{j'}} \right) \frac{e^{-jk|\mathbf{r}-\mathbf{r}'|}}{4\pi|\mathbf{r}-\mathbf{r}'|}, \quad (4.59)$$

where the indices  $j, j'$  label Cartesian components. Substituting (4.49) into (4.59)

yields

$$\mathbf{G}(\mathbf{x} + \mathbf{d}) \approx \frac{-jk}{4\pi} \int d^2\hat{k} (\delta_{jj'} - \hat{k}_j \hat{k}_{j'}) e^{-j\mathbf{k} \cdot \mathbf{d}} T_L(k|\mathbf{x}|, \hat{k} \cdot \hat{\mathbf{x}}). \quad (4.60)$$

Furthermore, replacing the scalar Green's function with (4.60) into (4.44) and applying RWG vector basis function  $\mathbf{f}_m(\mathbf{r})$  and  $\mathbf{f}_n(\mathbf{r})$  simultaneously gives the vector expression of the MM interaction matrix entry as

$$Z_{mn} = B \int d^2\hat{k} \left\{ \int d\mathbf{r} [\mathbf{f}_m(\mathbf{r}) - \hat{k}(\hat{k} \cdot \mathbf{f}_m(\mathbf{r}))] e^{-j\mathbf{k} \cdot (\mathbf{r} - \mathbf{r}_{CA})} \right\} \left\{ \int d\mathbf{r}' [\mathbf{f}_n(\mathbf{r}') - \hat{k}(\hat{k} \cdot \mathbf{f}_n(\mathbf{r}'))] e^{j\mathbf{k} \cdot (\mathbf{r}' - \mathbf{r}_{CB})} \right\} T_L(k|\mathbf{r}_{AB}|, \hat{k} \cdot \mathbf{r}_{AB}). \quad (4.61)$$

From (4.61), the vector shifting operator is therefore defined as

$$\mathbf{V}_{fm\alpha}(\hat{k}) = \int d\mathbf{r} [\mathbf{f}_m - \hat{k}(\hat{k} \cdot \mathbf{f}_m(\mathbf{r}))] e^{i\mathbf{k} \cdot (\mathbf{r} - \mathbf{r}_{Cm})}, \quad (4.62)$$

and  $\mathbf{V}_{sm\alpha}(\hat{k}) = [\mathbf{V}_{fm\alpha}(\hat{k})]^*$  is still valid.

When finite conductivity surfaces are treated using impedance boundary conditions, the EFIE in (4.34) yields

$$\mathbf{V}_{sm\alpha}(\hat{k}) = \int d\mathbf{r} [\mathbf{f}_n - \hat{k}(\hat{k} \cdot \mathbf{f}_n(\mathbf{r}))] e^{-i\mathbf{k} \cdot (\mathbf{r} - \mathbf{r}_{Cm})}, \quad (4.63)$$

$$\mathbf{V}_{fm\alpha}(\hat{k}) = \int d\mathbf{r} [\mathbf{f}_n - \hat{k}(\hat{k} \cdot \mathbf{f}_n(\mathbf{r}))] e^{i\mathbf{k} \cdot (\mathbf{r} - \mathbf{r}_{Cm})} - \frac{Z_s}{\eta} \hat{k} \times \int d\mathbf{r} [\mathbf{f}_n(\mathbf{r}) \times \hat{n}] e^{i\mathbf{k} \cdot (\mathbf{r} - \mathbf{r}_{Cm})}, \quad (4.64)$$

where  $\hat{n}$  is the unit vector external normal to the surface of the triangle over which the integration is being performed. The translation operator  $T_L()$  remains unchanged for a PEC or an impedance surface.

FMM can now be summarized as a sparse decomposition of the dense moment method impedance matrix  $Z$  given by

$$Z = Z' + UTV \quad (4.65)$$



where  $Z', U, T$  and  $V$  all are sparse matrices.  $Z'$  includes the interaction between near elements. The matrix  $UTV$  is the FMM decomposition of the far terms of  $Z$ .  $U$  and  $V$  are both block-diagonal matrices [133].  $V$  translates the plane waves from the individual elements to their group center, and  $U$  translates the waves from the center of group to individual elements which belong to this group. The sparse matrix  $T$  translates the plane waves of all elements in one group to another group only once.

When the total number of unknowns is  $N$ , it can be shown that the cost of FMM is minimized by choosing the number of groups  $M \approx \sqrt{N}$ , giving a total cost of  $O(N^{3/2})$  for the FMM matrix-vector multiply [133]. This is a significant improvement compared to  $O(N^2)$  cost of standard dense moment method iterative solutions.

## 4.7 Multilevel Fast Multipole Algorithm

### 4.7.1 Introduction

Multilevel Fast Multipole Algorithm (MLFMA) is the natural extension of the FMM technique when large surfaces are under consideration. The concept of levels is used in MLFMA to describe the relationship between groups. In fact, in the FMM implementation discussed in the previous section can be thought of as two levels as shown in Figure 4.9. The upper level ( $L_1$ ) includes the FMM groups, and the lower level ( $L_0$ ) includes the individual FMM elements. MLFMA extends the level concept.

In MLFMA, the groups in the original level  $L_1$  are combined into larger parent groups at the next higher level, similar to the grouping of the elements into groups at the lowest level. This can continue upward to still higher levels, forming a tree as shown in Figure 4.10. The advantage of this approach is that the translation matrix  $T$  becomes more efficient as the level increases since more elements are translated at once. Also, elements which are contained within groups that are too close together at the highest level may be translated at a lower level where the groups are smaller.

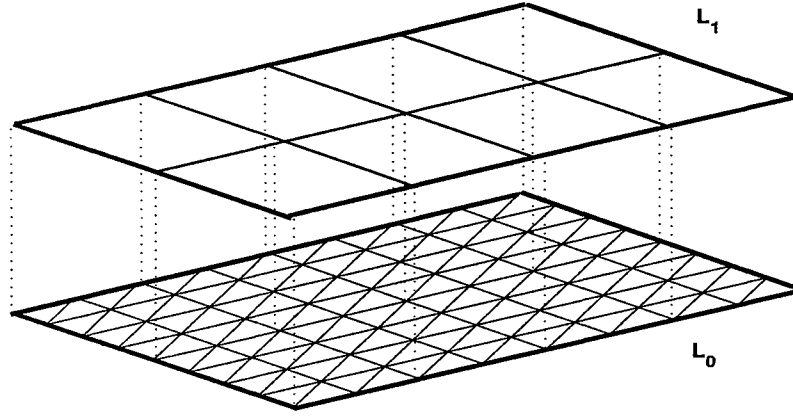


Figure 4.9: Two levels structure in FMM technique.

As mentioned in FMM grouping, larger groups require more terms be included in the multipole expansion. Following the upward tree, the groups in a level are formed by combining the smaller groups at the next lower level. To preserve the accuracy of the source expansion as groups are combined, the combined multipole expansion at the group center requires more higher-order multipole expansion terms be used. This is accomplished through interpolation. On the other hand, when the plane waves follow the downward tree after translation, the multipole expansion at each smaller group center requires fewer terms than in the parent group. The parent group expansion is therefore filtered into lower-order expansions centered at each child group.

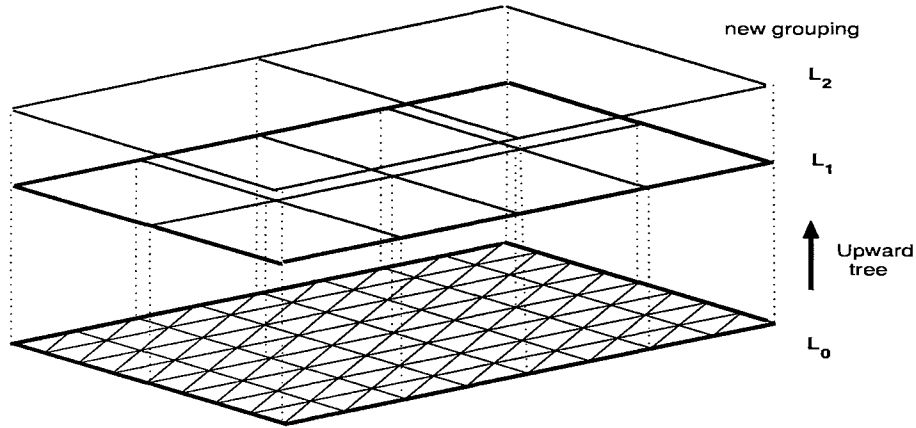


Figure 4.10: Upward tree multilevel structure in MLFMA technique.

## 4.7.2 Mathematical Derivation

The multilevel grouping structure is built using the aforementioned re-grouping method.

If there are  $n$  FMM levels in the tree, the indices of the FMM levels are numbered from  $L_1$  to  $L_n$ . The lowest level ( $L_0$ ) is the element level, in which FMM is not used.

Following the FMM principle, a series of plane waves are synthesized associated with discrete sampling of  $\hat{k}$ . In level  $L_1$ , the plane wave of group  $m'_{L_1}$  is expressed as

$$S_{m'_{L_1}}(\hat{k}_{L_1}) = \sum_{\alpha'_{L_1} \in G_{m'_{L_1}}} \mathbf{V}_{sm'_{L_1}\alpha'_{L_1}}(\hat{k}_{L_1}) I_{m'_{L_1}\alpha'_{L_1}} \text{ for } m'_{L_1} = 1, 2, \dots, M_{L_1}, \quad (4.66)$$

where  $\alpha'_{L_1}$  stands for the elements which belong to group  $m'_{L_1}$ ,  $G_{m'_{L_1}}$  is the set of all groups near to group  $m'_{L_1}$ ,  $M_{L_1}$  is the total group number at level  $L_1$ .  $I_{m'_{L_1}\alpha'_{L_1}}$  is the contribution from the element  $\alpha'_{L_1}$ ,  $\mathbf{V}_{sm'_{L_1}\alpha'_{L_1}}()$  is the shifting operator that translates the plane wave from the individual elements to the group center. Therefore,  $S_{m'_{L_1}}(\hat{k}_{L_1})$  represents the plane wave at the group center. It is the coherent sum of the contributions from the individual elements that belong to the near groups. Using translation operator  $T_L()$ ,  $S_{m'_{L_1}}(\hat{k}_{L_1})$  can be mapped onto other groups which belong to the same level.

At higher level  $L_l$  ( $L_n \geq L_l \geq L_2$ ), the multipole expansion may be synthesized from the plane wave multipole expansion of its child groups at the next lower level. This is mathematically written as

$$S_{m'_{L_l}}(\hat{k}_{L_l}) = \sum_{\text{child groups}} e^{-j\mathbf{k} \cdot (\hat{\mathbf{r}}_{cm'_{L_l}} - \hat{\mathbf{r}}_{cm'_{L_{l-1}}})} \sum_1^{k_{L_{l-1}}} \omega_{L_{l-1}, L_l} [S_{m'_{L_{l-1}}}(\hat{k}_{L_{l-1}})], \quad (4.67)$$

where  $S_{m'_{L_{l-1}}}(\hat{k}_{L_{l-1}})$  is the plane wave component of a child group in the  $\hat{k}_{L_{l-1}}$  direction,  $e^{-j\mathbf{k} \cdot (\hat{\mathbf{r}}_{cm'_{L_l}} - \hat{\mathbf{r}}_{cm'_{L_{l-1}}})}$  is a shifting factor which shifts the plane wave reference from the child group center  $\mathbf{r}_{cm'_{L_{l-1}}}$  to the parent group center  $\mathbf{r}_{cm'_{L_l}}$ , and  $\omega_{L_{l-1}, L_l}$  is a transform coefficient which interpolates the plane waves in the directions  $\hat{k}_{L_{l-1}}$  into

the directions  $\hat{k}_{L_l}$ . Note that more plane waves are needed at the higher level due to the larger group size, as explained in Section 4.6.2, thus giving the need for the interpolation. The interpolation in the  $\phi$  direction is performed using an FFT, while the  $\theta$  interpolation is performed using a discrete Legendre transform. The formation of multipole expansions moving up the tree is termed the aggregation process.

At the highest level ( $L_n$ ), the translation operator  $T_L()$  is used to translate the references of the plane waves from the center of the source group to the center of the observation group using

$$g_{m_{L_n}}(\hat{k}_{L_n}) = \sum_{m'_{L_n} \in D_{m_{L_n}}} T_L(m, m', \hat{k}_{L_n}) S_{m'_{L_n}}(\hat{k}_{L_n}), \quad (4.68)$$

where  $S_{m'_{L_n}}(\hat{k}_{L_n})$  is the plane wave radiated from group  $m'_{L_n}$ ,  $g_{m_{L_n}}(\hat{k}_{L_n})$  is the received plane wave by group  $m_{L_n}$ , and  $D_{m_{L_n}}$  is the group set consisting of all groups far from group  $m_{L_n}$ .

The plane waves at the observation group at the highest level  $g_{m_{L_n}}(\hat{k}_{L_n})$  must be decomposed and mapped on the child groups level by level. A process similar to the aggregation process is employed on the downward tree, termed disaggregation. Mathematically it is given by

$$g_{m_{L_{l-1}}}(\hat{k}_{L_{l-1}}) = \sum_{m'_{L_l} \in D_{m_{L_l}}} e^{-j\mathbf{k} \cdot (\hat{\mathbf{r}}_{cm'_{L_{l-1}}} - \hat{\mathbf{r}}_{cm'_{L_l}})} \sum_1^{k_{L_l}} \omega_{L_l, L_{l-1}}[g_{m'_{L_l}}(\hat{k}_{L_l})], \quad (4.69)$$

where  $g_{m'_{L_l}}(\hat{k}_{L_l})$  is the plane wave from the group  $m'_{L_l}$  at parent group level  $L_l$ ,  $e^{-j\mathbf{k} \cdot (\hat{\mathbf{r}}_{cm'_{L_{l-1}}} - \hat{\mathbf{r}}_{cm'_{L_l}})}$  is a shifting factor which shifts the plane wave from the parent group center  $\mathbf{r}_{cm'_{L_l}}$  to a child group center  $\mathbf{r}_{cm'_{L_{l-1}}}$ ,  $\omega_{L_l, L_{l-1}}$  is a transform coefficient which transforms the plane waves in the directions  $\hat{k}_{L_l}$  into the directions  $\hat{k}_{L_{l-1}}$ . Since fewer plane-wave components are needed at the lower level, the resampling operation, termed filtering, is used in the disaggregation stage. The filtering operation is also

implemented using an FFT in the  $\phi$  dimension and a discrete Legendre transform in the  $\theta$  dimension.

Once the disaggregation process reaches the finest group level ( $L_1$ ), the plane wave of the observation group at level  $L_1$  must be transformed onto the individual observation element through the shifting operator  $\mathbf{V}_{fm\alpha}(\cdot)$ . Hence, the final expression of MLFMA can be written as

$$V_{m\alpha} = \sum_{m' \in B_m} Z_{m\alpha m' \alpha'} I_{m' \alpha'} + \frac{\omega \mu k}{(4\pi)^2} \int d^2 \hat{k} \{ \mathbf{V}_{fm\alpha}(\hat{k}_{L_1}) \cdot g_{L_1}(\hat{k}_{L_1}) \}, \quad (4.70)$$

where  $V_{m\alpha} = \langle \mathbf{E}^i, \mathbf{f}_{m\alpha} \rangle$  is the MM test term with respect to the incident field, and  $B_m$  is the set of all groups near to group  $m'$ . Therefore the first term of (4.70) stands for the near element interactions, while the second term represents the interaction between far elements.

As levels are added, the computational cost of MLFMA converges to  $O(N \log N)$  [134]. However the interpolation and filtering operations add overhead so that MLFMA may be at a disadvantage to the  $O(N^{(3/2)})$  FMM when small  $N$  systems are considered. However the advantage of MLFMA is considerable when  $N$  is large.

## 4.8 Surface Truncation and Edge Treatment

As mentioned in Section 4.4, finite computer resources limit the size of the surface that can be modeled. Thus, the surface must be truncated, giving artificial edge diffraction that affects the calculated cross-section if the edges are not treated. In this work, resistive loading of the edges was used to suppress edge effects. This was first used by Oh and Sarabandi [122], who applied a power-law taper to the edges of 2-D surfaces. West [123] used the Taylor weighting taper of Haupt and Liepa [135], and found it is superior to the power-law weighting and also showed that this approach is best suited to the surfaces whose end section can be tilted away from horizontal

without significantly affecting the dominant scattering mechanisms. Finally, Zhao and West [72] extended the resistive tapering approach to the 3-D MLFMA surface scattering problem. That is the approach used here.

The resistive loading  $R(\mathbf{r})$  for the Taylor loading taper takes the form

$$R(\mathbf{r}) = \begin{cases} \eta_0 \left\{ \frac{1}{J(\mathbf{r})} - \frac{1}{2} \right\} & \text{loading area,} \\ 0 & \text{otherwise} \end{cases} \quad (4.71)$$

where

$$J(\mathbf{r}) = \frac{1}{2a} \left[ 1 + 2 \sum_{n=1}^{\bar{n}-1} f(n) \cos \left( \frac{\pi n |\mathbf{r} - \mathbf{r}_0|}{a} \right) \right],$$

$$f(n) = \frac{[(\bar{n} - 1)!]^2}{(\bar{n} - 1 + n)! (\bar{n} - 1 - n)!} \prod \left( 1 - \frac{n^2}{w_m^2} \right),$$

$$w_m = \begin{cases} \bar{n} \sqrt{\frac{A^2 + (m - 0.5)^2}{A^2 + (\bar{n} - 0.5)^2}} & |n| < \bar{n}, \\ n & |n| \geq \bar{n}. \end{cases},$$

and  $\eta_0$  is the intrinsic impedance of free space,  $\bar{n}$  is the number of sidelobes desired in the scattering pattern at a level of  $q$  dB below the main reflection,

$$A = \frac{1}{\pi} \cosh^{-1}(10^{q/20}),$$

$a$  is the distance over which the loading is applied, and  $\mathbf{r}_0$  is the position where the loading begins.

Figure 4.11 shows the geometry of the resistive loading applied to a flat plate. The loading is applied entirely around the perimeter of the surface. As the thick arrows show in Figure 4.11, the taper of (4.71) is applied with increasing  $d$  from the inner edge of the loaded region to the outer edge. This scheme ensures that the loading is continuous everywhere. As introduced in [72], a Taylor-based weighting with  $q = 90$

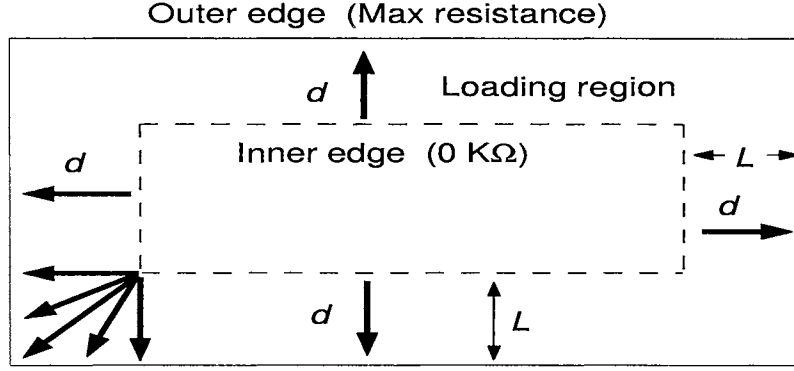


Figure 4.11: Illustration of 2-D resistive loading.

and  $\bar{n} = 9$  are used here. The loading tapers smoothly from  $0 \Omega$  at the inner edge and reaches the maximum at the outer edge.

## 4.9 Iterative Solver and Preconditioning

The far interactions in an MLFMA expansion are implemented using (4.70). The interactions are not stored as in the standard MM as this would remove the advantages of MLFMA. Instead, (4.70) is used to find the interactions between groups of elements as that are needed in an iterative solution procedure. Thus, MLFMA is used to dramatically accelerate the matrix-vector product used by the iterative solvers. Several iterative solution algorithms are available for the complex non-Hermitian matrices that result from RWG basis functions, including generalized conjugate gradient (GCG), conjugate gradient-normal equation (CGNR), biconjugate gradient (BICG), quasi-minimum residual (QMR), biconjugate gradient-stable (BICGSTAB) and general minimum residual (GMRES) etc. The details of these algorithms are found in [136] [137]. Here we use GMRES since it requires only one matrix-vector multiply per iteration and converges more quickly than the others for general problems [138].

The EFIE of equations (4.9) possess a strong singularity. This leads to a poorly conditioned interaction matrix, which leads to slow convergence of the iterative al-

gorithm. Preconditioning is therefore widely used to improve the iterative efficiency. Preconditioning improves the condition of the system matrix by changing the singularity distribution [139]. Incomplete LU factorization with a dual threshold drop strategy and pivoting (ILUTP) is chosen due to its robustness and efficiency [136] [140]. The preconditioner can be simply set up based on the incomplete LU factorization of the near-interaction sparse matrix. However, an additional reduction of the computational complexity is achieved by dropping preconditioner matrix element if its two related elements are spaced greater than a distance parameter  $d$ . A smaller value of  $d$  increases the sparsity of the preconditioning matrix, giving more rapid ILU factoring. Larger  $d$  may be used with particularly badly conditioned linear systems, increasing the factoring time and decreasing the required number of iterations.

Zhao and West [141] developed the 3-D MLFMA routines and applied them to analyze the backscattering from the spilling breaker crest of Figure 4.5. All 3-D scattering results provided in this paper are computed using this MLFMA codes.

## 4.10 Cube Element Grouping

Figure 4.12 shows the cubical grouping scheme used with MLFMA. The synthesis of the 3-D plunging breaker test profile is described in Section 5.1. The size of the surface is about  $11\lambda$ ,  $15\lambda$  and  $5\lambda$  in  $x$ ,  $y$  and  $z$  directions, respectively. There are about 109100 interior edges (unknowns) when the surface is meshed using the triangular patch model. The element grouping is formed by dividing space into cubical regions, as shown in the figure. Edges falling within the same cube are included within the same FMM group at that level.

Note that the elements on the overturning section of the wave are very close to one another. Therefore, numerous elements are contained within a single group. Other groups contain fewer elements, and cubes that contain no elements are ignored. Note that smaller cubes are combined into larger cubes as the level of the MLFMA



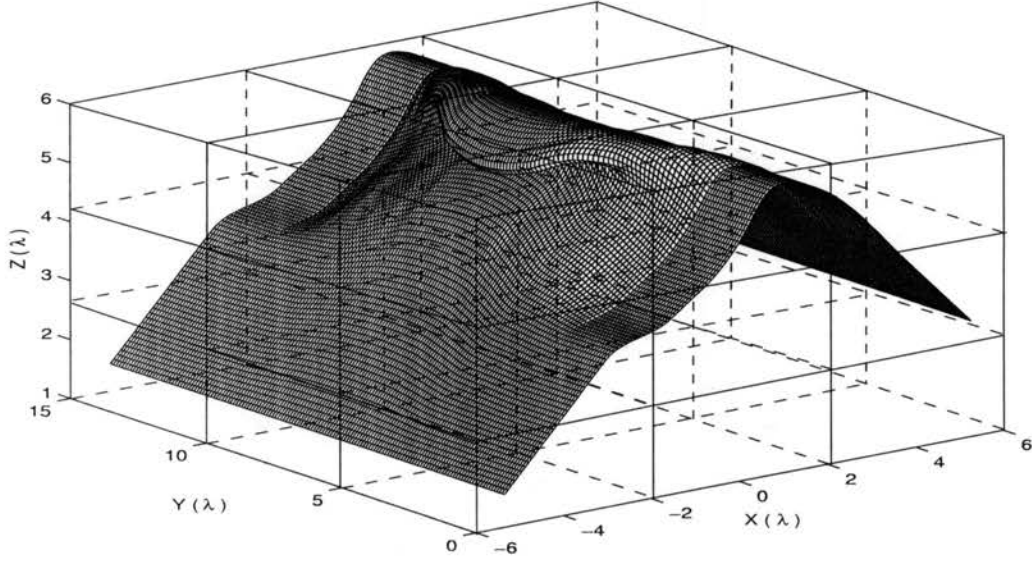


Figure 4.12: Demonstration of the cube grouping scheme.

expansion increases.

## 4.11 Test Case: Scattering from Impedance Flat Plate

In this section, the scattering from an impedance boundary flat plate is discussed to confirm the validity of the numerical technique and to establish some basic vector scattering concepts, including the induced current distribution and the corresponding polarimetric scattering cross-sections. As shown in Figure 4.13, the test truncated impedance flat plate is of  $12\lambda$  by  $9\lambda$  in area. The impedance was determined from a complex dielectric constant of  $65 - j40$  that of sea water at 10 GHz. The resistive loading to suppress the edge diffraction was applied over widths of  $2\lambda$  on each side. The scattering geometry is shown in the left upper corner of Figure 4.13. The scattering when  $\phi_i = \phi_s = 0^\circ$  and  $\theta_i = \theta_s$  is termed on-axis backscattering. “Off-axis” backscattering occurs when  $\phi_i = \phi_s \neq 0^\circ$ , and  $\theta_i = \theta_s$ . Bistatic scattering occurs when either  $\phi_i \neq \phi_s$  or  $\theta_i \neq \theta_s$ .

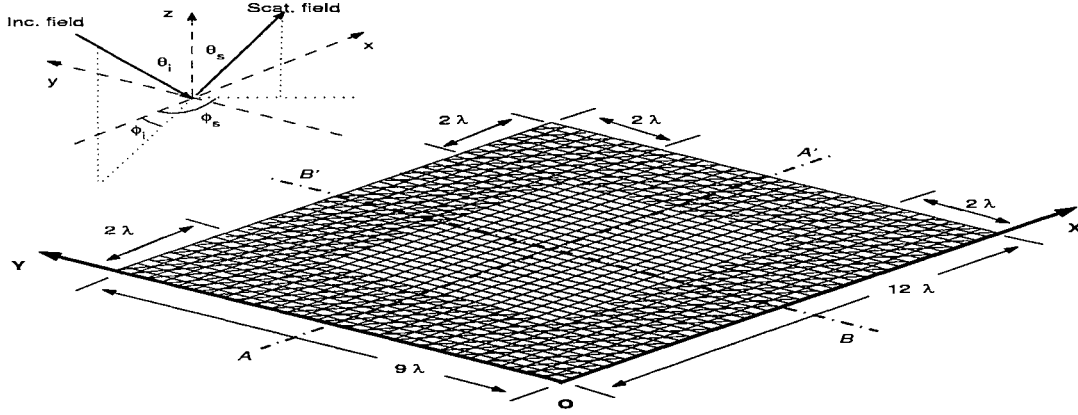
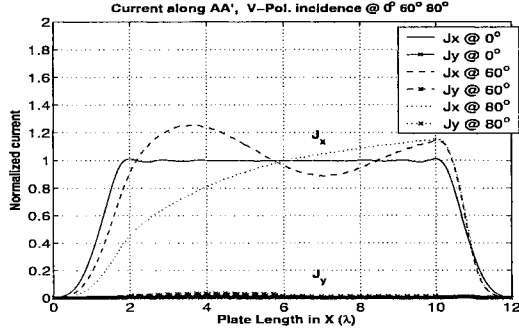


Figure 4.13: The truncated flat sea surface.

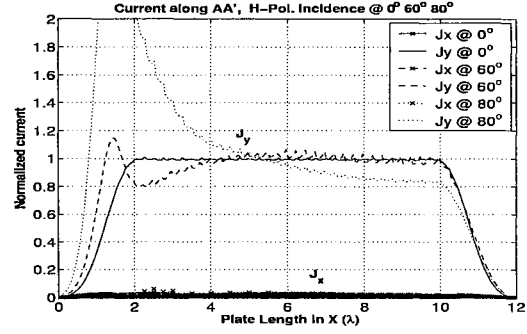
### • Induced Currents

As mentioned, MLFMA finds the current induced on the scatterer that is then re-radiated to give the scattered field. Errors in the current distribution therefore yield errors in the calculated scattering cross-section. Figure 4.14 shows the induced current distributions along two central lines ( $AA'$  in X direction,  $BB'$  in Y direction) when a plane wave is incident on the plate at  $\phi_i = 0^\circ$  (on-axis) and  $\theta_i = 0^\circ, 60^\circ$  and  $80^\circ$ . Both vertical and horizontal polarizations are shown. The currents are normalized to the level that would flow on an infinitely extending planar impedance boundary (*i.e.* the physical optics current).

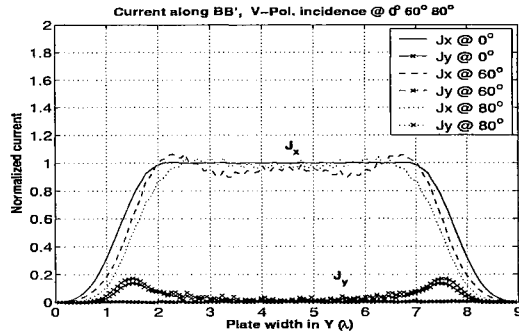
As expected, the currents in Figure 4.14 are strongest in the direction of an applied electric field component (the X direction along  $AA'$  for vertical polarization and the Y direction along  $BB'$  for horizontal polarization). As a reference, the current distribution on the same impedance plate, without edge resistive loading, is shown in Figure 4.15. Part(a) is the current along  $AA'$  for vertical polarized incidence and part(b) is the current along  $BB'$  for horizontal polarized incidence, they correspond to part(a) and part(d) in Figure 4.14, respectively. Figure 4.15 shows that the edge diffraction induced current oscillations in each case, and the induced currents are strongest near the edges. The resistive loading reduced the oscillations and forced the currents to zero at the edges.



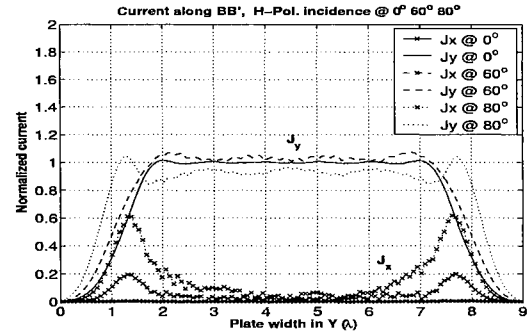
(a) Current along AA', Vertical polarized incidence



(b) Current along AA', Horizontal polarized incidence

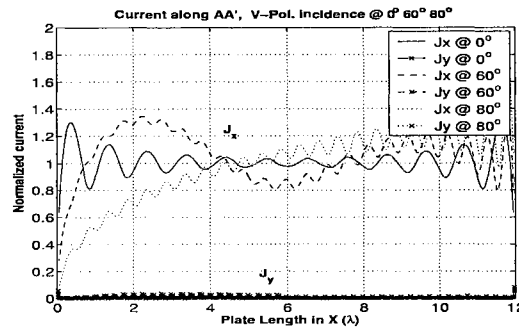


(c) Current along BB', Vertical polarized incidence

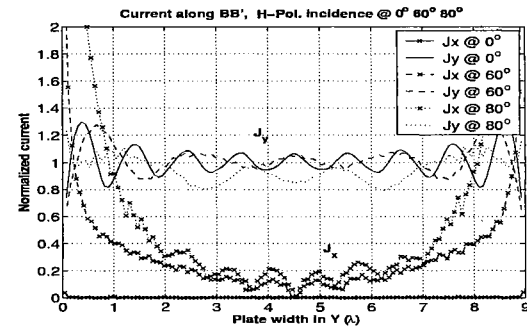


(d) Current along BB', Horizontal polarized incidence

Figure 4.14: Current distribution on the flat impedance plate with resistive edge loading



(a) Current along AA', Vertical polarized incidence



(b) Current along BB', Horizontal polarized incidence

Figure 4.15: Current distribution on the flat impedance plate with no resistive edge loading.

### • On-axis Backscattering

Incidence angles ( $\theta_i$ ) are usually divided into three ranges, small incidence ( $\theta_i = 0^\circ$  to  $30^\circ$ ), moderate incidence ( $\theta_i = 30^\circ$  to  $60^\circ$ ), and grazing incidence ( $\theta_i = 60^\circ$  to  $90^\circ$ ). Figure 4.16 shows the on-axis backscattering cross-section for  $\theta_i$  ranging from  $0^\circ$  to  $90^\circ$ . Part(a) used a sea surface impedance plate, while part(b) used a PEC surface. VV indicates that both the transmit and receive polarizations are vertical, while HH shows the horizontal polarization transmit/receive. VH and HV represent the cross-polarizations. At small incidence case, co-polarization backscatter is much stronger than cross-polarization, typically 50 dB or more. The ratio of VV/HH is 0 dB, which the physical optics model (PO) predicts [142]. At normal incidence ( $\theta_i = 0^\circ$ ) the reflection is specular, so PO is accurate. The sea water specular reflection is 2 dB below that with the PEC plate. Away from normal incidence the scattering is due to edge diffraction that is not fully suppressed by the edge loading. Interference lobing appears in the backscattering away from normal due to diffraction from the opposite edges. As shown by Zhao and West [72], the interference lobes are considerably larger when no edge loading is used. When the induced edge currents are attenuated by the resistive loading, the RCS declines quickly as the incident angle increases from  $0^\circ$  to  $90^\circ$ . Note that the results below about  $-80 \text{ dB} \cdot \lambda^2$  are affected by the numerical noise

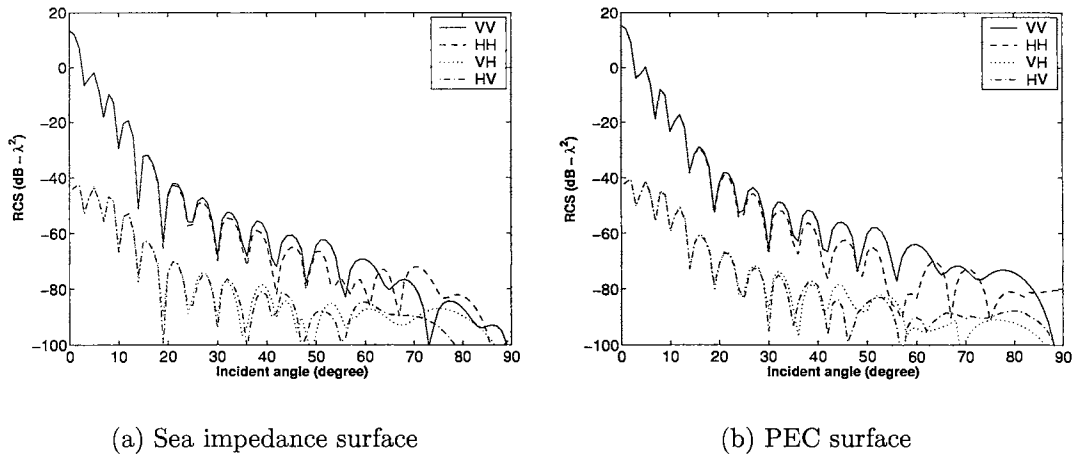


Figure 4.16: RCS of normal backscattering from the flat plate.

floor of the calculations.

- **Off-axis Backscattering**

The 3-D “off-axis” backscattering RCS distribution figures are shown in Figure 4.17. The backscattering ranges from  $\phi = -30^\circ$  to  $30^\circ$  (azimuthal angle  $\pm 30^\circ$  off the -x axis). The results are similar to that of the on-axis backscattering in Figure 4.16. First, co-polarization scattering (VV,HH) is much stronger (about 50 dB) than cross-polarization scatter (VH,HV) at small incidence angles. Also, the scattering declines quickly as the incidence angle increases, from about 20 dB to -100 dB for co-polarization and -30 dB to -100 dB for cross-polarization as the incidence angle changes from  $0^\circ$  to  $90^\circ$ . Edge diffraction again causes interference lobing as

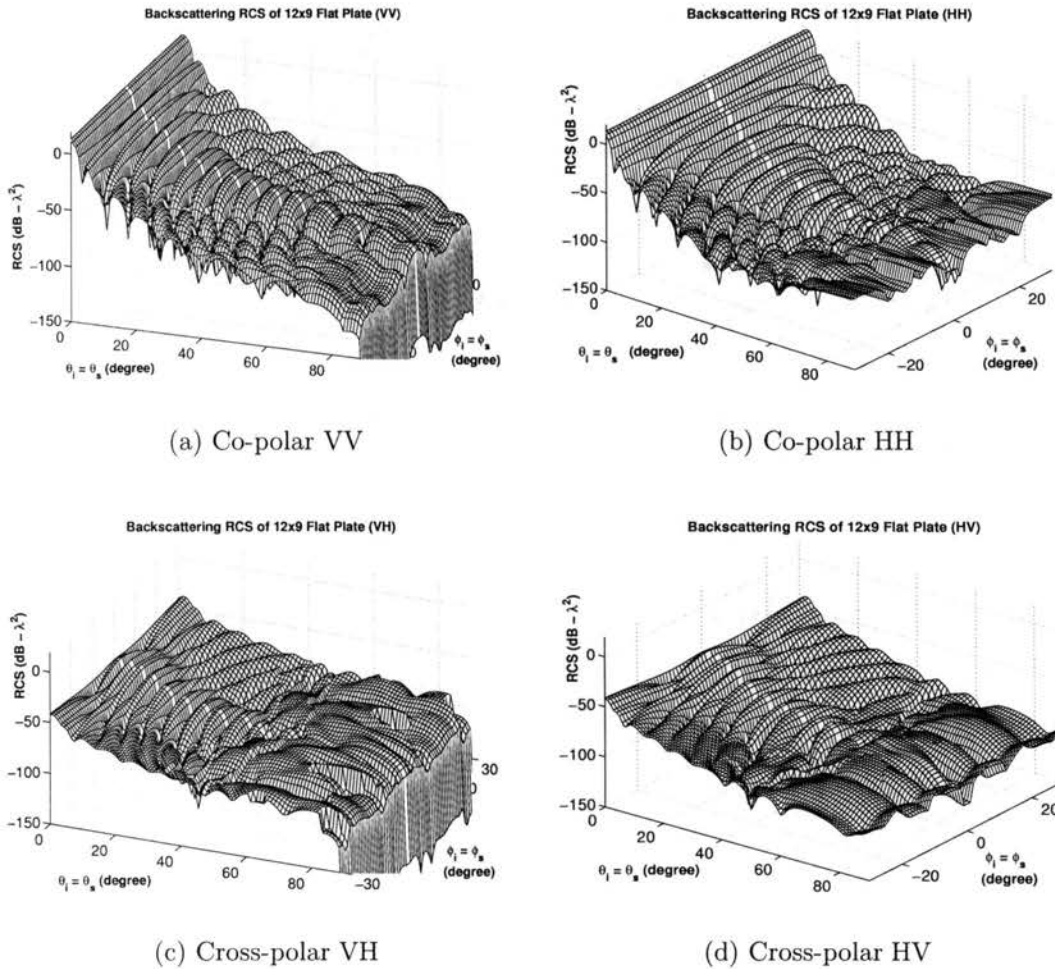


Figure 4.17: Off-axis backscattering RCS distribution.

the incident angle ( $\theta_i$ ) changes. The fluctuations in the azimuthal dimension are also caused by the edge diffraction when the incidence is azimuthally varied. The RCS distributions of cross-polarized backscattering at VH and HV nearly equal above -80 dB- $\lambda^2$  (the numerical noise floor), which agrees with the reciprocity principle.

### • Bistatic Scattering

The bistatic scattering from the flat plate with fixed illumination at  $\phi_i = 0^\circ$  and  $\theta_i = 80^\circ$  is now considered. The results with the observation angles ranging over  $\phi_s = 0^\circ$  to  $360^\circ$  and  $\theta_s = 0^\circ$  to  $90^\circ$  is shown in Figure 4.18. Figure 4.19 also shows the results as a contour plot.

The bistatic scattering distribution in Figure 4.18 is similar to the “off-axis”

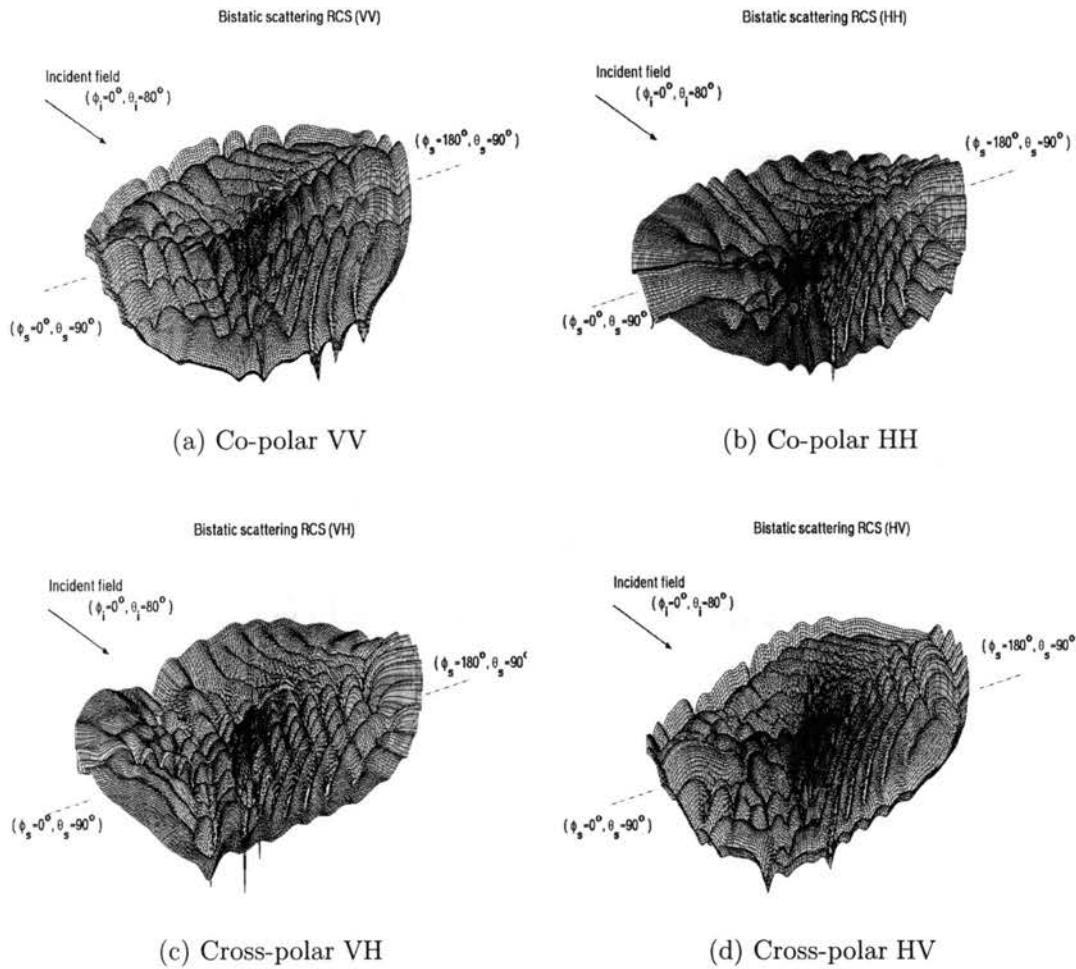


Figure 4.18: Bistatic scattering RCS distribution of the flat plate.

backscattering in Figure 4.17. The interference lobing with incident angle and fluctuation in azimuthal dimension still exist due to the edge diffraction, and the diffraction effects change as the observation azimuthally varies. Overall, the lobing in the bistatic scattering changes more slowly than that with backscattering since the induced current distribution remains unchanged here. The associated magnitude contours in Figure 4.19 indicate that the cross-polarization scattering is still much lower than the co-polarization scattering. The maximum scattering for both co-polarization and cross-polarization cases appears around the observation point  $\phi_s = 180^\circ$ ,  $\theta_s = 80^\circ$ , which corresponding to the specular reflection direction for this incidence. However, due to the lobing, the maximum scattering values do not exactly appear in the specular-reflection direction.

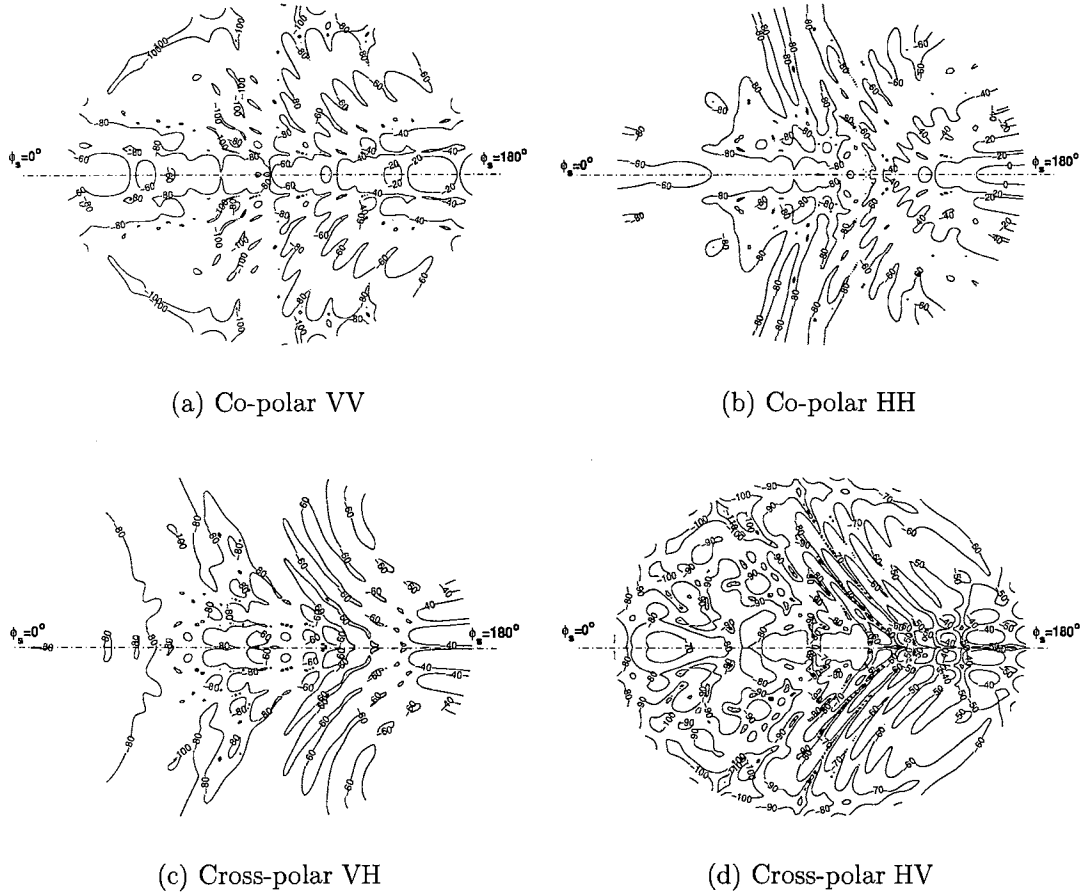


Figure 4.19: Contours of the bistatic scattering RCS of the flat plate.

# Chapter 5

## Normal Backscattering Study

In the last two decades, LGA breaking wave scattering has received considerable attention in surface scattering research. The breaking wave surfaces have steepening wave fronts, projected wave crests, and overturning jets. The projected and steep sections of a surface cause strong reflection at LGA incidence, thus potentially dominating the scattering from the entire surface. Therefore, the understanding of scattering from various crest shapes is critical to the understanding of the overall sea-surface scattering.

In Chapter 4, the MM-based numerical techniques were reviewed, and the validity of the MLFMA routine was verified by analyzing the scattering from a flat plate. These numerical routines are now applied to 3-D breaking-wave crest models. Directly measured surfaces typically have multiple scattering features whose contributions are difficult to isolate when the entire surface is modeled. Therefore, the test surfaces are formulated to have a single dominant scattering feature which may be examined in isolation. The effects of the individual features may then be combined to give the complete scattering.

As introduced in Section 2.2, the 18 profiles of LONGTANK model case 2.4 [63] describe the time-evolution of a breaking wave. The crest shapes of the profiles are typical of the crest features of breaking waves. Therefore, 3-D test surfaces are created



from these 18 profiles. As a reference, the 2-D scattering of the individual profiles are completed first using MM/GTD and EGO/GTD. The scattering for the 3-D test surfaces is then computed by using MLFMA. The validity of 3-D EGO model is also discussed based on the comparison of the analytical and numerical results.

In this chapter, only upwave-looking backscattering is discussed (analogous to the on-axis look with the flat plate in the previous chapter). Results presented are limited to  $60^\circ$  to  $90^\circ$  incidence since the LGA backscattering only is of interest. The frequency of the incident wave is assumed 10 GHz unless specially noted.

## 5.1 Generation of 3-D Crest Test Surfaces

As mentioned, the 18 profiles of the LONGTANK model case 2.4 indicate the temporal evolution of a complete breaking wave. Each profile ideally represents a specific crest shape during the formation of a breaking wave. Figure 2.3 shows that profile 1 to profile 11 are the steepening waves which represent a energy cumulative process [143]. An overturning jet forms gradually from profile 12 to 18. Compared with a flat or smooth surface, the steepening and the overturning jet will lead to strong backscattering when the incident field illuminates it at low grazing angles. On the other hand, the wave breaks as the overturning jet gets so large that the capillary and hydrodynamic forces can not support the weight of the projected water. After the crest collapses, turbulent regions are generated, which reflect or scatter the incident energy into different directions. The backscattering therefore reduces significantly, and it is the crest that dominates the backscattering from a breaking wave at LGA incidence. The calculation of the scattering from individual profiles of the LONGTANK series is a 2-D electromagnetic problem. The hybrid MM/GTD technique is therefore employed to numerically solve the 2-D scattering problem. In order to apply MM/GTD routines, the original profiles are pre-processed by symmetric reversal, and a  $3^\circ$  clockwise rotation. The rotation is used for convenience in implementing the

half-planar extension required by MM/GTD. Also, the relative positions of the profiles also are adjusted, which actually does not affect the magnitude of the scattering from each profile, but will be convenient for the later 3-D test surface generation. Figure 5.1 shows the pre-processed profiles 1 to 18. Each has  $3\lambda$  half-planar extensions at each side with a  $40^\circ$  slope angle to horizontal.

The 3-D test surfaces are generated by using a spline interpolation based on the profiles of LONGTANK model case 2.4. The adjusted and extended profiles in Figure 5.1 are used. One profile is used as the major reference for each 3-D test surface. The other profiles before it are used in the interpolation, and those after it are ignored. For example, in the generation of test surface 12, the spline interpolation is applied from profiles 1 through 12 only. Figure 5.2 shows the generation of surface 12. The original profiles (plotted with thick lines) are separated azimuthally, between which the interpolation generates new profiles and fills the space. The interpolation between profile 11 to 12 dominates the surface, and the interpolation between profiles 1 through 11 only smoothly transitions to the edge extension.

Resistive loading as discussed in Section 4.8 is used to suppress edge-diffraction effects. The  $3\lambda$  flat extensions in front of and in back of the individual LONGTANK profiles provide the low-scattering regions needed for the application of the loading

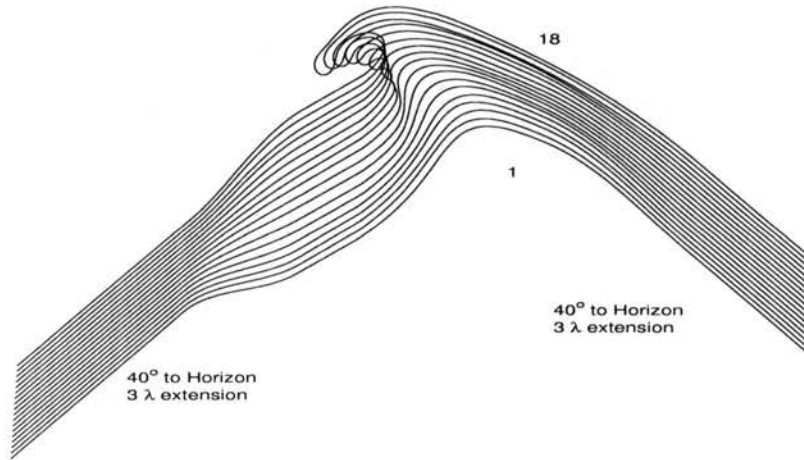


Figure 5.1: Pre-processed LONGTANK case 2.4 profiles.

in the range (x) direction. The surface must also be extended in the azimuthal (y) direction. Profile 1 of the LONGTANK series is sufficiently steep that it gives significant 2-D backscattering at  $60^\circ$  incidence. It therefore should not be extended directly. Instead, multiple passes of a three-point moving average were applied to profile 1 to decrease the steepness and give a surface with little backscattering at all incidence. This resulting surface was applied over  $2\lambda$  to provide the region for the resistive loading. Also, the surface was made symmetric in azimuth around the reference profile. The smoothed profile 1 extension therefore appears on both sides of the test profiles, on which the loading is applied. The process for resistive loading is also illustrated in Figure 5.2. Note that the symmetric duplication may lead to strong interference for some surfaces. This phenomenon will be identified when it occurs.

Profiles 8, 12, and 18 represent the steepening stage, the beginning of overturning, and the fully developed overturning jet, respectively. They are therefore chosen as reference profiles. An earlier 2-D scattering analysis [2] showed that the scattering was very sensitive to the profile change at the initial breaking (from profile 11 to 13), particularly at VV. Therefore, profiles 11 and 13 were also used to generate two additional test surfaces. Finally, profile 15 is used as the representative of a small overturning jet. Therefore, a total of six test surfaces are used with profiles 8, 11,

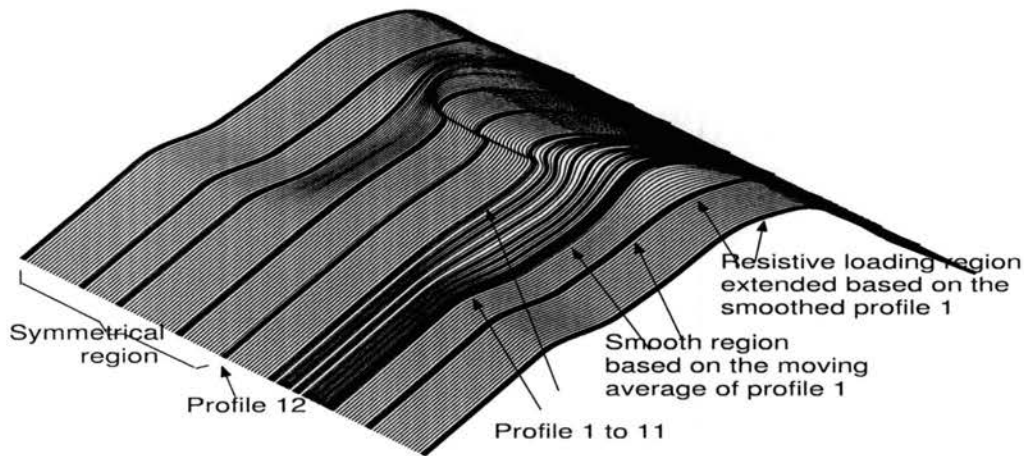


Figure 5.2: Demonstration of the 3-D crest surface formation.

12, 13, 15 and 18 used as the references. The final 3-D test surfaces are shown in Figure 5.3, they are named surface 8, 11, 12, 13, 15 and 18, respectively.

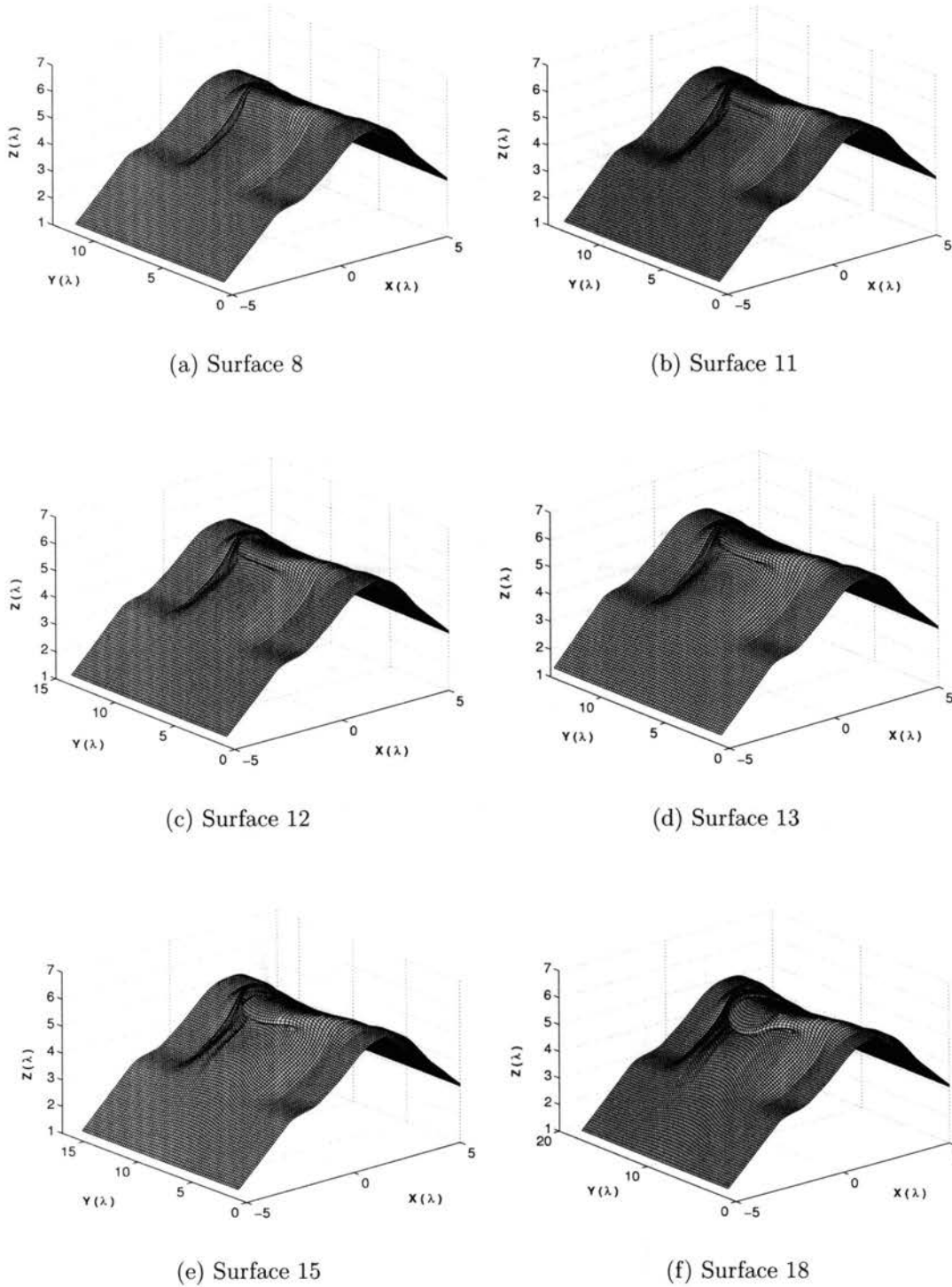


Figure 5.3: Test 3-D surfaces with various crest features

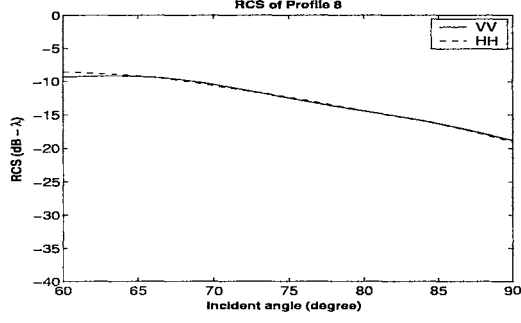
The six surfaces have different features at their centers, which represent the different crest characteristics at different stages of breaking. These features may exist in the different stages of a breaking wave, or simultaneously appear in different parts of a large sea surface.

## 5.2 2-D Scattering

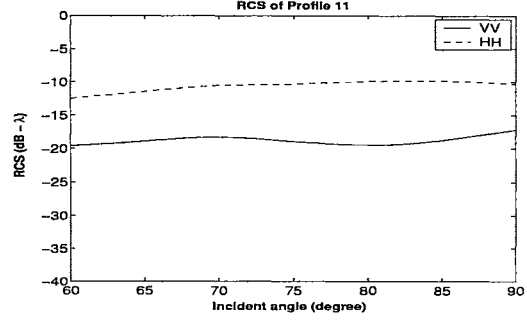
### 5.2.1 MM/GTD

MM/GTD was previously used by West [2] to find the upwave looking backscattering from the 2-D profiles in Figure 5.1. Additional results from profiles 8,11,12,13,15 and 18 are shown in Figure 5.4. Shown are the LGA radar cross-sections (RCS) for both VV and HH backscattering. The 2-D RCSs are calculated from the definition in (2.1), and are given in dB with respect to unit wavelength (dB- $\lambda$ ). The VV and HH RCS scattering of profile 8 are nearly identical at all angles. However, HH exceeds VV from profile 11 to profile 13. The HH RCS depends much less strongly than VV on incidence angles with these profiles. A deep null appears in the VV RCS at  $77^\circ$  with profile 13. Note that HH exceeding VV backscatter indicates a super event. For profile 15, with a small jet, the super event occurs only when the incident angle is greater than  $70^\circ$ . As the jet becomes larger in profile 18, the super event exists for all incident angles from  $60^\circ$  to  $90^\circ$ .

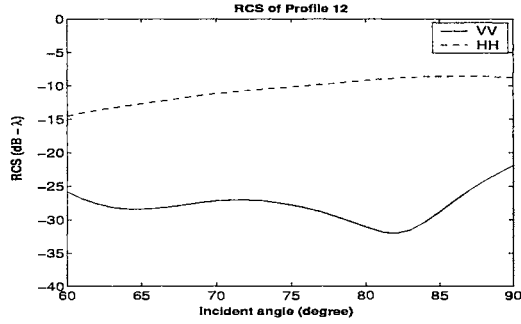
Figure 5.5 shows the backscattering RCS of the 18 profiles at incidence angles of  $80^\circ$  and  $60^\circ$ . The scattering dramatically changes with the incident angle change. At  $80^\circ$  incidence, the super event exists after profile 8, but at  $60^\circ$  incidence the situation is more complicated. At  $60^\circ$  incidence, the super event appears after profile 8, but disappears from profile 13 through 17. The explanation of the  $80^\circ$  RCS was provided by West[2].



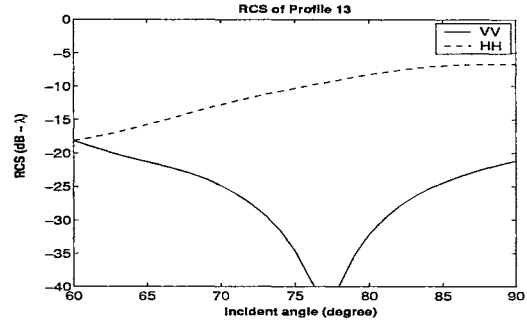
(a) Profile 8



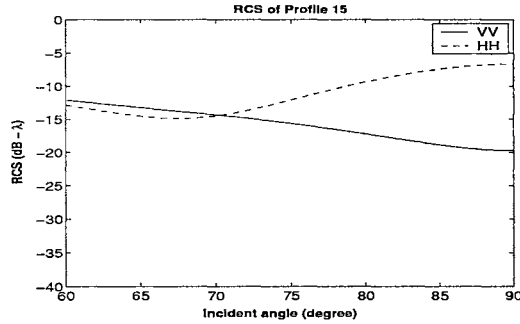
(b) Profile 11



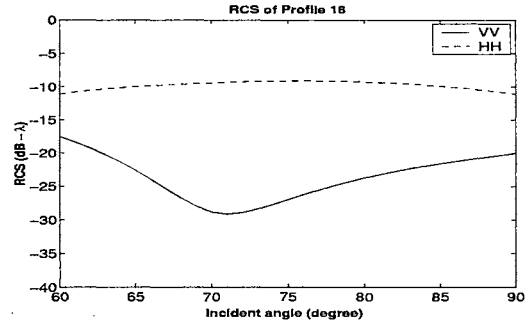
(c) Profile 12



(d) Profile 13



(e) Profile 15



(f) Profile 18

Figure 5.4: Backscattering RCS of 2-D surfaces (MM/GTD)

### 5.2.2 Prediction of EGO/GTD model

The EGO/GTD model [2] can provide a good prediction of the backscattering from some simple crest structures. For the crest geometry shown in Figure 5.6, there are two specular reflection points A and B located on the jet and cavity region respec-

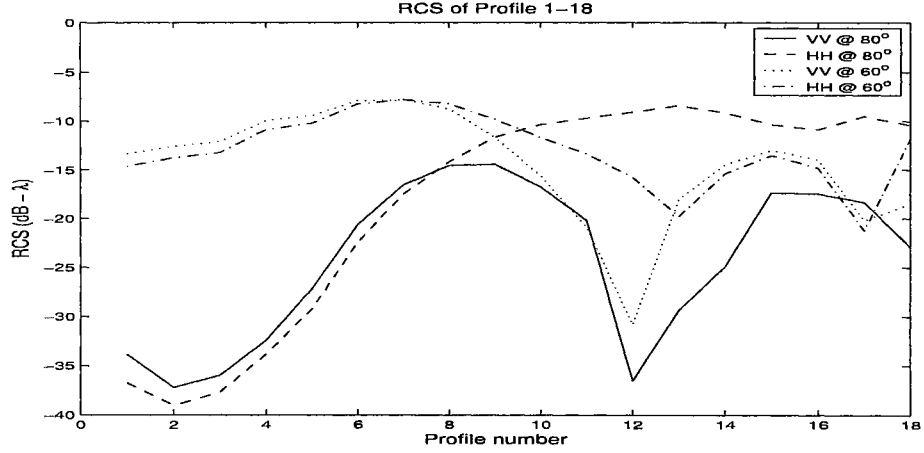


Figure 5.5: Backscattering of the 18 LONGTANK profiles (MM/GTD) [2].

tively. D shows a curvature inflection point. The backscattering from this crest can be predicted by the EGO reflections from A and B plus the GTD-based diffraction from D. Interference may occur between the reflections from A and B, explaining why the VV backscattering of profile 13 has a deep null. However, if the crest structure is too complicated, the EGO/GTD model may fail to give a good prediction.

According to West's analysis [2], prior to profile 9 there are no specular reflection points on the waves at very low grazing angle. The backscattering of profile 8 is therefore dominated by the GTD-based diffraction from the inflection point. At profile 9 and beyond specular reflection points appear and the EGO back-reflection must also be included.

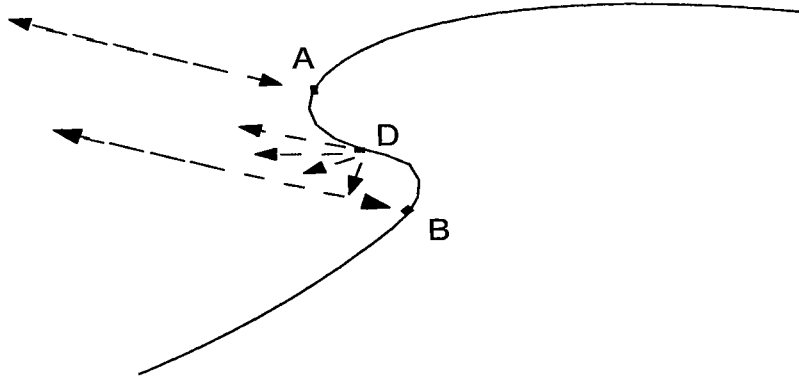


Figure 5.6: Geometry for reflection and diffraction by a crest structure.

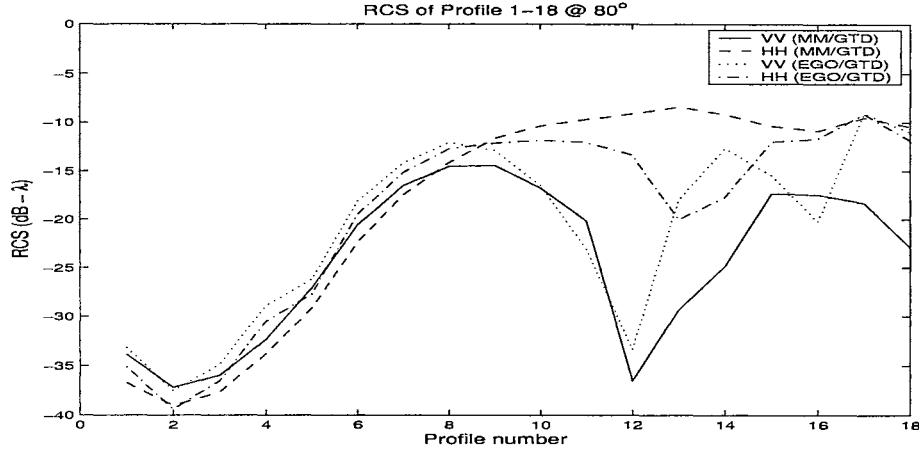


Figure 5.7: EGO/GTD prediction of the backscattering from the 18 LONGTANK profiles (repeated from [2]).

Figure 5.7 shows the EGO/GTD backscattering prediction result of the 18 profiles when incident angle is  $80^\circ$ . Compared with the MM/GTD numerical result, EGO/GTD is accurate to within 3 dB at both polarization up to profile 9. In particular, the VV interference nulls of profile 10 through 12 are predicted. The modeled result is quite inaccurate at both VV and HH for profiles 13 and later.

## 5.3 3-D Crest Test Surface Scattering

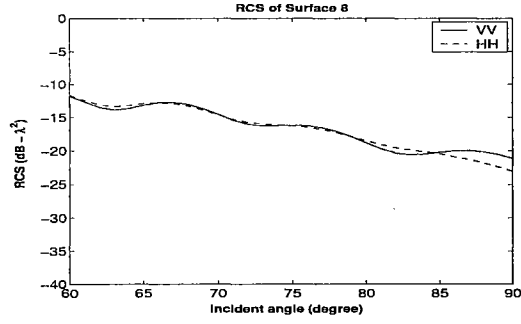
### 5.3.1 Backscattering

MLFMA is now used to analyze the backscattering from the six 3-D crest test surfaces. As a full vector technique, MLFMA can find both the co-polarized and cross-polarized backscattering. The 3-D RCS is obtained following the definition of (2.2), represented using dB with respect to the unit wavelength square ( $\text{dB-}\lambda^2$ ). Figure 5.8 shows the co-polarization backscattering RCS when looking up-wave at LGA. The depolarization phenomena will be discussed in next chapter.

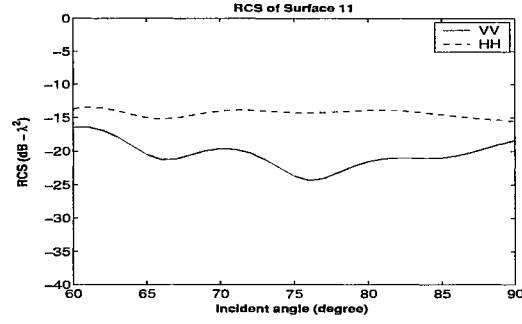
Many similarities are apparent when comparing the backscattering RCS of these 3-D test surfaces with the MM/ GTD results associated with individual 2-D profiles



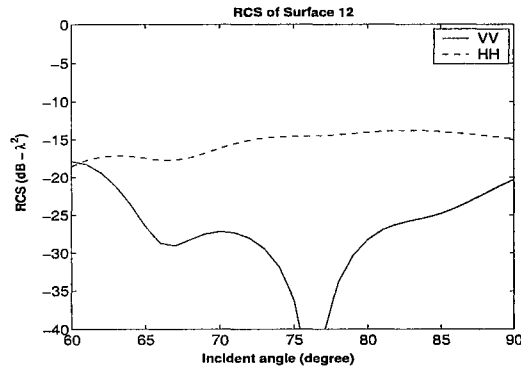
in Figure 5.4. The dependence of the RCS of surface 8 and 11 on incidence angle are similar to those of 2-D profiles 8 and 11. The relative RCS at VV of 3-D surface 12 and 13 are higher than those of 2-D profiles 12 and 13 when incidence at  $60^\circ$  to  $65^\circ$ ,



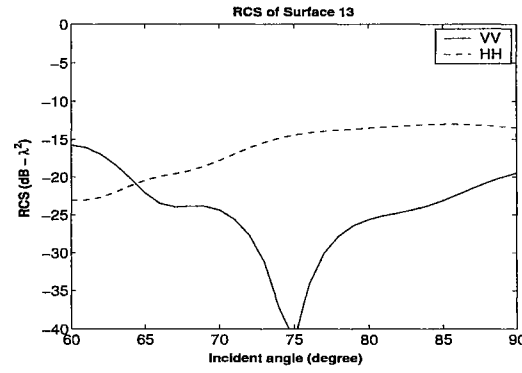
(a) Surface 8



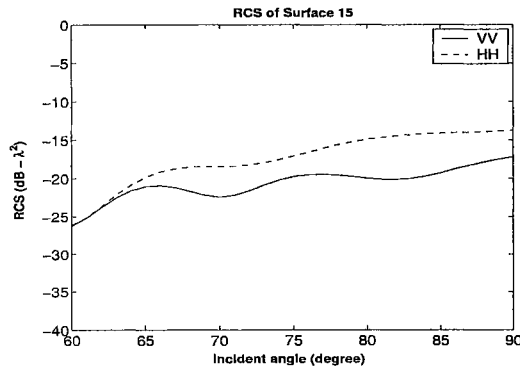
(b) Surface 11



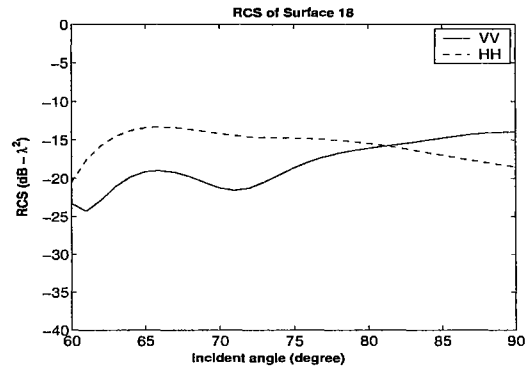
(c) Surface 12



(d) Surface 13



(e) Surface 15



(f) Surface 18

Figure 5.8: Normal backscattering RCS of 3-D test surfaces (MLFMA)

so the super events disappear in these cases. A deeper interference null appears with 3-D surface 12 VV scattering than in the corresponding 2-D case. 3-D surfaces 15 and 18 and 2-D profiles 15 and 18 backscattering differs significantly at both VV and HH. This results because the 2-D surfaces are electromagnetically treated as if they extend infinitely in azimuth. The 3-D surfaces are curved in the azimuthal dimension, affecting the scattering.

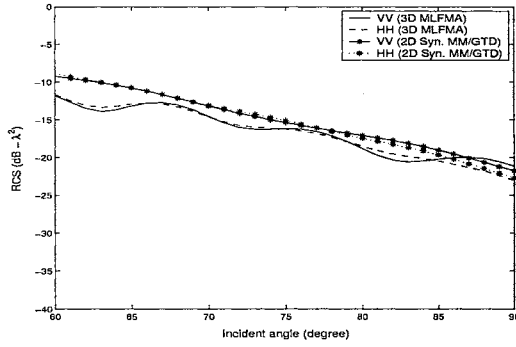
### 5.3.2 The Relationship of 2-D and 3-D Backscattering

Since the 3-D test surfaces were formed by azimuthally aligning and interpolating the 2-D crest profiles, the scattered field from a 3-D test surface can be approximated from the 2-D scattering from the individual profiles using a technique first used by Zhao [67] for a spilling breaker wave. The approximate 3-D field is given [77] by

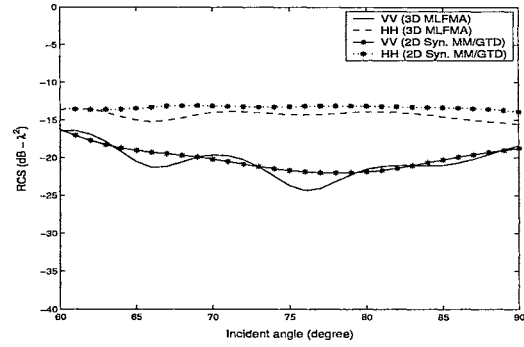
$$E_{3D} \approx \left( E_{2D-total} \frac{le^{j\pi/4}}{\sqrt{\lambda\rho}} \right)_{\rho=r}, \quad (5.1)$$

where  $E_{2D-total} = \sum E_i$  is the coherent sum of all 2-D surface scattered fields,  $E_i$  is the scattered field of the  $i$ th 2-D profile, and  $l$  is the azimuthal width of each 2-D profile used in forming the 3-D surface. MM/GTD is used to compute the backscattered fields from each 2-D profile of a test surface, and (5.1) is applied to these fields to give the 3-D synthesized fields. The 3-D RCS is then found from (2.2). The azimuthal width is the interval between two 2-D profiles in the 3-D test surface after interpolation ( $l = \frac{1}{60}\lambda$  here). Figure 5.9 shows the comparison of the 2-D-synthesized RCS with the reference MLFMA results. The starred lines are the synthesized results. The synthesized HH RCS gives a better match with the exact results than at VV, especially at higher incidence ( $> 70^\circ$ ). When incident angle is less than  $70^\circ$ , the maximum error of HH is less than 5 dB (except surface 15). The synthesized VV shows the interference nulls with profiles 12 and 13. However, VV is sensitive to the azimuthal curvature of reflection points, leading to oscillations in the MLFMA results

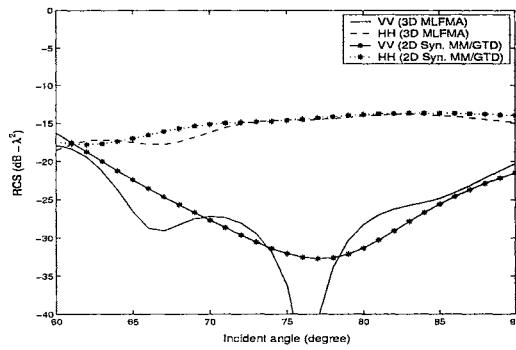
that are not seen in the synthesized results. Overall, the disagreement becomes larger as the surface jet gets bigger. Siegel [144] introduced a shape correction factor for the RCS calculation of simple bodies of revolution. The 3-D RCS was obtained from the relative 2-D RCS by multiplying the shape correction factor to account for the



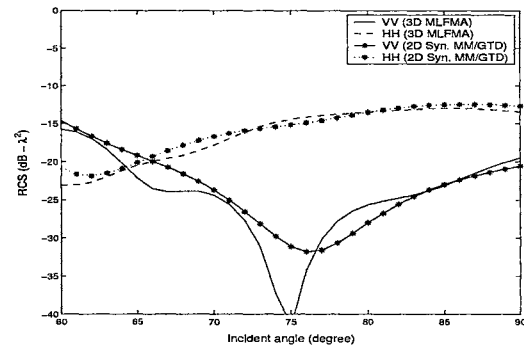
(a) Surface 8



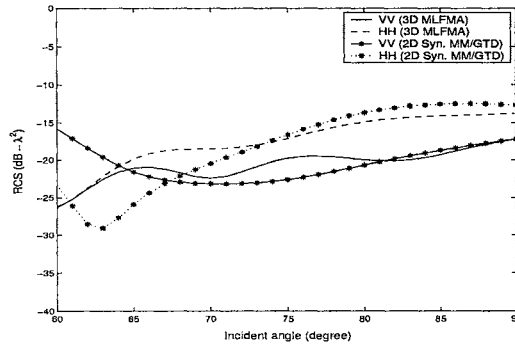
(b) Surface 11



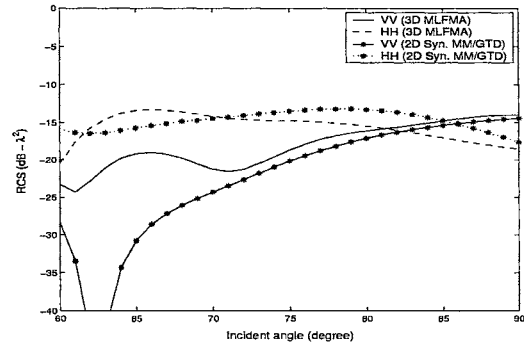
(c) Surface 12



(d) Surface 13



(e) Surface 15



(f) Surface 18

Figure 5.9: Comparison of synthesized 3-D RCS with MLFMA results.

curvature. However, different correction factors were used according to the shape of the scatterers. Similarly, the approximation in the relationship (5.1) also relates to the shape of a scatterer. The crest shape changes rapidly in azimuth with surface 18, which compromises the approximation accuracy of (5.1).

### 5.3.3 3-D EGO Model

Referring back to the crest test surfaces in Figure 5.3, the surfaces are smoothly curved in azimuth at their center. Sharply curved sections occur only on the sides, which should have only a slight role in the upwave-looking backscattering. In the range dimension, the angled edge extensions are shadowed from the crest so there is no multipath reflection. Similar to the 2-D profiles, the upwave looking backscattering from these surfaces should be primarily due to a few quasi-specular reflection points. Thus, a 3-D EGO model will be applied to the 3-D crest test surfaces. Diffraction from inflection points will be small and very difficult to model with 3-D profiles, so is simply ignored. Also, EGO failed after 2-D profile 13, so is not expected to be valid for the 3-D profiles after 13. The 3-D EGO model was therefore applied only to test surface 12 and 13.

To apply the 3-D EGO approximation, an automatic searching code was first developed to find the reflection points on the surface by comparing the incident direction with the surface normal vector at every point on the surface. The point is assumed to contribute to the specular reflection when the error angle between these two directions is less than a specific criteria  $\delta$ . The reflection point distribution of surface 12 and surface 13 are shown in Figure 5.10 when  $\delta \leq 2^\circ$ . The position accuracy of the reflection points depends on the search sampling accuracy. The range dimension step size of  $\Delta x = 0.05 \lambda$  and the azimuthal step size of  $\Delta y = 0.02 \lambda$  are used in Figure 5.10. The figures indicate that all reflection points concentrated in two locations for any incident angle from  $60^\circ$  to  $90^\circ$ . One area is at a convex curvature point in the range

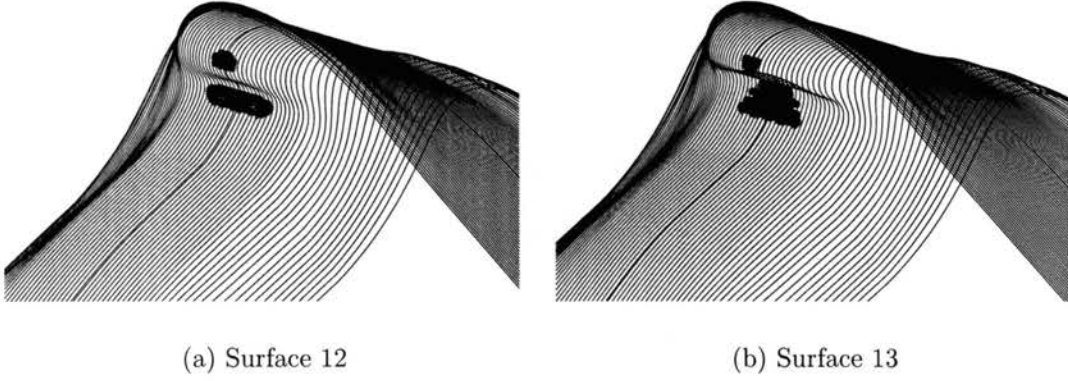


Figure 5.10: Automatically searched reflection points when  $\delta \leq 2^\circ$ .

dimension on the jet. The other is located in the cavity region under the jet, where the range curvature is concave.

Two equivalent reflection points are obtained from the mean of the reflection point coordinates automatically identified, shown in Figure 5.11. The 3-D EGO model is implemented at these two points. The RCS results of the VV and HH reflection are calculated and compared with the reference of MLFMA results in Figure 5.12. The 3-D EGO results using the automatically found reflection points and curvatures (denoted as “Auto. 3D-EGO” in the figure) give fairly poor agreement with the MLFMA results. However, the positions of the two reflection points on surface 12 were slightly adjusted manually, giving the EGO results in Figure 5.12 designated

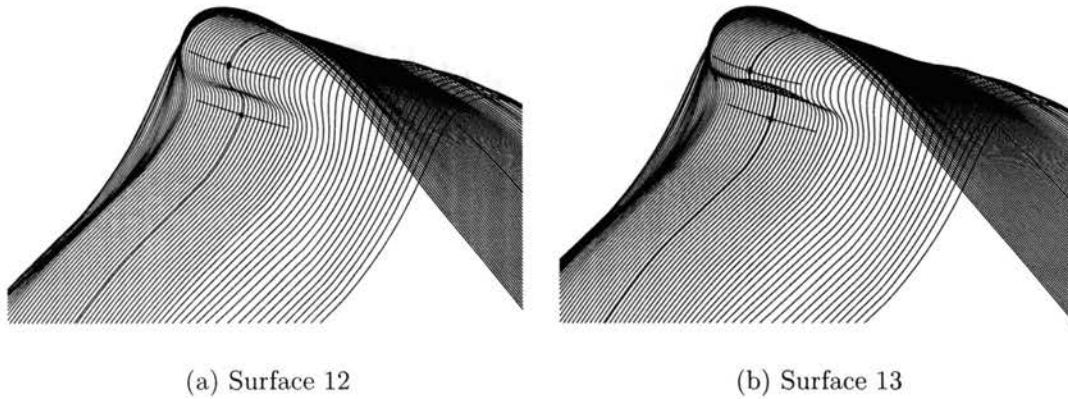
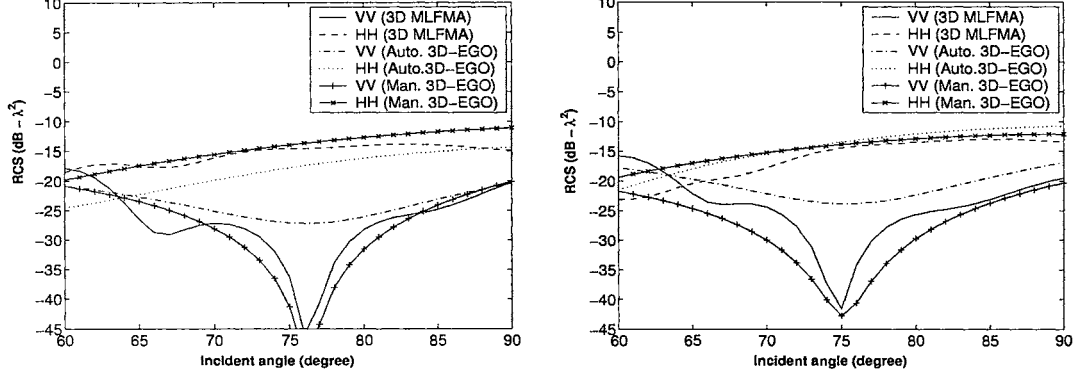


Figure 5.11: Equivalent reflection points and their cross-section curves.



(a) RCS of surface 12

(b) RCS of surface 13

Figure 5.12: Comparison the 3-D EGO results with the reference of MLFMA.

by the crossed and plussed lines. The VV RCS changes dramatically, and a deep interference null appears at the same incident angle as the reference results. This result indicates that 3-D EGO is able to reveal the underlying mechanisms that lead to backscattering as the incident angle changes. On the other hand, the sensitivity to the positions of the reflection points and still limited accuracy indicate that the two-point reflection model is not sufficient to provide a good prediction of the backscattering from the entire surface. This likely results since the inflection point diffraction and the reflection from side regions are completely ignored. Note that similar results for surface 13 are also obtained by slightly adjusting the positions of the two reflection points, as seen in Figure 5.12(b).

### 5.3.4 Cross-section Curvature Effect on Scattering

The computed test-surface backscattering presented so far shows that the azimuthal curvature of a surface plays a role in its scattering. Equations (3.12) and (3.13) also indicate the relationship between the scattered field and the radii of curvature at the reflection point. The relationship can also be explicitly observed through numerical simulation. Surface 12 is used as an example. The surface is reformed by reducing spacing between the individual 2-D profiles used to form the 3-D surface by a specific

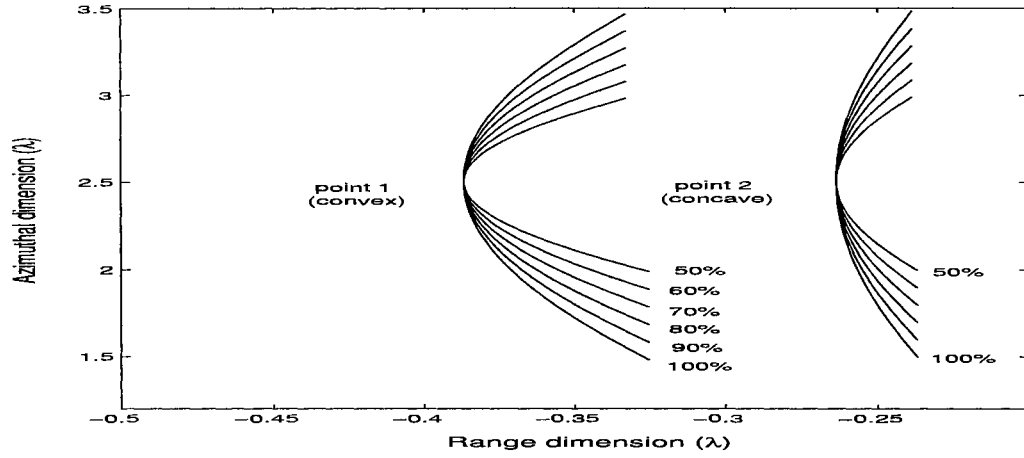


Figure 5.13: The cross-section cut lines at reflection points.

percentage. The azimuthal curvature is reduced simultaneously. Figure 5.13 shows azimuthal cuts in horizontal plane through the two reflection points for 50%, 60%, 70%, 80% and 90% compression. The non-compressed cuts is shown in Figure 5.11.

Figure 5.14 shows the VV and HH RCS computed by MLFMA for each compression case. As the azimuthal cross-section radius of curvature decreases, the RCS level decrease for both VV and HH cases. The VV scattering changes sharply as the surface is compressed, and changes the position of the interference null. In fact, equation (3.12) indicates the VV and HH RCS curves should have shifted with a constant level at a specific incident angle if the scatterer is an ideal sphere. For the case of surface

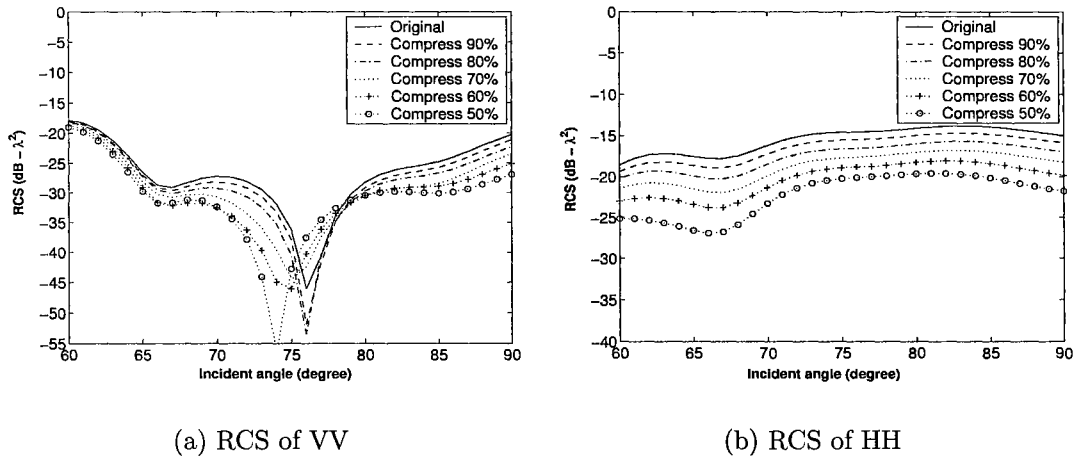


Figure 5.14: The backscattering RCS of compressed surface 12.

12, the null at  $VV$  is generated by the interference between concave and convex points reflections. The surface compression changes the azimuthal curvature at both points differently. The interference therefore changes, and null position is shifted.



# Chapter 6

## Polarimetric Scattering

The vector MLFMA scattering code provides both co-polarized and cross-polarized surface scattering. A full characterization of the polarization dependence of the scattering is termed the polarimetric signature. The polarimetric signature can provide additional information for target identification and classification beyond that available from co-polarized signals alone [145][146]. Polarimetric scattering from the synthesized profiles is considered in this chapter.

The cross-polarized scattered fields were usually very low when looking upwave with the 3-D test surfaces considered in the previous chapter. Here, the dependence of the co-polarization and cross-polarization backscattering on the azimuthal look angle will first be considered. Following the notation in Chapter 4, this is termed “off-axis” backscattering. Then, the incidence elevation and azimuth angles will be fixed and the scattering angles varied, giving the bistatic scattering signature.

In Chapter 4, the flat plate test case was used to define the concepts and terminology for monostatic and bistatic polarimetric scattering. These concepts will be used in examining the polarimetric scattering from the LONGTANK-based 3-D test surfaces. Once again, the study is limited to LGA incidence. The frequency is still assumed to be 10 GHz.

## 6.1 Off-axis Backscattering from Surface 8

The off-axis backscattering RCS for test surface 8 for incidence angles ranging from  $60^\circ$  to  $90^\circ$  and azimuth angles ranging from  $0^\circ$  to  $30^\circ$  is shown in Figure 6.1. Note that the cross-section is symmetric around the  $0^\circ$  azimuthal angle since the test surface is symmetric.

As shown in Figure 6.1 (a) and (b), the RCSs at both VV and HH smoothly reduce as the angle moves azimuthally away from the upwave looking direction. When looking up wave, there are two quasi-specular reflection points in the center of the surface. As marked in Figure 6.2(a), the upper point has convex curvature in range

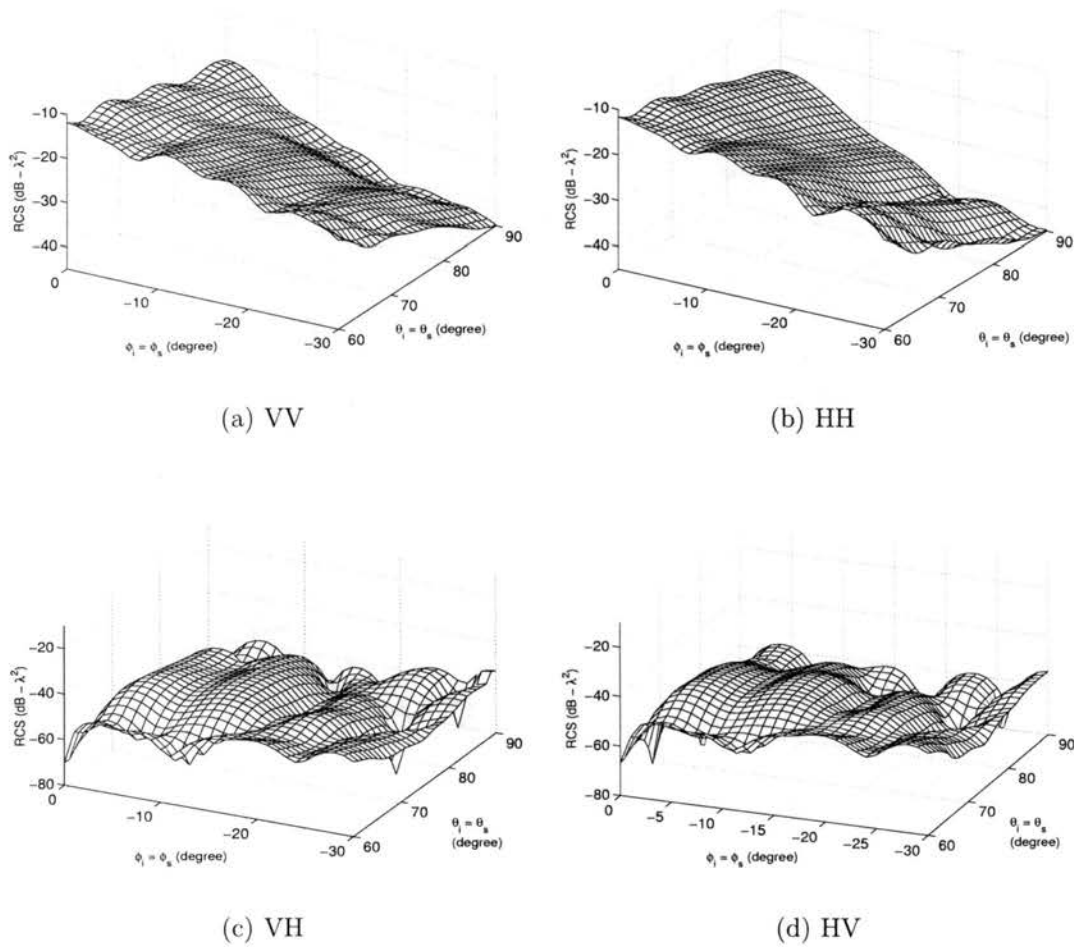


Figure 6.1: RCS of off-axis backscattering from surface 8.

direction and the curvature of the lower one is concave. However, due to the minimal jetting of this surface, these two reflection points closely located, and the range-direction surface radii of curvature are larger than the electromagnetic wavelength. Because of this, no significant destructive interference occurs. As shown in Figure 6.2, the positions of the reflection points move from center across the surface to edge area as azimuthal angle increases. On the other hand, the azimuthal radii of curvature at these specular reflection points reduce gradually, thus causing the RCSs to decrease simultaneously. Both VH and HV cross-sections in Figure 6.1(c) and (d) are very low (below  $-40 \text{ dB-}\lambda^2$ ) and have irregular fluctuations. Although it is difficult to clearly describe the mechanism that leads to fluctuations, the similarity of the RCS at VH and HV indicates the MLFMA computation is accurate.

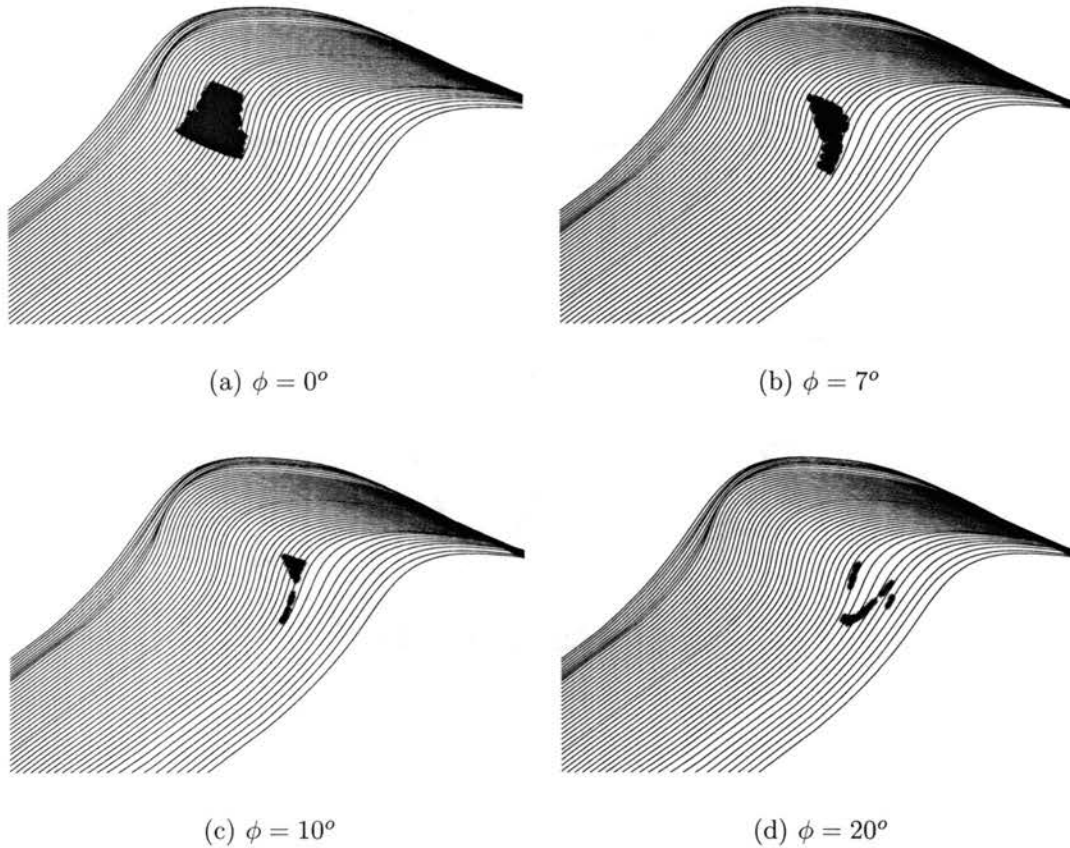


Figure 6.2: Position variation of specular reflection points on surface 8

## 6.2 Off-axis Backscattering from Surface 12

Figure 6.3 shows the off-axis RCS of backscattering from test surface 12. At  $0^\circ$  azimuth, the VV RCS has an interference null at an incidence angle of  $\theta_i = \theta_s = 76^\circ$ , corresponding to part(c) of Figure 5.8. The null position moves toward a larger incidence angle as the azimuth angle increases to  $7^\circ$ . As the azimuth angle continues to increase to  $12^\circ$ , the null position moves back to smaller incidence angles. The VV RCS then smoothly reduces as  $\phi$  moves above  $15^\circ$ . The HH RCS decreases as the azimuth angle increases, with a distinct null appearing at  $9^\circ$  at smaller incidence. In this case, the VH and HV are also very low (below  $-40 \text{ dB-}\lambda^2$ ) and have irregular fluctuations.

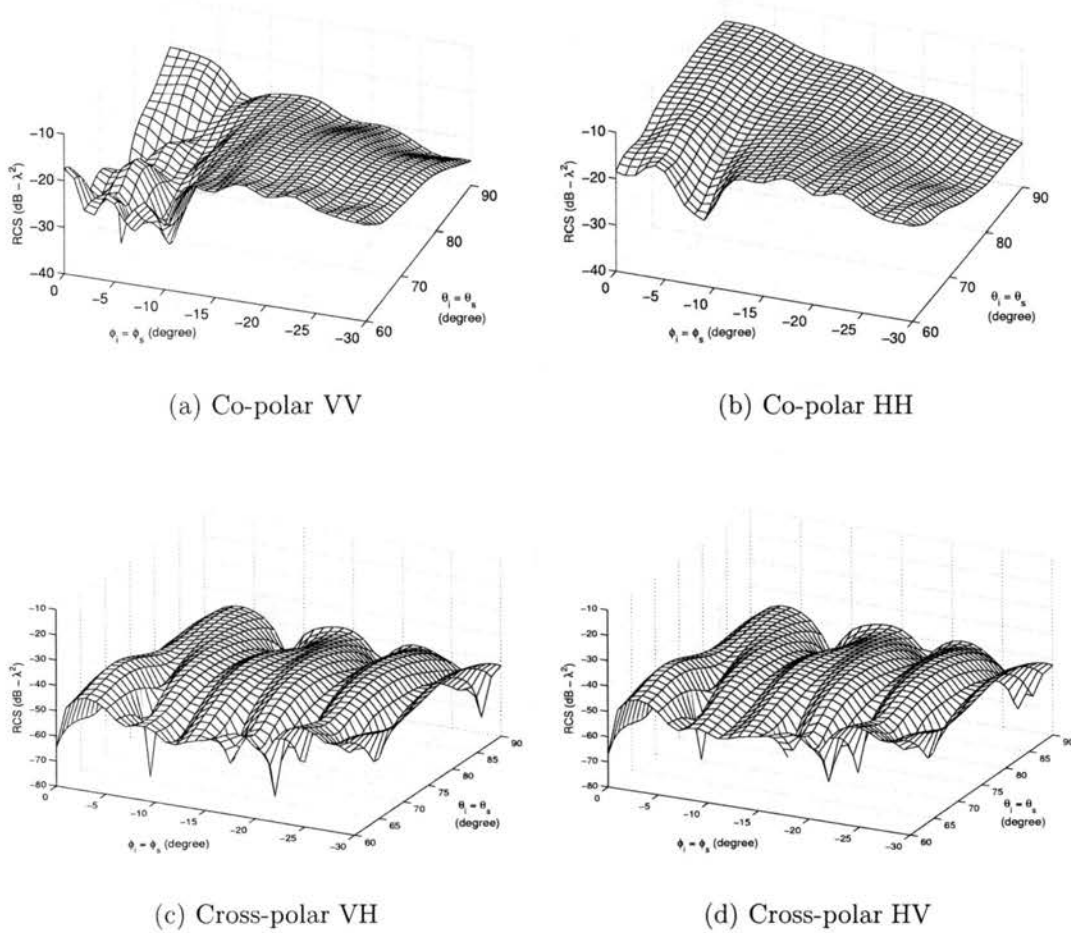


Figure 6.3: RCS of off-axis backscattering from surface 12.

Compared with the cross-polarized scattering from surface 8, the fluctuations are even stronger, which indicates that the scattering mechanisms that lead to interference at co-polarized components also play a role at cross-polarized scattering.

In Section 5.3.3, 3-D EGO showed that the upwave looking (on-axis) backscattering from test surface 12 is dominated by the quasi-specular reflections from the jet

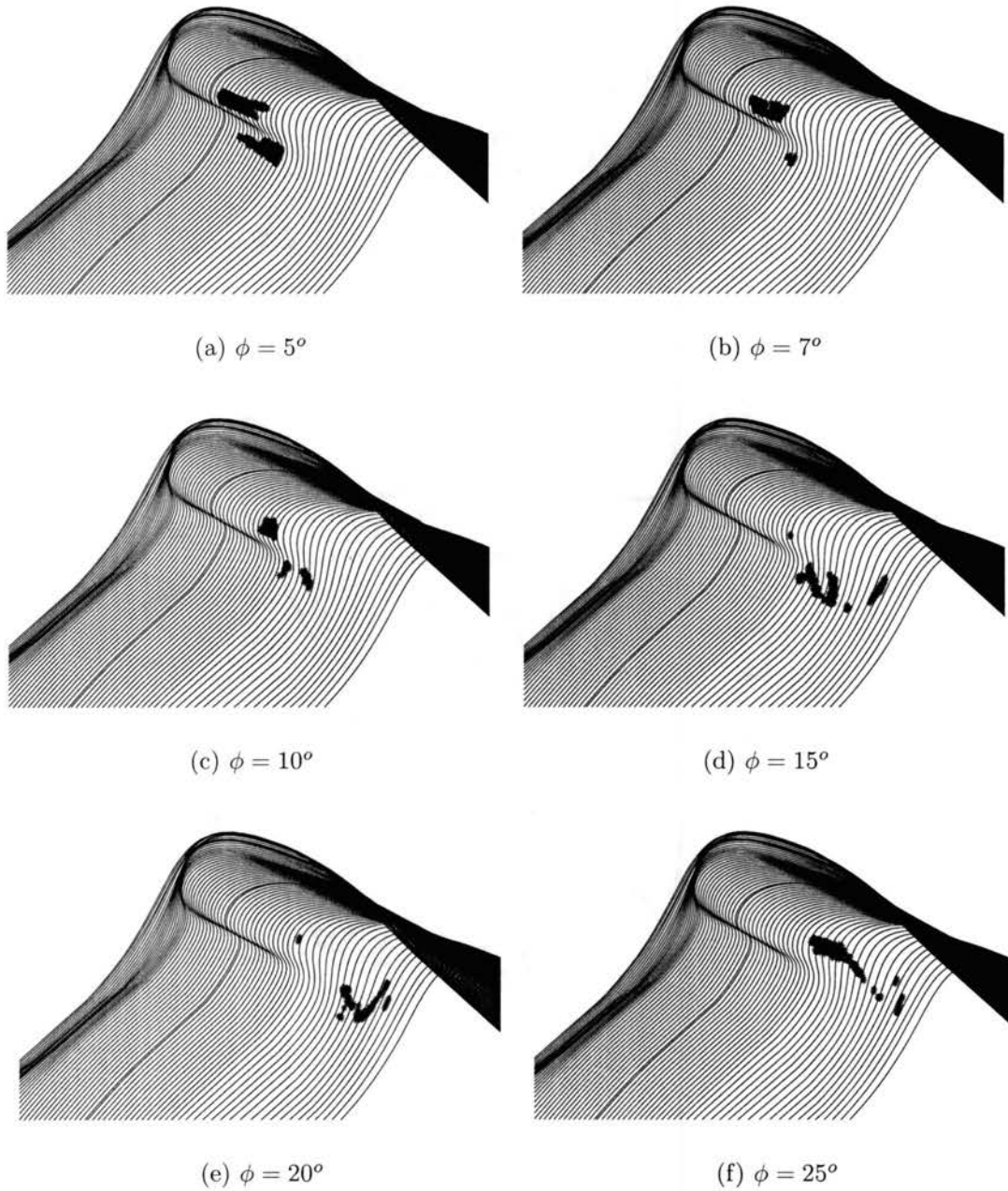


Figure 6.4: Position variation of specular reflection points on surface 12

and cavity regions. Also, interference between these reflections gives cancellation at VV while constructively adding at HH. Thus  $HH > VV$  super events occur.

The off-axis backscattering shows that the destructive interference between the reflections from the jet and cavity region still occurs at VV as the azimuth angle varies. This indicates that specular reflection points still exist and dominate the backscattering. Figure 6.4 shows the specular reflection points identified on surface 12 for a few azimuth angles. The upwave-looking case was shown in part (a) of Figure 5.10. The figure shows that there are specular reflection points on the jet and in the cavity region from  $\phi = 0^\circ$  through  $10^\circ$ , but the positions of reflection points move from the center of the profile to side as  $\phi$  increases. The different curvatures of the surface at the reflection points lead to the change of the depth and incidence angle of the interference null. As shown by West [2], the destructive interference at VV occurs only when convex and concave reflection points exist simultaneously, and the surface radii of curvatures (in range direction) at the reflection points are somewhat smaller than the electromagnetic wavelength. When  $\phi > 10^\circ$ , the reflection points move from the central region to the side section of the surface. Although the convex and concave reflection points are still there, the radius of curvature changes. The interference null at VV therefore disappears gradually.

### 6.3 Off-axis Backscattering from Surface 15

Figure 6.5 shows the off-axis backscattering from surface 15. There is no strong VV interference null around the upwave looking direction corresponding to Figure 5.8(e). However, a null appears as the azimuthal angle increases, and a very deep null appears at all incidence angles above  $75^\circ$  when azimuthal angle is  $7^\circ$ . The specular back-reflection points shown in Figure 6.6 indicate the corresponding scattering mechanism. When upwave looking ( $\phi=0^\circ$ ), the cavity region is shadowed by the jet, so there is no specular reflection from this concave section to interfere with the reflection from the

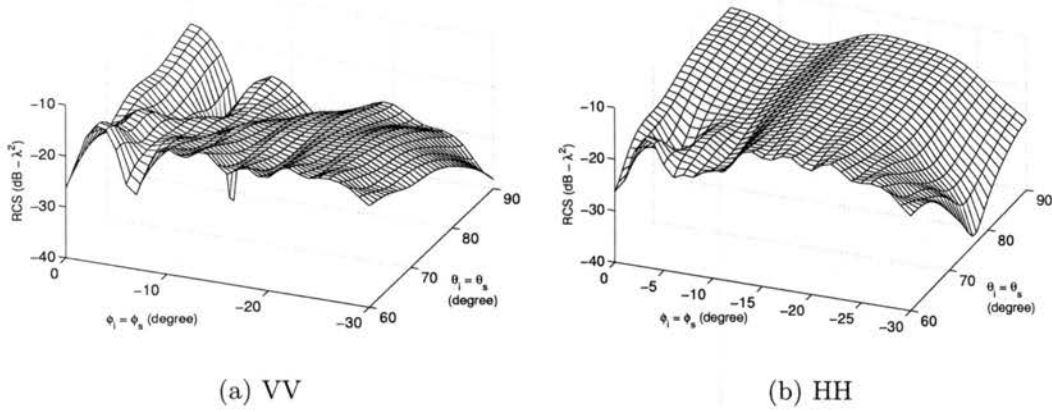


Figure 6.5: RCS of off-axis backscattering from surface 15.

convex jet. As the azimuthal angle increases, the cavity reflection points move out of the jet shadow and become visible. This gives the concave reflection point needed for the VV destructive interference to occur. This effect is most pronounced at the largest incidence angle.

A slight HH null also appears at  $\phi=3^\circ$ . The responsible mechanism will be analyzed in next section.

## 6.4 Off-axis Backscattering from Surface 18

Figure 6.7 shows the off-axis backscattering from surface 18. A deep VV interference null appears at  $\phi = 8^\circ$ . Additional shallow VV nulls exist at other positions. These VV nulls have the same scattering mechanism as that identified in surface 12 and surface 15 cases. That is, the VV nulls are formed by the destructive interference of the reflections from the convex reflection points at jet and the concave reflection points at the cavity region. The HH backscattering includes a deep interference null at about  $13^\circ$  azimuth. No corresponding VV interference null appears at the same azimuth.

As mentioned, a shallow HH null is also observed in the HH backscattering from

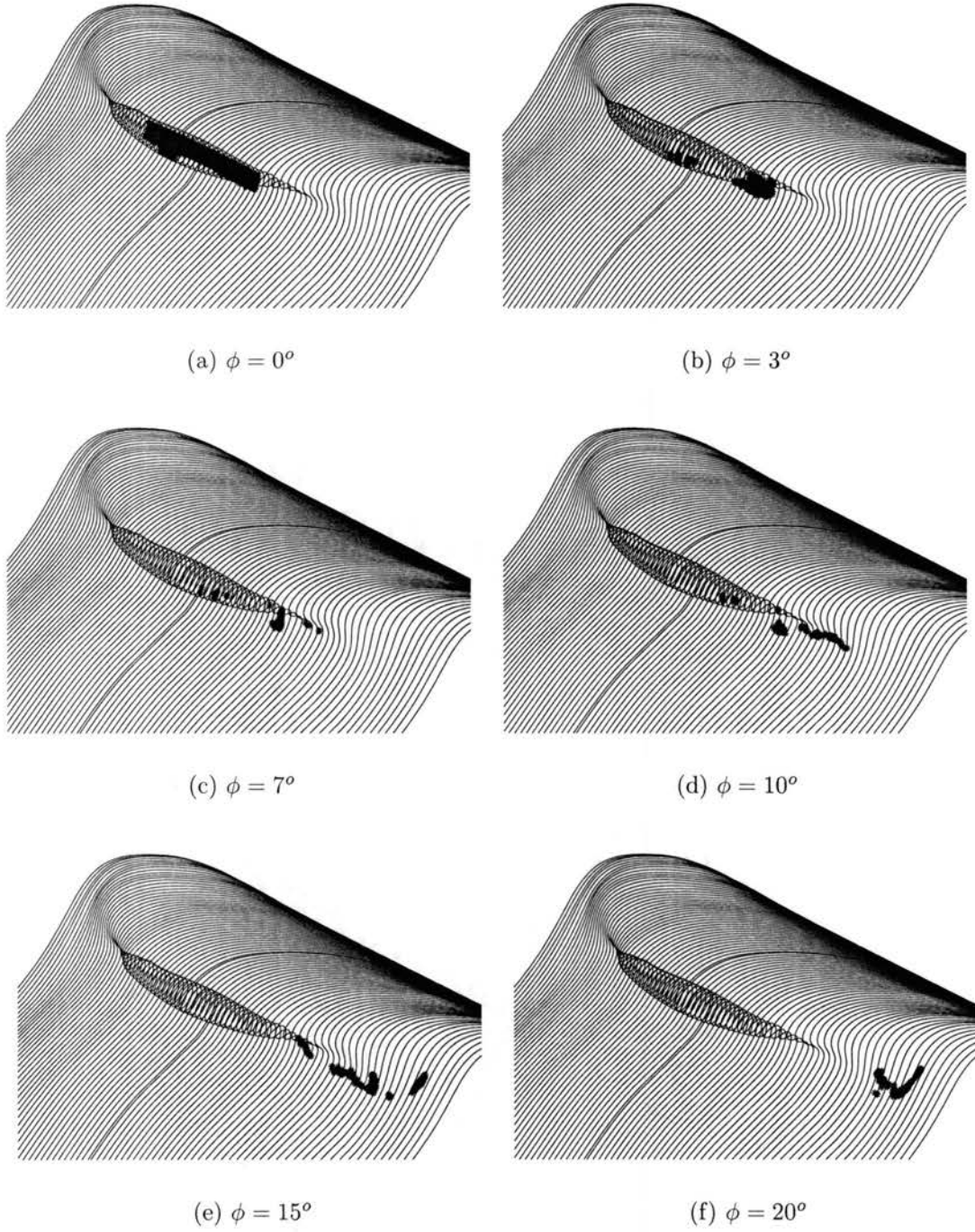


Figure 6.6: Position variation of specular reflection points on surface 15

surface 15 at  $3^\circ$  azimuth. This phenomena may be due to a similar effect. Consider the specular reflection points when the azimuthal angle equals  $13^\circ$  as shown in Figure 6.8(e). One of the reflection points is on top of the jet, while another is located in the cavity region near the azimuthal edge of the surface. The surface has a posi-



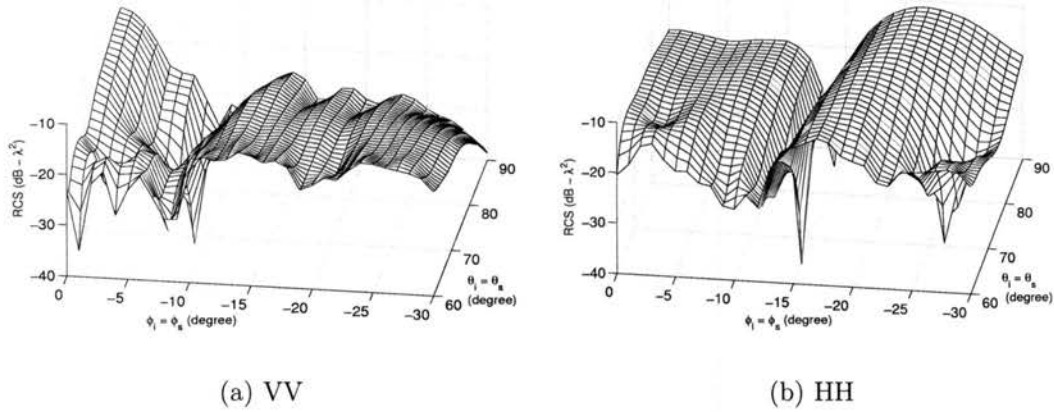


Figure 6.7: RCS of off-axis backscattering from surface 18.

tive radius of curvature in the azimuthal direction at the point on top of the crest, while it is negative at the point in the cavity region. This is similar to the case at VV polarization that leads to destructive interference, but with the surface and field rotated counter clockwise by  $90^\circ$ . This gives the observed interference null.

The destructive interference scattering mechanism is further illustrated in Figure 6.9. Part (a) shows the case where VV destructively interferes, but HH interferes constructively. In contrast, the configuration in part (b) leads to HH destructive interference, while VV interferes constructively. Note that the surface radii of curvatures at the reflection points should be somewhat smaller than the electromagnetic wavelength to give the destructive interference [2]. Here, this refers to the radii in range direction for case (a), and in the azimuthal direction for case (b). As seen in Figure 6.6(b), the specular reflection points on surface 15 at  $3^\circ$  azimuth similarly meet these conditions, which further supports this explanation. This effect is hereafter referred to as an “HH null” event.

Considering the above analysis, both super events (strong sea spikes) and HH null events should appear in the scattering from real sea surfaces which have complex rough wave crests. From the numerical treatments (especially in the 2-D simulations and 3-D upwave looking backscattering simulations), it has been seen that VV interference

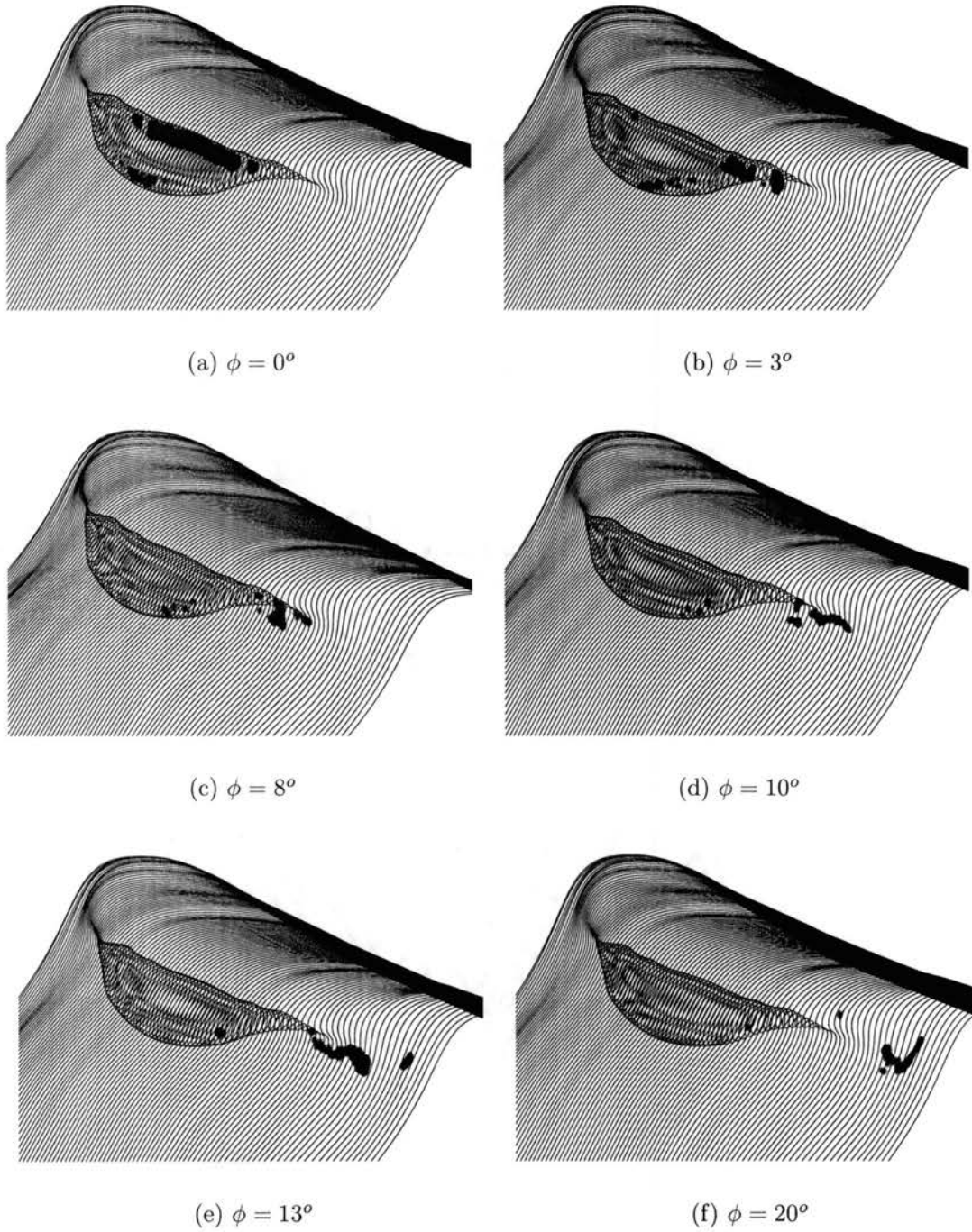


Figure 6.8: Position variation of specular reflection points on surface 18

nulls due to the reflections from the jet and cavity areas is one of the mechanisms that can lead to super events. However, the HH interference null is much less likely since the interference condition in azimuthal direction is seldom satisfied. When the off-axis backscattering or bistatic scattering from a single crest is considered, however,

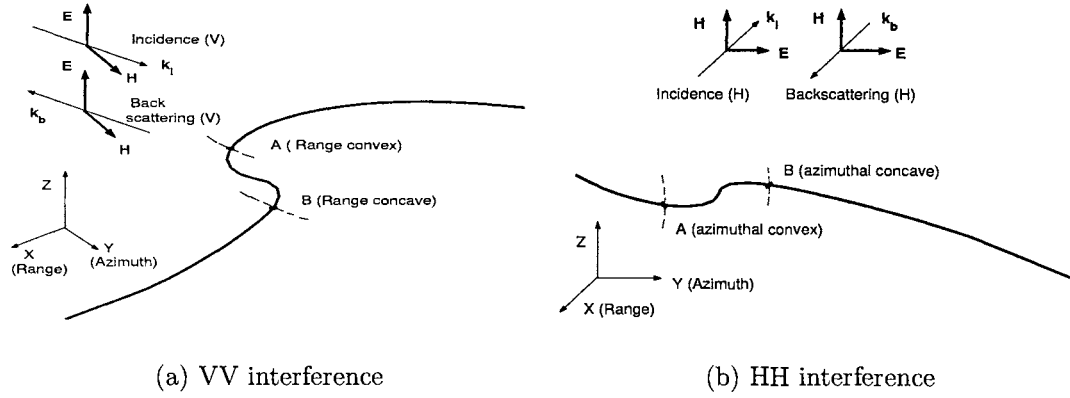


Figure 6.9: Illustration of destructive interference mechanisms

it is easily observed and identified as a scattering mechanism similar to that which causes the VV interference nulls.

## 6.5 Bistatic Scattering from Surface 12 and 18

Figure 6.10 shows the bistatic scattering from surface 12 when the illumination direction is  $\phi_i = 0^\circ$  and  $\theta_i = 80^\circ$ . The bistatic scattering is shown from  $\phi_s = 0^\circ$  to  $30^\circ$  and  $\theta_s = 60^\circ$  to  $90^\circ$ .

The cross-polarized scattering is stronger than in the corresponding monostatic case (although still small compared to the co-polarized scattering). It changes smoothly across the observation range. The dependence of the position of the VV (co-polarized) interference null on azimuth is similar to that in the backscattering case, although weaker. This results since the specular reflection points are somewhat different from those shown in Figure 6.4 due to the separation of the source and observation point. Because the incident direction remains unchanged, the specular reflection points move less rapidly with respect to the azimuthal observation angle, which leads to the slower and smoother variation of the bistatic scattering.

The co-polarization scattering characteristics (especially at VV) change abruptly as the azimuth angle moves through  $15^\circ$ . This is due to the surface shape. When

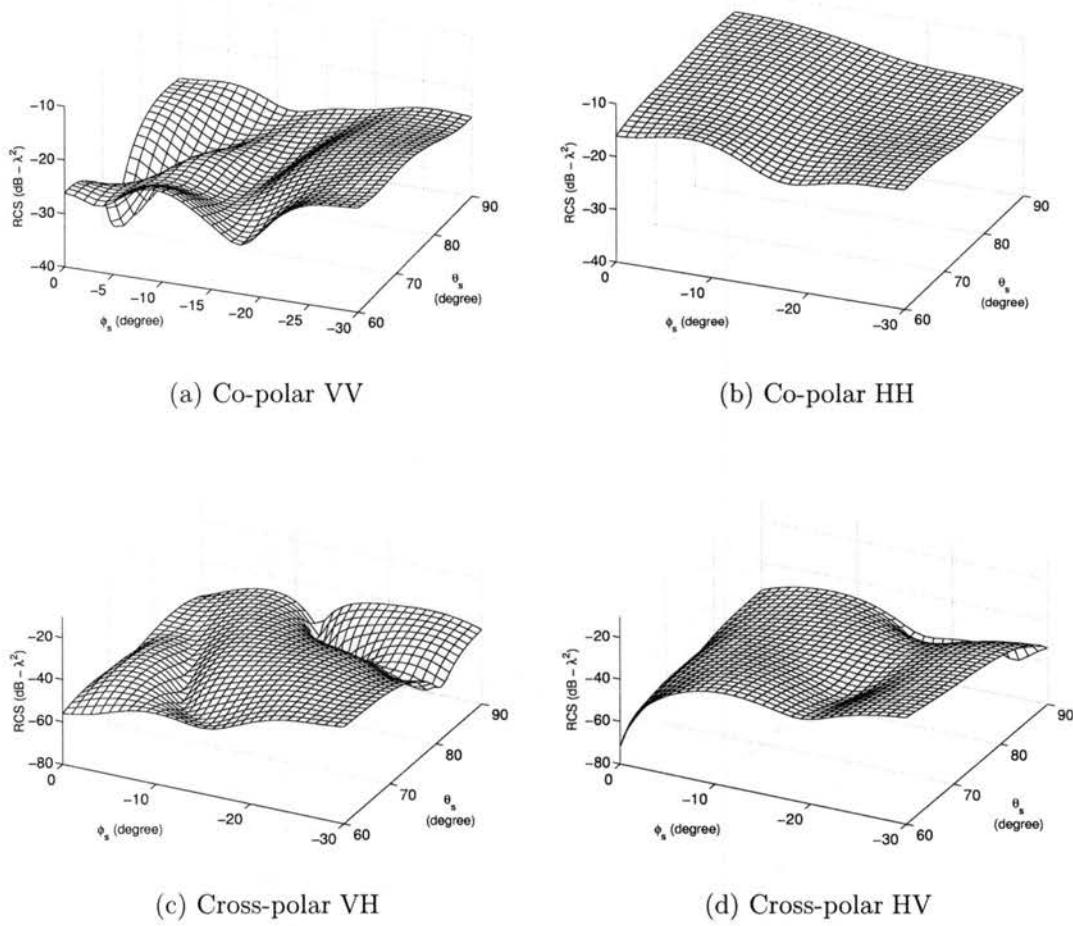


Figure 6.10: RCS of bistatic scattering from surface 12.

$\phi_s \leq 10^\circ$ , the specular reflection points are on the center of the crest, which therefore satisfy the curvature conditions that causes strong VV interference null. When  $\phi_s \geq 15^\circ$ , the reflection points are more on the side of the wave where the curvature at the reflection points does not support VV destructive interference. The rapid change (from VV null to flat response) occurs when the reflection points move from the center onto the side. The surface curvature at the reflection points changes quickly there.

Unlike the off-axis monostatic case, the cross-polarized bistatic VH and HV RCSs are considerably different. This is because they are no longer reciprocal cases due to the separation of source and observation point.

The bistatic scattering from surface 18 with the same illumination as Figure 6.10

is shown in Figure 6.11. Compared with the off-axis backscattering results of this surface in Figure 6.7, the co-polarized scattering again changes more smoothly with the azimuth angle. On the other hand, a significant VV interference null occurs at about  $\phi_s = 20^\circ$ , and a deeper HH interference null appears at  $\phi_s = 26^\circ$ . This results since the specular reflection points are again different for the monostatic and bistatic scattering cases. However, the mechanisms for interference nulls at both VV and HH are similar to those for backscattering.

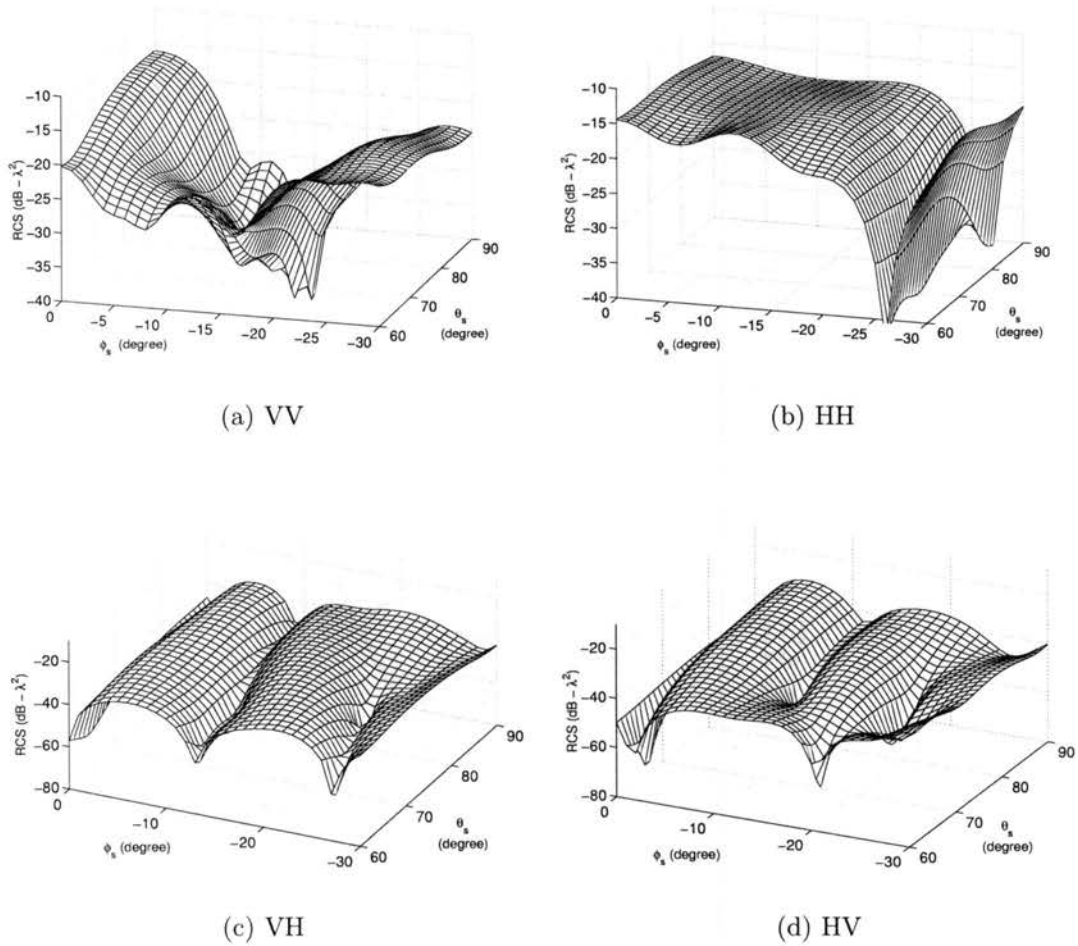


Figure 6.11: RCS of bistatic scattering from surface 18.

# Chapter 7

## Backscattering from Multiple-jet Wave Crests

### 7.1 Introduction

In the previous chapter, the polarimetric scattering from four 3-D test surfaces was discussed. The results, especially the off-axis backscattering, indicated that the mechanisms of scattering from different crest features were different. The destructive interference phenomenon was observed at both VV and HH in some cases. The interference effect strongly depends on the change of the positions of the specular reflection points on the wave crest with the change in the incidence azimuthal angle. The scattering mechanisms were easily identified due to the relatively simple crest structure that included only single jet.

When more complicated crests are considered, such as waves with multiple jet structures, the scattering will become more complex, with more reflection points interfering. This chapter focuses on the analysis of scattering from multi-jet test surfaces.

The 3-D multi-jet test surfaces are synthesized following a method similar to that used in the Chapter 5. The first step used in the synthesis is to interpolate three

profiles between each adjacent LONGTANK profile. For example, Figure 7.1 shows the profiles interpolated between profile 17 and profile 18, referred to as profile 17.25, profile 17.5 and profile 17.75. The other interpolated profiles are named following the same rule. The multi-jet test surfaces are synthesized by azimuthally aligning these interpolated profiles. They are formed to have multiple jets, with “cavity” regions between the adjacent jets. These “cavity” regions are formed by overlapping the side areas of the adjacent jets, also called “overlapped cavity region”.

Figure 7.2 illustrates the cross-section view of two example wave crests. Crest 1 has 3 identical jets ( $J_1$ ,  $J_2$ , and  $J_3$ ) with profile 18 as the central reference, 2 cavity regions ( $C_1$  and  $C_2$ ) with profile 17 as the central reference. The distance between two adjacent jet centers (or cavity centers)  $\Delta Y_1$  is named the jet period. Crest 2 has 4 jets with profile 18 as the central reference, and 3 cavity regions with profile 17 as the central reference. Different jet variations are synthesized by changing the central reference profiles of the cavity regions. For example, in Crest 2 of Figure 7.2, profiles 16, 17, 17.5 are used as the central reference profile of the cavity regions, giving the profiles marked by the dash-dotted line, solid line, and dotted line, respectively. For simplicity, these will be termed rough-ripple, medium-ripple, and smooth-ripple crests respectively. The jet period of crest 2 ( $\Delta Y_2$ ) is less than that of Crest 1. In later tests, crests with more random features where there is no fixed jet period, or the central reference profiles of individual jets or cavity regions are different, are generated.

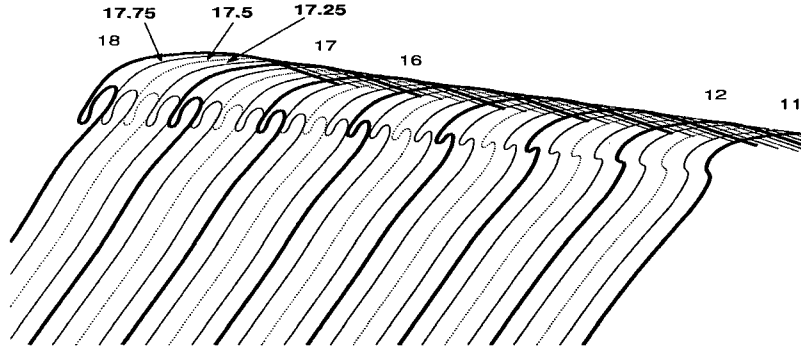


Figure 7.1: Interpolated LONGTANK case 2.4 profiles (11 to 18).

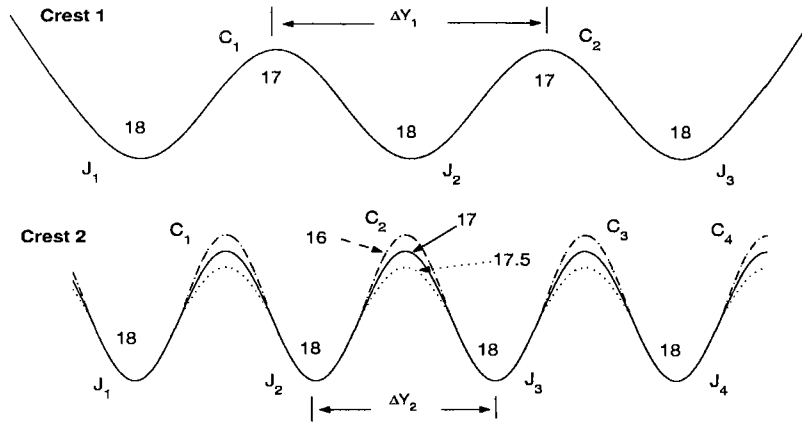


Figure 7.2: Illustration of the creation of multi-jet surface crests.

The analysis in this chapter will focus on the scattering from test surfaces which have various jet ripple magnitudes, jet periods, and varying number of jets. The relationship between the scattering results and the crest features are considered, and scattering mechanisms are identified.

## 7.2 Scattering Analysis of Multi-jet Wave Crests

Four related test surfaces are shown in Figure 7.3. The individual jets in each of these surfaces are identical, using profile 13 as the central reference profile. Part (a) shows the single-jet surface. Parts (b), (c) and (d) show 2-, 3-, and 5-jet surfaces, respectively. Profile 11 is used as the reference at the center of the cavity regions between each adjacent jets. The specular reflection points resulting with upwave looking incidence are marked in these surfaces. The MLFMA backscattering from these surfaces is shown in Figure 7.4. The RCS of the single-jet surface in part (a) is nearly the same as that in Fig.5.8 (d). Slight differences result from a change in curvature in the surface side regions. However, the jetting area dominates the scattering, giving a deep VV interference null. With the multi-jet surface cases, the depth of the VV null is somewhat smaller as the jet number increases, and the shape of the RCS curve changes slightly. This is because the back-reflections from the



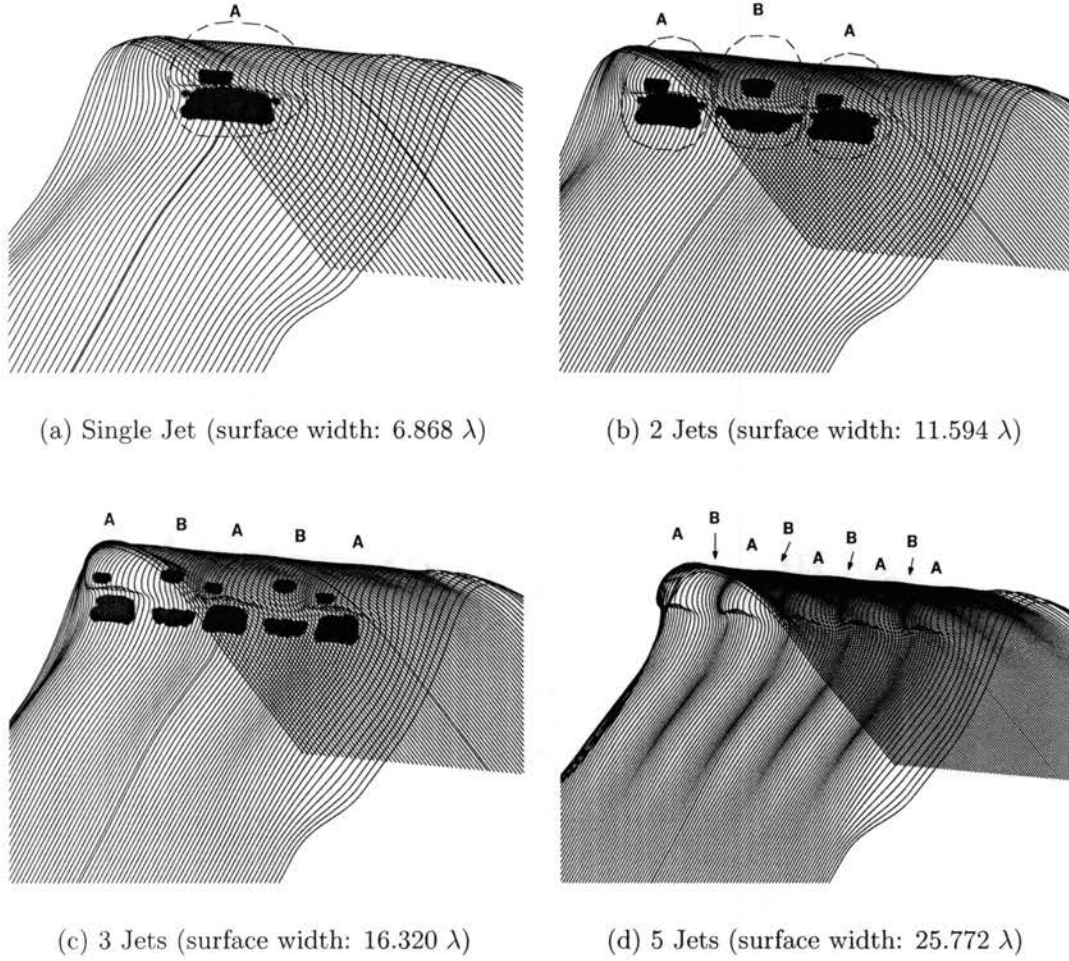


Figure 7.3: Multi-jet surfaces with marked reflection points ( $\delta \leq 4^\circ$ ).

cavity regions tend to reduce the destructive interference. Because the individual jets and cavity regions of these surfaces are identical, the specular reflection points always appear at the same positions on each jet or in each cavity region. The fields scattered from these individual regions therefore add constructively when looking upwave. Therefore, the RCS level of both VV and HH raises about 3 to 5 dB when a second jet is added in Figure 7.4(b). The VV null becomes slightly shallower due to the addition of the first cavity region. The scattering from an N-jet test surface can then be found using the superposition of the scattering from the one- and two-jet surfaces.

A synthesis procedure has been formed to predict the backscattering from the

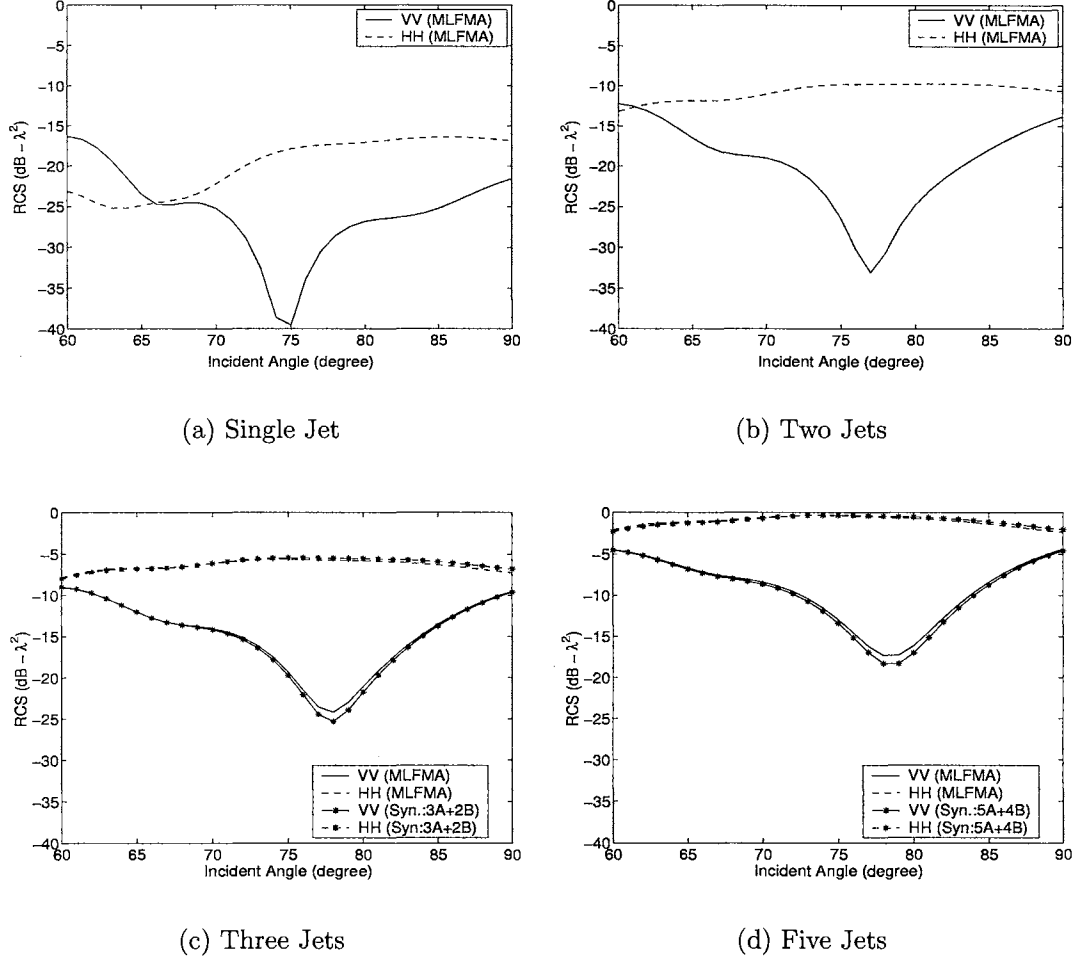


Figure 7.4: RCS of backscattering from multi-jet surfaces.

multi-jet crests. The scattering from the surface in Figure 7.3 (a) is termed the ‘A’ scattering from a single jet. The scattering from the region between two jets is then isolated using the scattering from the surface of Figure 7.3 (b). That is, the ‘B’ scattered fields from the cavity region is found by coherently subtracting twice the single-jet surface scattering from the two-jet surface scattering. The scattering from an N-jet surface can then be found using the coherent addition ‘(N)A+(N-1)B’. Synthesized 3- and 5-jet surface RCSs are compared with the MLFMA results for the complete surfaces in Figure 7.4. Excellent agreement is achieved at both polarizations for this test case.

This synthesis prediction method is significant because the large computational

cost of MLFMA may prevent the direct numerical computation of a very large surface. However, it may only be used in cases where the adjacent features do not interact significantly through multipath. Cases where this takes place will be observed later.

The 3-D EGO model was also applied to the multi-jet surfaces of Figure 7.3. Automated algorithms to identify specular reflection points and calculate the curvatures used in EGO were tested, but as with the single jet cases, the accuracy was again limited. Therefore, manually adjusted EGO parameters were again used for the four test surfaces. The 3-D EGO backscattering results are shown in Figure 7.5. 3-D EGO is much less accurate than the synthesized backscattering results. As discussed before, the 3-D EGO model is too sensitive to the positions and curvatures of the specular

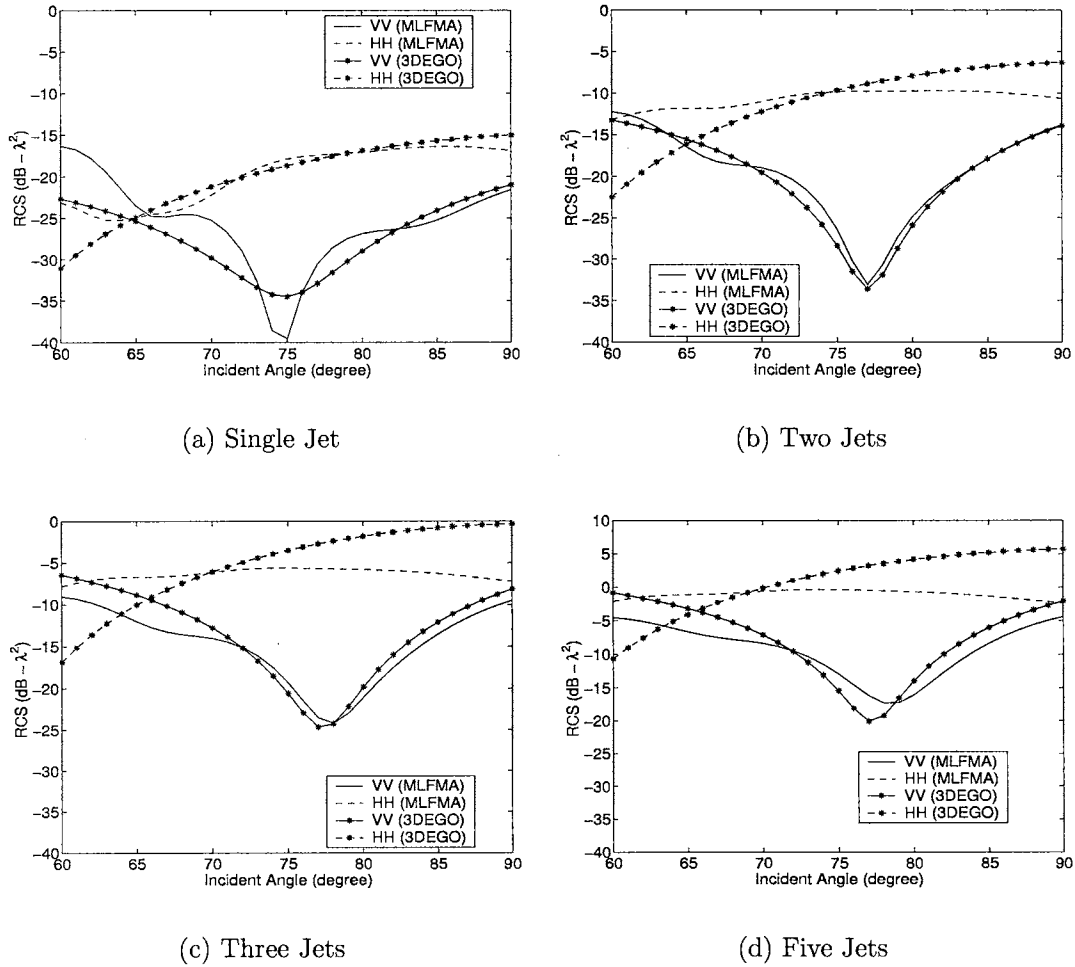


Figure 7.5: 3-D EGO results of multi-jet surfaces.

reflection points to provide accurate scattering based on a few dominant reflection points. However, it again clearly demonstrates physical scattering mechanism. Due to the limited accuracy, the 3-D EGO model is not further considered.

### 7.3 Scattering from Three-jet Crest Surfaces

In this section, the scattering from four different surfaces is examined. The crest of each surface has three identical jets. The ability of the synthesis procedure to predict the three-jet surface scattering from the one-jet and two-jet surface MLFMA scattering is tested on these surfaces. The comparison of the synthesized results with the MLFMA scattering from the full three-jet surface indicates the different scattering mechanisms in each case.

Figure 7.6 (c) shows a 3-jet surface. The central reference profile of each jet region is profile 13, while the cavity center profile is 12.5. The RCS of the surface is shown in Figure 7.6 (d). The solid line is VV and dashed line is HH. Compared to the single-jet result of surface 13 in Chapter 5, this 3-jet surface has a similar deep VV interference null. The interference between the reflections from the jetting areas and the cavity regions under the jets is therefore still significant. The specular reflection points marked in the figures show that the cavity region between two adjacent jets has reflection points similar to those of the jets. Also, there are two concave reflection points in each side cavity region of the crest. Because the reflection point distribution in this case is different from that in Figure 7.3, the synthesis procedure also changes. Figure 7.7 illustrates the crests of one-jet and two-jet.  $T_1$  and  $T_2$  are the reflection points on the jets,  $C_1$  and  $C_2$  are those in the cavity regions underneath the two jets.  $SC_1$  and  $SC_2$  are reflection points on the side cavity regions of the crest.  $T_3$  and  $CC_1$  are the reflection points in the middle region between the jets, on the top and in the cavity region respectively. The scattering from the full one-jet surface is termed ‘A’ scattering. ‘C’ scattering stands for the residual backscattering from the

2-jet surface after the ‘A’ scattering is coherently subtracted, and therefore includes the reflections from the points  $T_2$ ,  $C_2$ ,  $T_3$ , and  $CC_1$ . The synthesis ‘A+2C’ therefore represents the scattering from the 3-jet surface. The synthesized ‘A+2C’ scattering

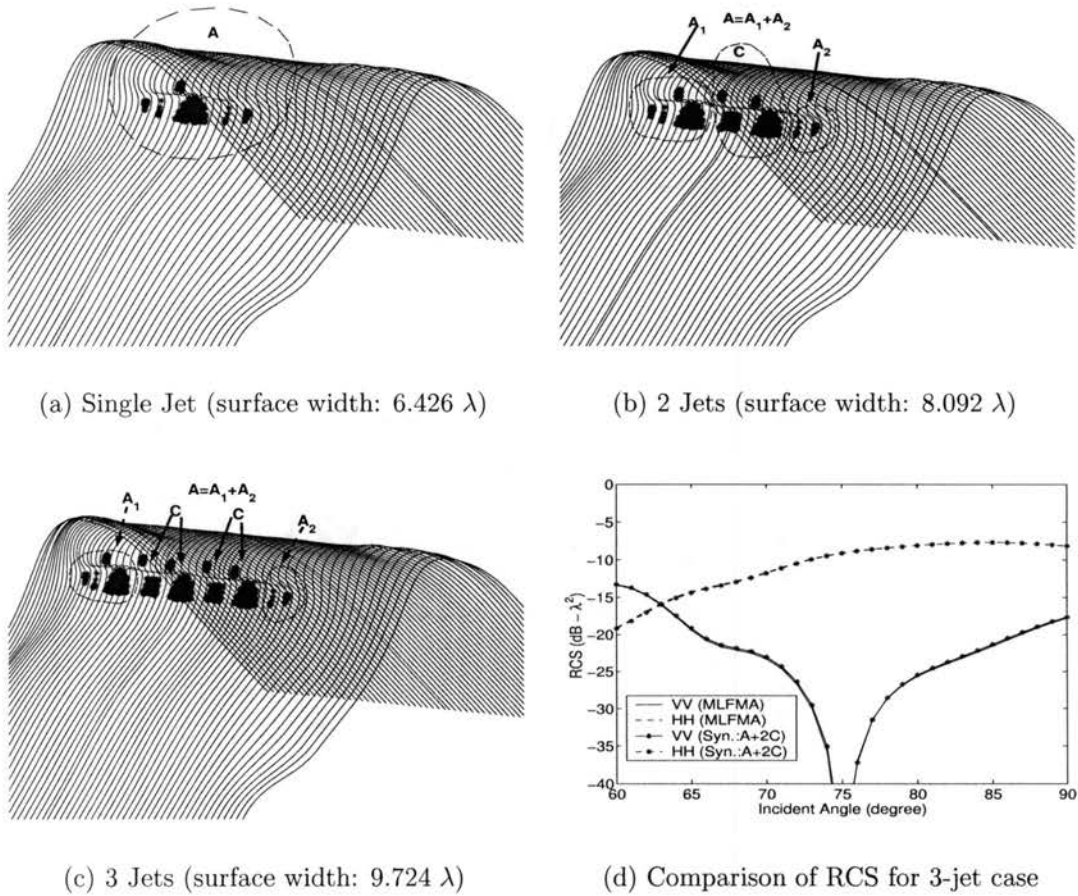


Figure 7.6: Illustration of 3-jet surface (Reference profile 13/12.5).

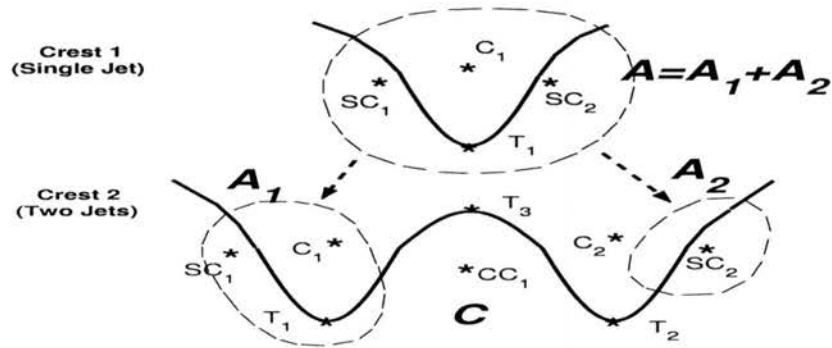


Figure 7.7: Illustration of reflection points on crest jets and in cavity regions.

is compared with the MLFMA scattering from the full surface in Figure 7.6 (d). The excellent agreement indicates that multiple interactions between the jets and cavities is small, and coherent superposition of the fields scattered from the individual scattering features is valid.

Figure 7.8 (c) shows another 3-jet surface. The reference profiles used in the surface formation are 18/17 at the jet/cavity region centers. For this scenario, due to the long jetting of profile 18, the size of a complete jet is bigger than that in Figure 7.6. Strong overlapping therefore occurs in the side regions of each jet when the 2-jet and 3-jet surfaces are generated. However, the ‘A+2C’ synthesis results still agree with the direct MLFMA results very well. In this case, the jetting areas totally

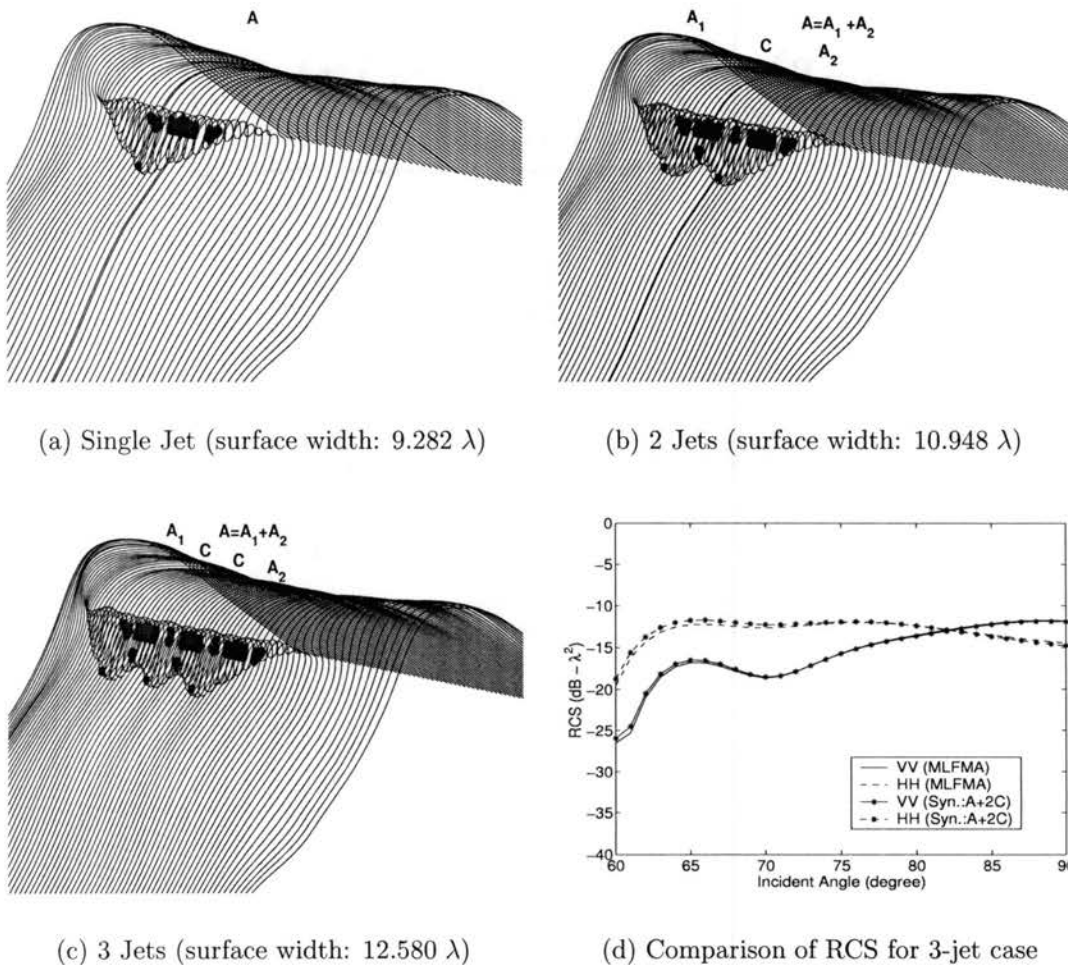


Figure 7.8: Illustration of 3-jet surface (Reference profile 18/17).

shadow the reflections from the points under the jets. Therefore, only a few dominant reflection points contribute to the backscattering. Little multiple interaction between the crest features takes place despite the large crest, which supports the constructive superposition for the multiple-jet cases. With no reflection from a concave surface point, the VV interference null does not occur.

The 3-jet surface in Figure 7.9 (c) is generated with the central reference profile 16/14 at the jet/cavity region center. Figure 7.9 (d) compares the synthesized backscattering with the full-surface MLFMA results. VV again shows good agreement, but HH is much poorer at high incidence. In the single-jet surface in Figure 7.9 (a), the medium-size jet shadows the middle part of the cavity region underneath the

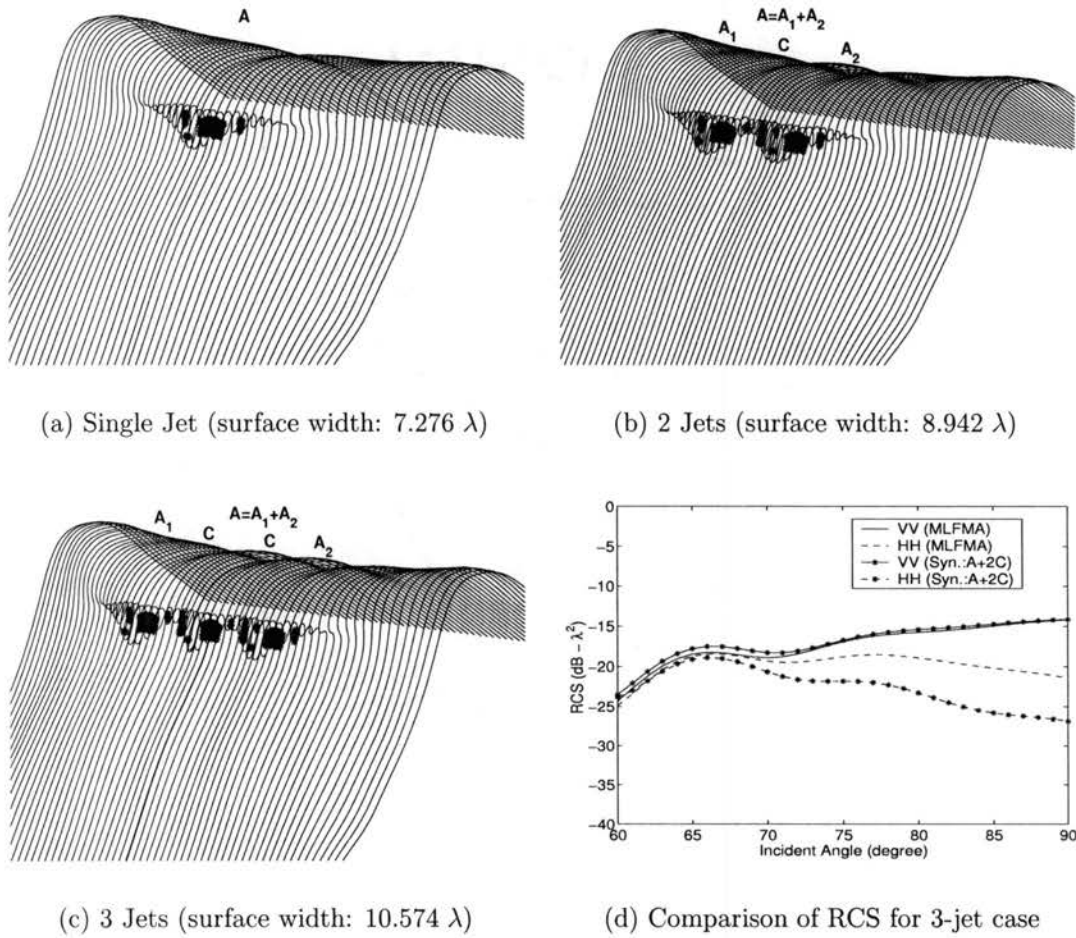


Figure 7.9: Illustration of 3-jet surface (Reference profile 16/14).



jet, while the side parts of the cavity region are only partially shadowed. For the 2-jet and 3-jet surface cases, the overlapped regions between adjacent jets have less jetting so the reflection points in these cavity regions are also only partially shadowed. The degree of partial shadowing depends upon the incident angle, being less severe at high incidence (low grazing).

Figure 7.10 shows the variation of the reflection points on the 2-jet surface at different incident angles.  $T_1$ ,  $T_2$ , and  $T_3$  stand for the convex reflection points on the top area of the crest.  $C_1$  and  $C_2$  are the concave reflection points in the cavity regions underneath the jets.  $SC_1$  and  $SC_2$  are the concave reflection points on the side regions of the crest. Finally,  $CC_1$  stands for the concave reflection points in the overlapped

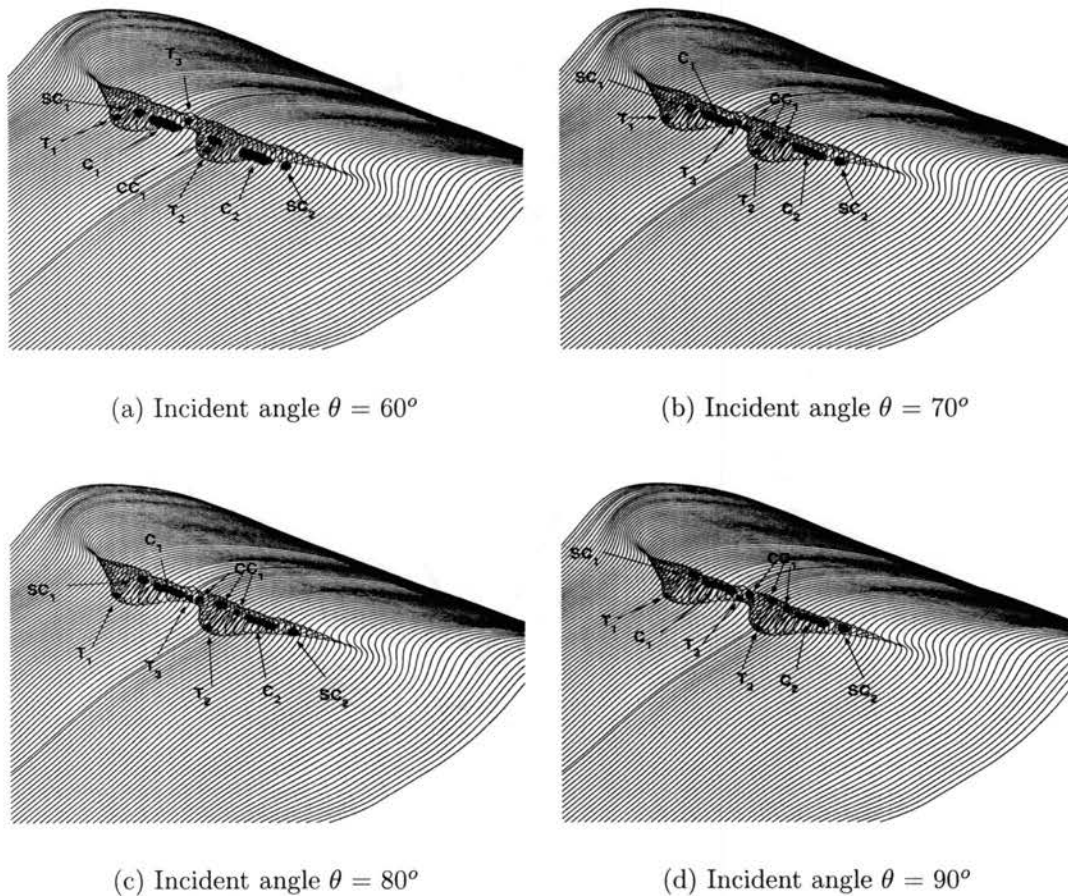
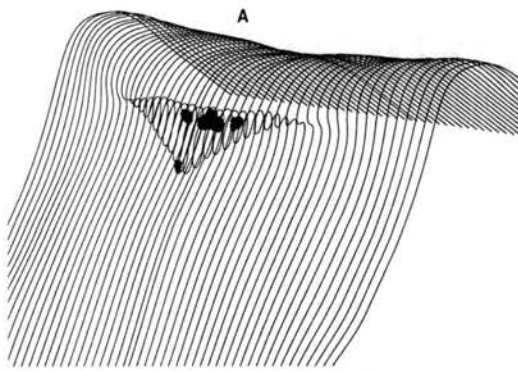


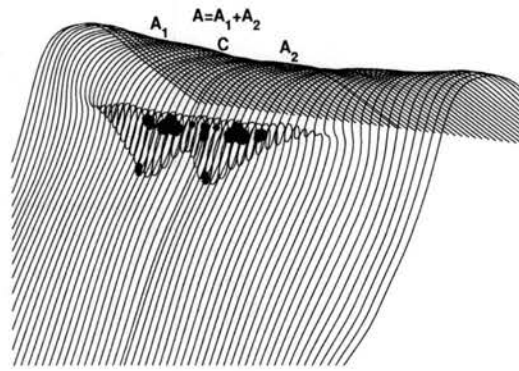
Figure 7.10: Reflection points on the 2-jet surface in Figure 7.9(b) at different incident angles.



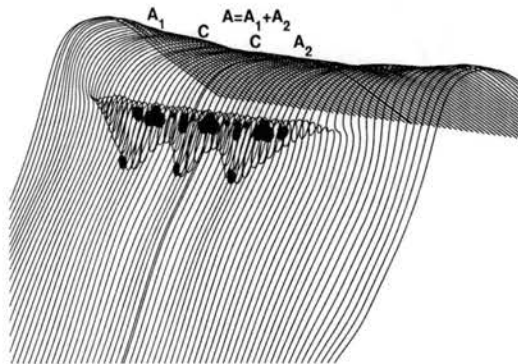
cavity region between the two jets. As mentioned, the VV interference null usually occurs when the reflections from  $T_1$  and  $T_2$  destructively interfere with the reflections from  $C_1$  and  $C_2$ . However,  $C_1$  and  $C_2$  are totally shadowed by the jetting parts in this case, so there is no significant VV null. On the other hand, the reflections from  $T_1$  and  $T_2$  (azimuthally convex) may interfere with the reflections from  $SC_1$ ,  $SC_2$ ,  $CC_1$  or  $T_3$  (azimuthally concave), which leads to HH destructive interference. As the incidence approaches grazing, the unshadowed cavity region gets larger, and the reflection points move to the positions where the surface radii of curvatures are different. The HH destructive interference therefore becomes stronger. There is some interaction between the individual scattering regions, the simple ‘A+2C’ coherent



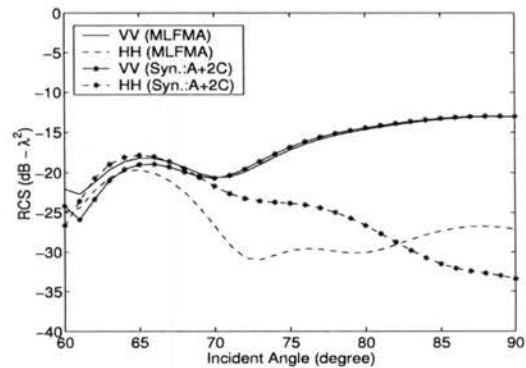
(a) Single Jet (surface width:  $8.738 \lambda$ )



(b) 2 Jets (surface width:  $11.628 \lambda$ )



(c) 3 Jets (surface width:  $12.036 \lambda$ )



(d) Comparison of RCS for 3-jet case

Figure 7.11: Illustration of 3-jet surface (Reference profile 18/16).

superposition is no longer perfectly accurate.

Figure 7.11 (c) shows another 3-jet surface. The central reference profiles are 18/16 at the jet/cavity region centers. In this case, the jetting area is narrower than that in Figure 7.8 (c), and partial shadowing of the cavity below the jets occurs in the overlapped cavity regions between the jets and the side regions of the crest. A detailed identification of the reflection points on the 2-jet crest is given in Figure 7.12. No significant VV destructive interference occurs because the reflections from  $C_1$  and  $C_2$  are totally shadowed. The HH destructive interference occurs because  $T_1$  and  $T_2$  are azimuthally convex and  $SC_1$ ,  $SC_2$  and  $CC_1$  are azimuthally concave in the electric field plane. The simple 'A+2C' coherent synthesis loses accuracy at HH, but still predicts HH destructive interference.

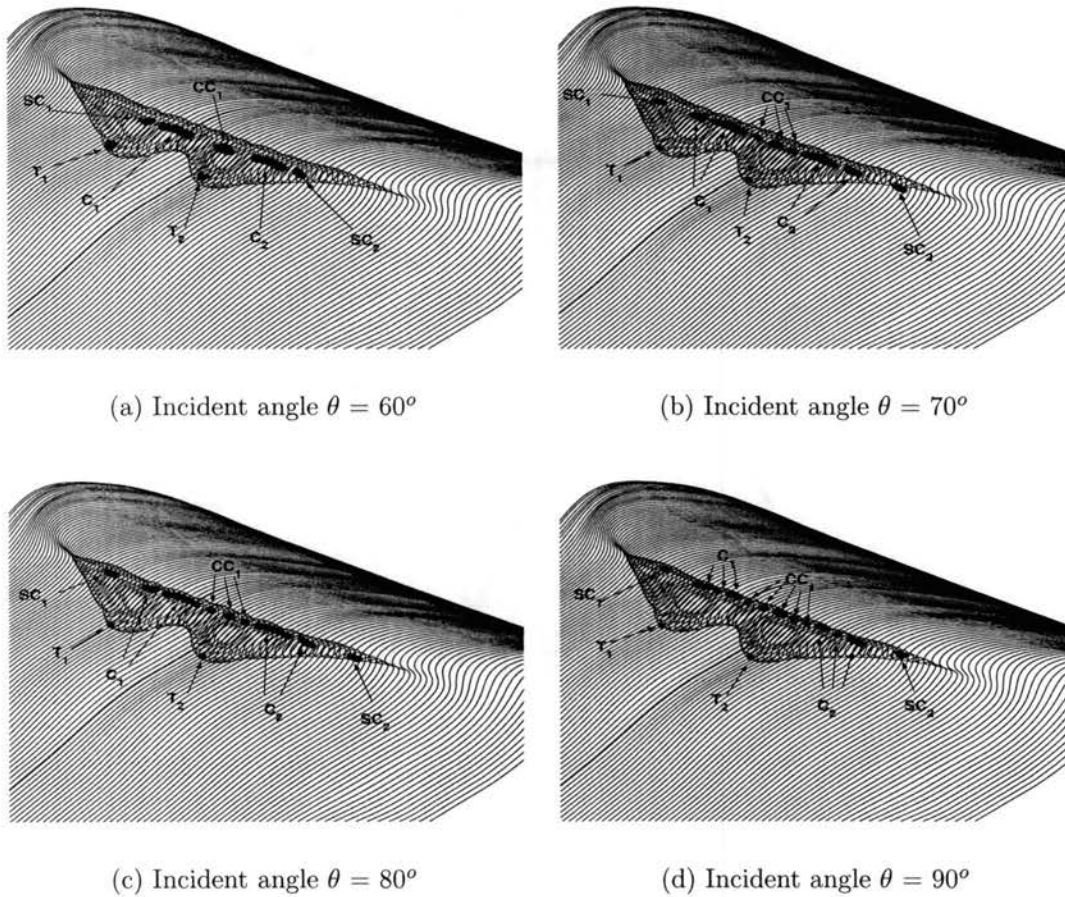


Figure 7.12: Reflection points on the 2-jet surface in Figure 7.11(b) at different incident angles.

## 7.4 Scattering from Six-jet Crest Surfaces

### 7.4.1 Jet Period

The backscattering from 6-jet test surfaces is analyzed in this section. The six jets are identical within each surface. The crest characteristics of different surfaces are different due to either different central reference profiles or a variation of the jet sizes. The scattering phenomena associated various crest features are identified and compared. Figures 7.13 (a), (b) and (c) show three 6-jet test surfaces, each of which have reference profiles 13/12 at their jet/cavity region centers. The surfaces

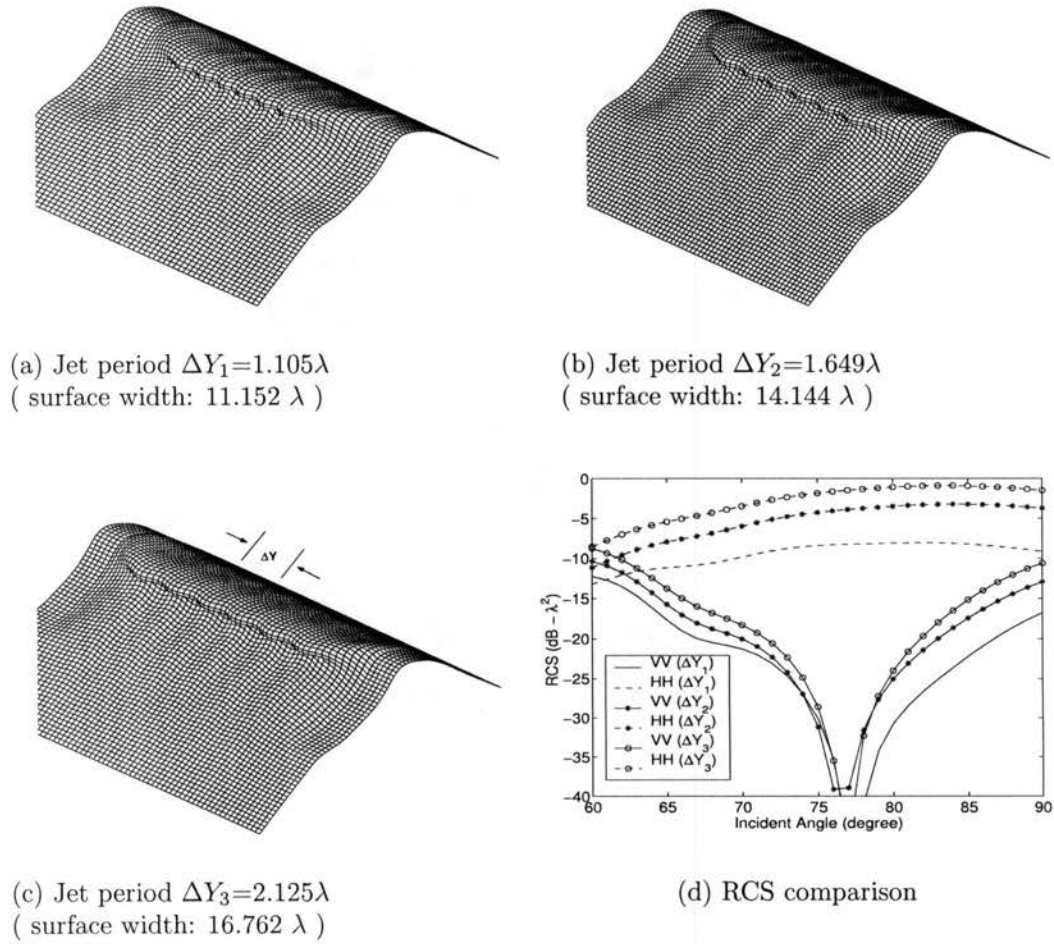


Figure 7.13: Six-jet surfaces (Ref. profile 13/12) with different jet period.

differ in that their jet periods are varied. (As previously defined, jet period stands for the distance between the centers of two adjacent jets). Thus, the different jet periods give different surface widths, and different azimuthal curvatures at specific points on these surfaces. The jet periods ( $\Delta Y$ ) of the three surfaces in Figure 7.13 are  $1.105 \lambda$ ,  $1.649 \lambda$  and  $2.125 \lambda$  respectively. The backscattering from these surfaces is shown in Part (d) of this figure. In each case, there is a deep VV interference null at approximately  $77^\circ$  incidence. This indicates that a crest expansion or compression in the azimuthal direction does not change the dominant scattering mechanism for the crest. This is not surprising since the positions of the convex and concave reflection points and their range-direction curvature remain almost unchanged. The RCS level at both VV and HH shifts upward with increasing jet period since the azimuthal radius of curvature at the dominant reflection points also increases as the jet size gets bigger.

The surfaces in Figures 7.14 (a), (b) and (c) have the same azimuthal jet periods as those in Figure 7.13, but the central reference profile is changed to 18/17 at the jet/cavity region centers. The larger jets totally shadow the reflections from the concave regions under the jets, so no significant destructive VV interference occurs. The main effect of the jet period is again simply to raise or lower the overall scattering.

## 7.4.2 Jet Magnitude

As observed above, a change in the jet period introduces little change to the scattering other than. Now, the analysis is focused on the effect of the magnitude of the jetting when the surfaces have an identical jet period.

Figure 7.15 (b) shows the same surface as that shown in Figure 7.13 (b), with central reference profiles of 13/12 and a jet period of  $1.649 \lambda$ . Parts (a) and (d) of Figure 7.15 use the same azimuthal jet period as part (b), but the central reference profiles are 13/12.5 in part (a), and 13/11 in part (c). The surfaces are

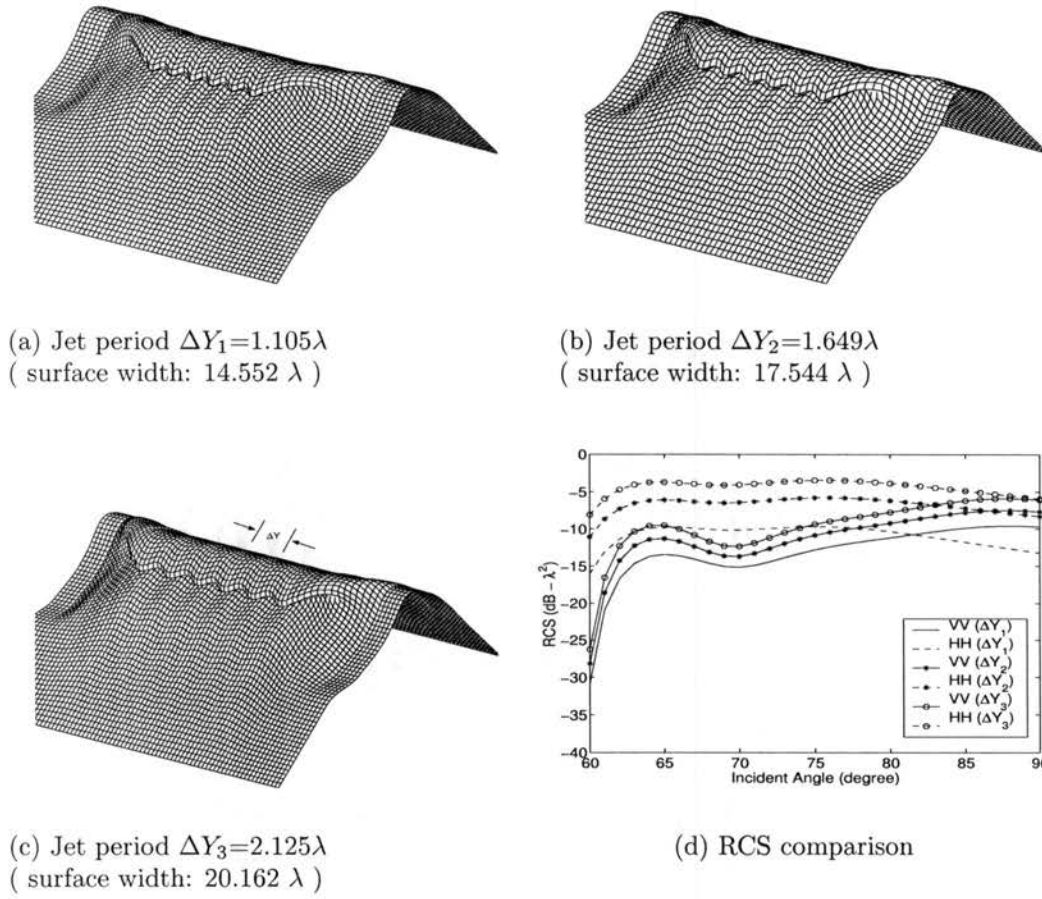


Figure 7.14: Six-jet surfaces (Ref. profile 18/17) with different jet period.

termed ‘smooth-ripple’, ‘medium-ripple’ and ‘rough-ripple’ for parts (a) through (c), respectively, corresponding to the azimuthal “ripple” that the multiple jets form on the crest. Figure 7.15 (d) gives the scattering from these surfaces. The scattering from the ‘smooth-ripple’ surface has a deep VV interference null similar to that with the ‘medium-ripple’ case, but at slightly higher incidence. The dominant scattering mechanisms are therefore similar. The ‘rough-ripple’ case, however, has very different results. There is only a shallow VV interference null, and the HH scattering drops about 3 to 5 dB overall. This difference results from the reflections from the regions between adjacent jet pairs, which reduces the original destructive interference at VV, and simultaneously introduces some destructive interference at HH. At the same time,

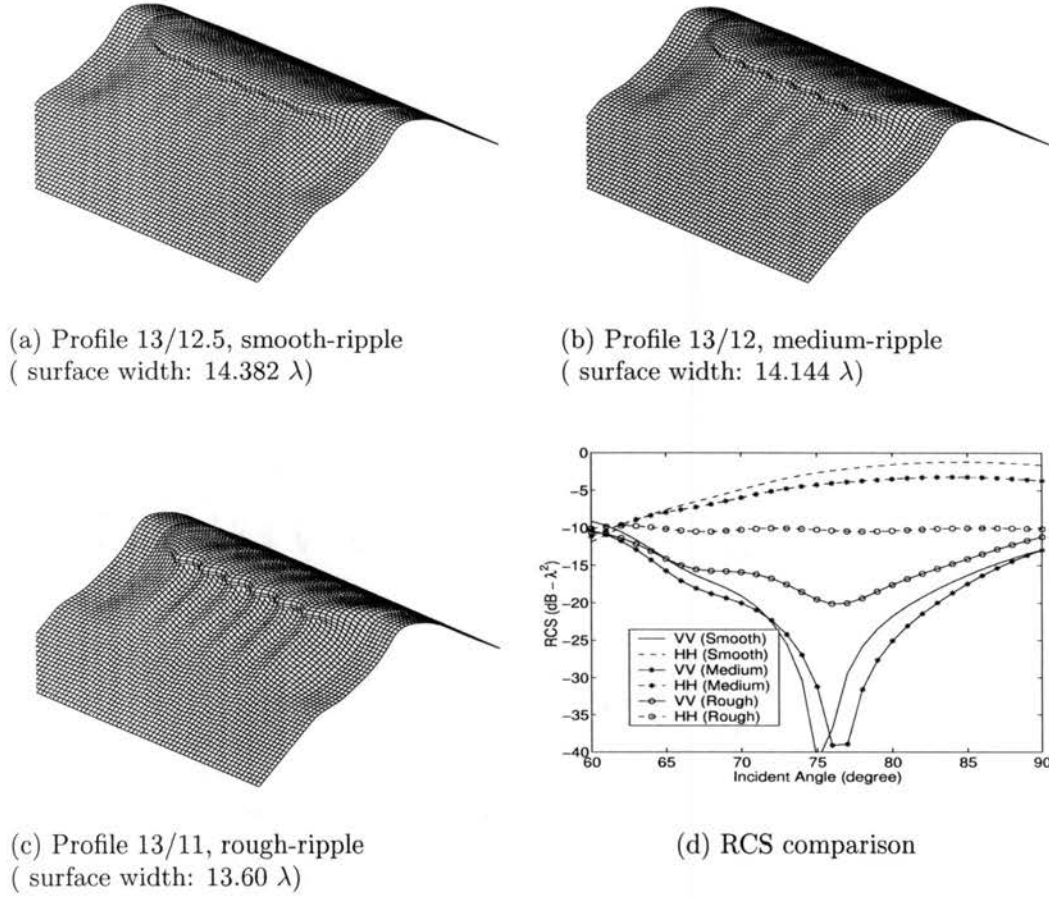


Figure 7.15: Six-jet surfaces (Ref. profile 13 at jet centers) with different ripple feature.

the ‘rough-ripple’ leads to the greater curvature at the reflection points, which is also a possible factor to reduce HH scattering because, in geometrical optics model, the reflected field is directly related to the surface radii of curvature at the reflection points.

The synthesis procedure illustrated in Figure 7.7 is now applied to the surfaces of Figure 7.15. As mentioned, ‘A’ scattering in Figure 7.7 includes two types interference. One is the interference of the reflections from the convex jet top  $T_1$  and the concave cavity region  $C_1$ , which leads to VV destructive interference. The other is the interference of the reflections from the jet top  $T_1$  (azimuthal convex) and the side cavity region  $SC_1$  and  $SC_2$  (azimuthally concave), which causes the destructive

interference at HH. Figure 7.16 (a) shows the single-jet ‘A’ scattering from each of the surfaces in Figure 7.15. The VV scattering is almost identical in the three cases, including the interference null, because they have the same reference profiles at the jet centers. Thus the identical  $T_1$  and  $C_1$  give the same VV interference. At the same time, the reflections from  $SC_1$  and  $SC_2$  give different interference with the reflection from  $T_1$  at HH. The HH destructive interference of the ‘rough-ripple’ case is stronger than the other two cases because less shadowing occurs in the side regions  $SC_1$  and  $SC_2$ , especially at large incident angles.

Figure 7.7 shows that the ‘C’ backscattering results not only from the overlapped region, but also partially from the jet top  $T_2$  and the cavity region  $C_2$  underneath the jet. In other words, the ‘C’ scattering actually results from interference between the reflections from the jet top  $T_2$ , the cavity region  $C_2$ , and the overlapped region points  $T_3$  and  $CC_1$ . Figure 7.16 (b) shows the ‘C’ scattering corresponding to the surfaces in Figure 7.15. Because  $T_2$  and  $C_2$  are exactly the same as  $T_1$  and  $C_1$ , they should produce the same scattering effect, a deep VV null. However, due to the interference with of the reflection from the overlapped region, the VV null almost disappears in the ‘rough-ripple’ case. For the ‘smooth-ripple’ and ‘medium-ripple’ cases, the reflections from the cavity of  $CC_1$  are mostly shadowed, the VV nulls that result from  $T_2$  and

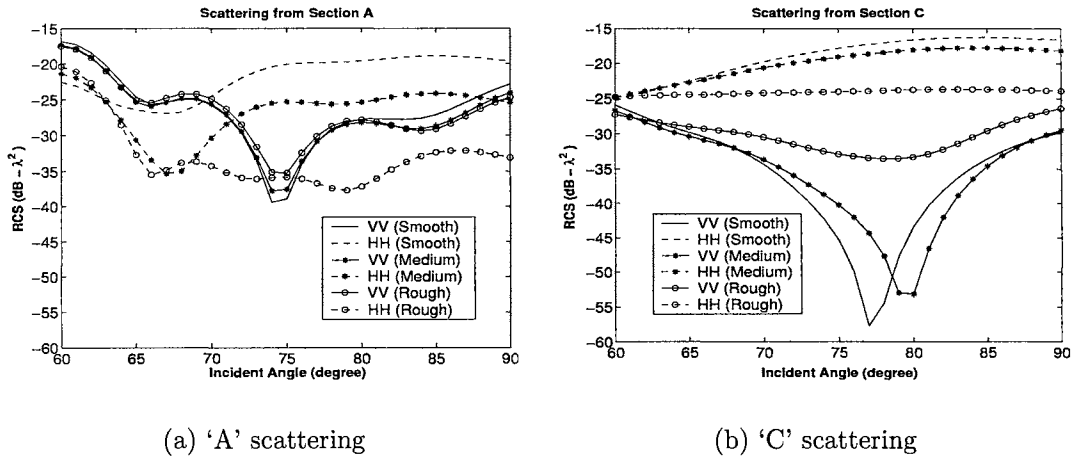


Figure 7.16: Comparison of the scattering from section A and C respectively.



$C_2$  therefore still appear. The scattering from six-jet surfaces in Figure 7.15 (d) looks very much like the ‘C’ scattering since the fields scattered from six-jet surface can be coherently synthesized as ‘A+5C’. Multiple interactions between features that are not represented in the synthesis are negligible.

The three surfaces shown in Figure 7.17 are similar to those in Figure 7.15, but the central reference profiles are 18/17.5 in part (a), 18/17 in part (b), and 18/16 in part (c). The RCS shown in Figure 7.17 (d) indicates there is no strong VV dependence on the jet amplitude. No VV interference nulls appear due to the shadowing of the cavity

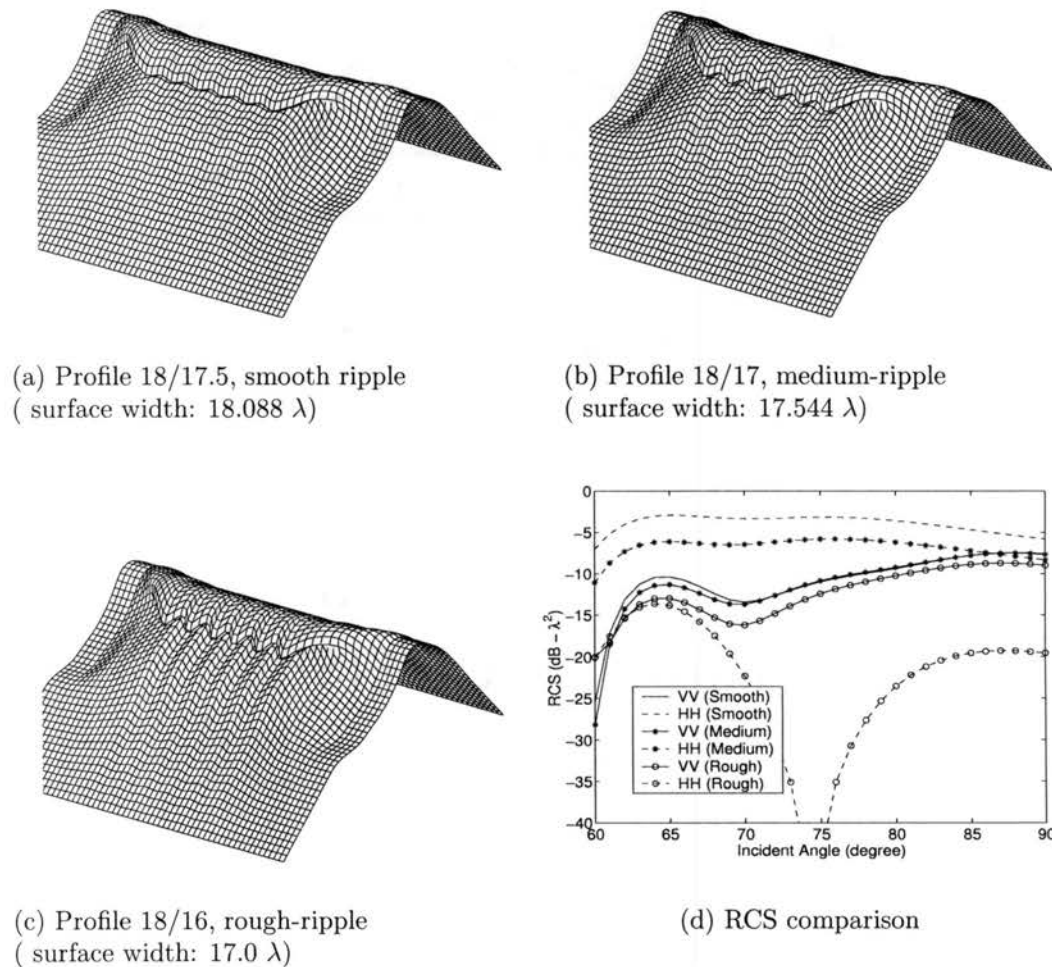


Figure 7.17: Six-jet surfaces (Ref. profile 18 at jet centers) with different ripple feature.



by the jetting area. However, more complicated HH scattering occurs in ‘rough-ripple’ case, especially when incidence approaches grazing. A deep HH interference null is formed at about  $74^\circ$  incident angle.

Figure 7.18 shows ‘A’ and ‘C’ scattering corresponding to the surfaces in Figure 7.17. Due to the large jetting, both the cavity region  $C_1$  and the side regions  $SC_1$  and  $SC_2$  are totally blocked from the incident field. Scattering ‘A’ results only from the scattering from the jet top area  $T_1$ . There is therefore little difference between the three cases, except that the RCS level slightly raises or lowers due to the different azimuthal curvatures. The ‘C’ scattering of the ‘smooth-ripple’ and ‘medium-ripple’ cases are similar. No significant interference nulls occur at either VV or HH since the overlapped cavity regions  $CC_1$  are totally shadowed by the large jetting areas. The ‘C’ scattering from ‘rough-ripple’ surface, however, shows strong destructive interference at HH as the incident angle increases beyond  $66^\circ$ . This is because the reflection from the jet  $T_2$  interferes with the reflections from the overlapped region  $T_3$  and  $CC_1$ . The cavity region  $CC_1$  of this ‘rough-ripple’ crest is only partially shadowed. Note that the scattering from the 6-jet ‘rough-ripple’ surface in Figure 7.15 is much different from that of the corresponding ‘C’ scattering shown in Figure 7.18 (b). This indicates that multiple interactions between the individual features take place while the

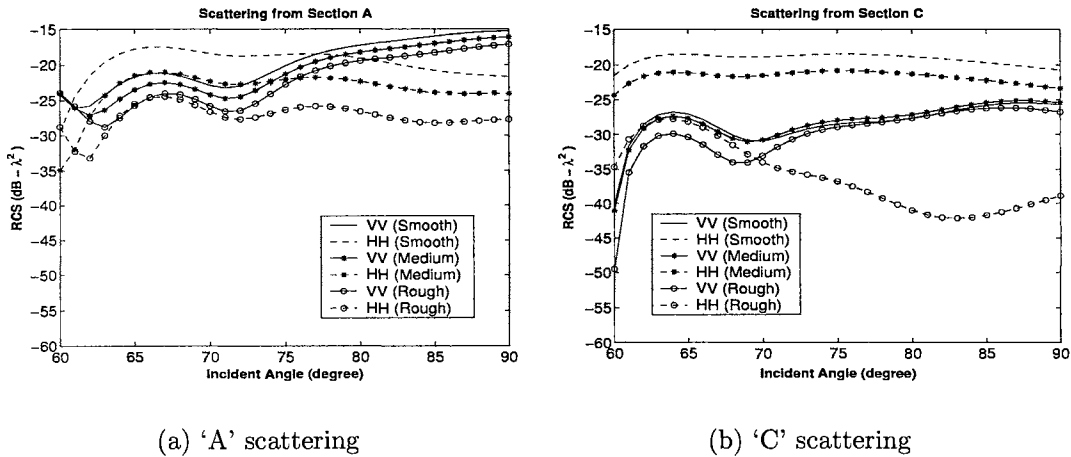


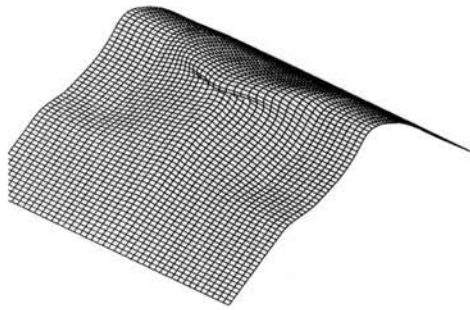
Figure 7.18: Comparison of the scattering from section A and C respectively.

destructive interference occurs. The scattering is no longer predicted by the simple coherent synthesis from scattering ‘A’ and ‘C’. The relative scattering mechanisms will be further examined in the next section.

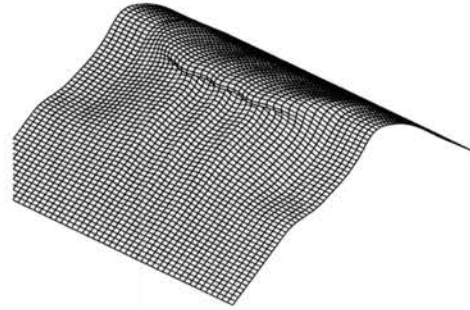
## 7.5 Scattering from Series Multi-jet Surfaces with Identical Jet Features

In this section, the constructive superposition synthesis and interference phenomena as the number of the identical jets increases is considered. A series of profiles with the number of jets ranging from 1 through 12 were synthesized. The central reference profiles were 13/12 for the jet/cavity region in each case. Figure 7.19 shows the 3-, 6-, and 12-jet surfaces. The six jet surface also appeared in Figure 7.13 (b). The azimuthal widths of these surfaces become larger as the number of jets increases since identical jet sizes and periods are used in all cases. Figure 7.20 (a) shows the RCSs of the 3- through 12-jet surfaces. Overall, both VV and HH scattered fields increase uniformly as the number of jets increase. Multiple interactions are therefore small. As examined in Section 7.2, the scattering from multiple-jet surfaces may be coherently synthesized from the fields scattered from the single-jet and 2-jet surfaces. Also, the cavity between jets has little contribution. The absolute RCS level increases linearly with jet number (logarithmically in dB).

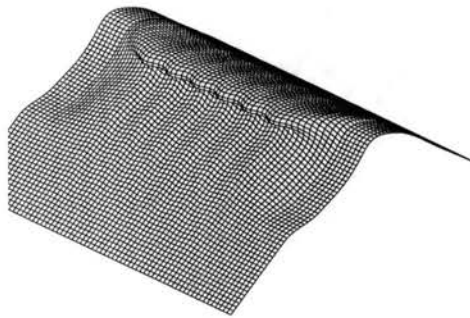
A second example is given in Figure 7.20 (b). The plotted backscattering is from the series of surfaces shown in Figure 7.21. The surfaces have 1 through 6 jets with the central reference profile 18/16. The 6-jet case was discussed in Figure 7.17 (c). The VV scattering increases linearly with the number of jets as in Figure 7.20 (a). The reflection points of the single-jet case dominate the VV scattering. The overlapped regions that appear as more jets are added have little effect. However, when the incident angle is above  $66^\circ$ , the RCS at HH varies significantly as the jet



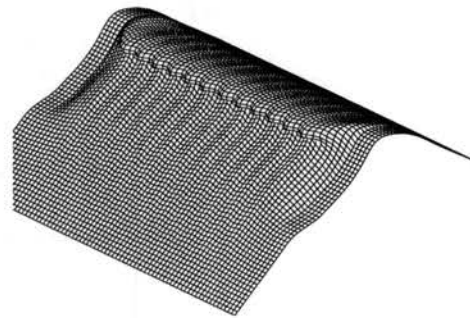
(a) Single Jet (surface width:  $5.882 \lambda$ )



(b) 3 Jets (surface width:  $9.180 \lambda$ )

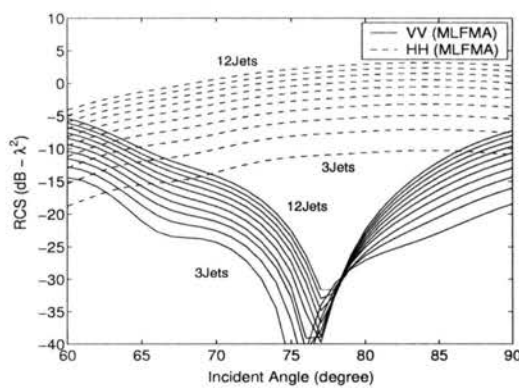


(c) 6 Jets (surface width:  $14.144 \lambda$ )

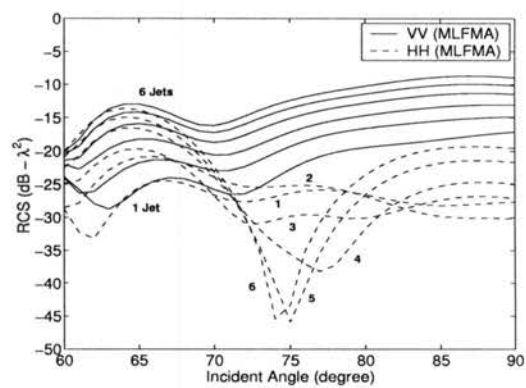


(d) 12 Jets (surface width:  $24.04 \lambda$ )

Figure 7.19: Series surfaces (Ref. profile 13/12) with identical jet size and period.



(a) Surfaces with ref. profile 13/12



(b) Surfaces with ref. profile 18/16

Figure 7.20: RCS comparison of backscattering from multi-jet surfaces.

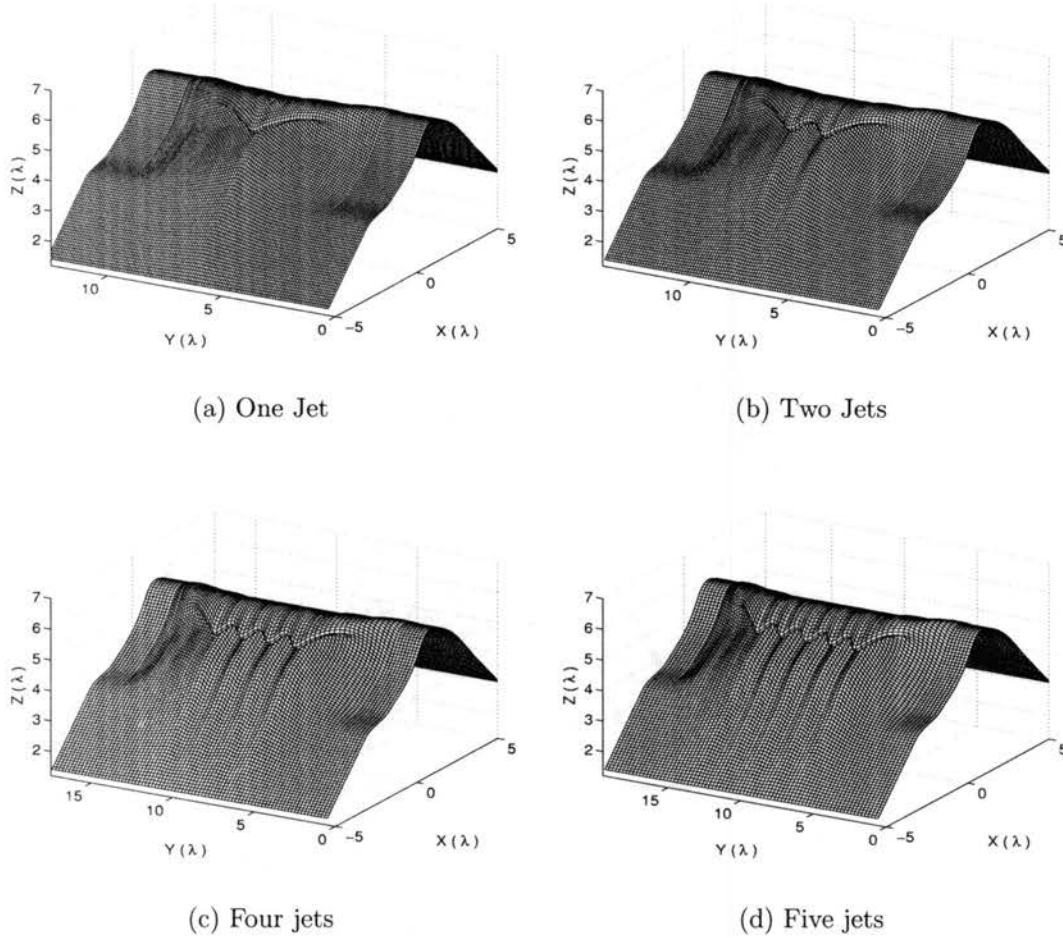


Figure 7.21: Series surfaces (Ref. profile 18/16) with identical jet size and period

number increases. As the number of jets increases from 1 to 5, the HH destructive interference increases until a -45dB deep null is formed. The overlapped region is therefore important in this case. The 6-jet case, which is similar to the 5-jet case, was analyzed in Figure 7.17 (c). Figure 7.22 and Figure 7.23 show the reflection points on the 2-jet and 4-jet surfaces at  $60^\circ$ ,  $70^\circ$ ,  $80^\circ$ , and  $90^\circ$  incident angle, respectively. As shown in these figures, all the concave reflection points in both the cavity regions under the jets ( $C_i$  and  $SC_i$ ) and the overlapped cavity regions between adjacent jets ( $CC_i$ ) are totally shadowed by the bigger jetting area at incidence angles less than  $66^\circ$ . The scattering, therefore, comes only from the reflection points on the jetting areas ( $T_i$ ) of the surfaces. Thus, no VV and HH interference occurs. As the

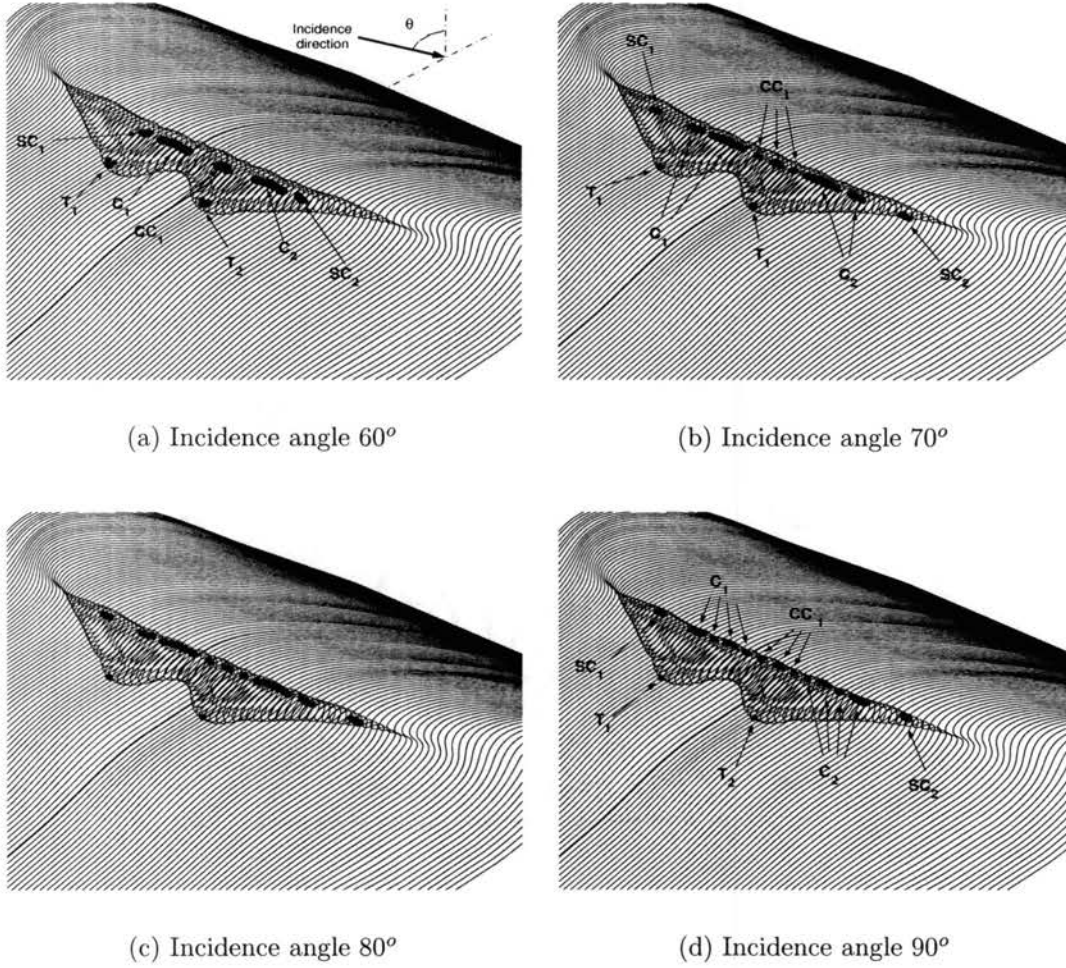
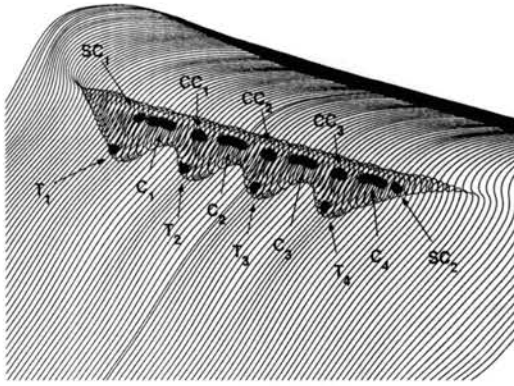


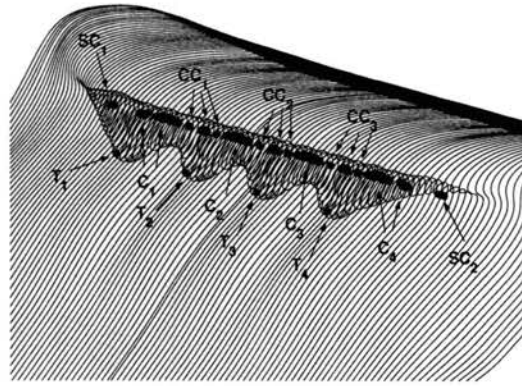
Figure 7.22: Reflection points on the 2-jet surface, at different incident angles.

incidence approaches grazing, the HH scattering varies dramatically as the number of jets increases. This indicates that some multiple interactions take place, so it is difficult to directly identify the mechanisms that lead to the HH reduction.

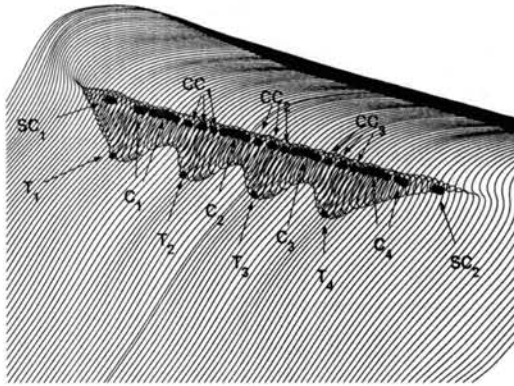
The two previously used synthesis procedures are also performed on the crests of Figure 7.21, illustrated in Figure 7.24. Part (a) shows that the scattering from the full 2-jet surface can be represented using '2A+B'. In this case, the effects of  $SC_1$  and  $SC_2$  are ignored, and 'B' scattering represents only the reflections from the overlapped region between the jets. The N-jet surface scattering therefore should be '(N)A+(N-1)B'. Part (b) uses 'A+D' to represent the full 2-jet scattering so that the reflection from  $SC_1$  and  $SC_2$  is considered in 'A' scattering, and the interference



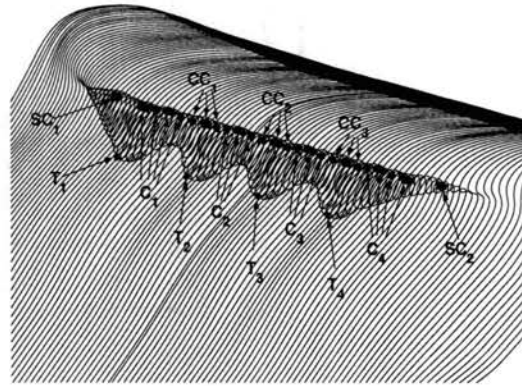
(a) Incidence angle  $60^\circ$



(b) Incidence angle  $70^\circ$

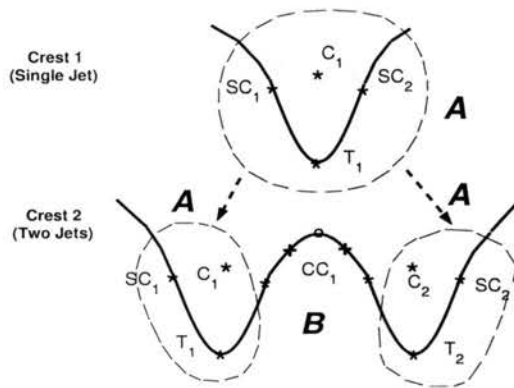


(c) Incidence angle  $80^\circ$

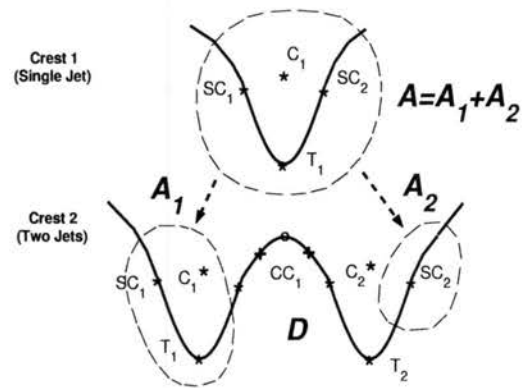


(d) Incidence angle  $90^\circ$

Figure 7.23: Reflection points on the 4-jet surface, at different incident angles.



(a) Synthesis based on 'B' scattering



(b) Synthesis based on 'D' scattering

Figure 7.24: Illustration of the difference between the two synthesis procedures.

between jet ( $T_2$ ) and cavity region ( $CC_1$ ) reflections is included in 'D' scattering. The N-jet surface scattering is synthesized by 'A+(N-1)D'. Figure 7.25 shows the 'A' scattering and the comparison of 'B' scattering with 'D' scattering. Both 'A' and 'D' scattering show the HH reduction, which indicates the effect of the side cavity region and the overlapped region. Figure 7.26 shows the comparison of the two types of synthesized results in the 3-, 4-, 5-, and 6-jet cases. Also showed is the corresponding MLFMA scattering.

The results of Figure 7.26 show that the 'B' and 'D' based synthesis give the exact same VV scattering, and have good agreement with MLFMA results. This again shows that the VV scattering is not affected by the cavity regions. The 'B' based synthesized HH scattering is over 20 dB greater than the MLFMA results in all cases. The 'D' based HH scattering agrees with MLFMA scattering when incidence angle is less than  $66^\circ$ . At the larger incident angles, the destructive HH interference is predicted, but with poor accuracy. This shows that multiple interactions occur with this surface, preventing the use of any synthesis procedure.

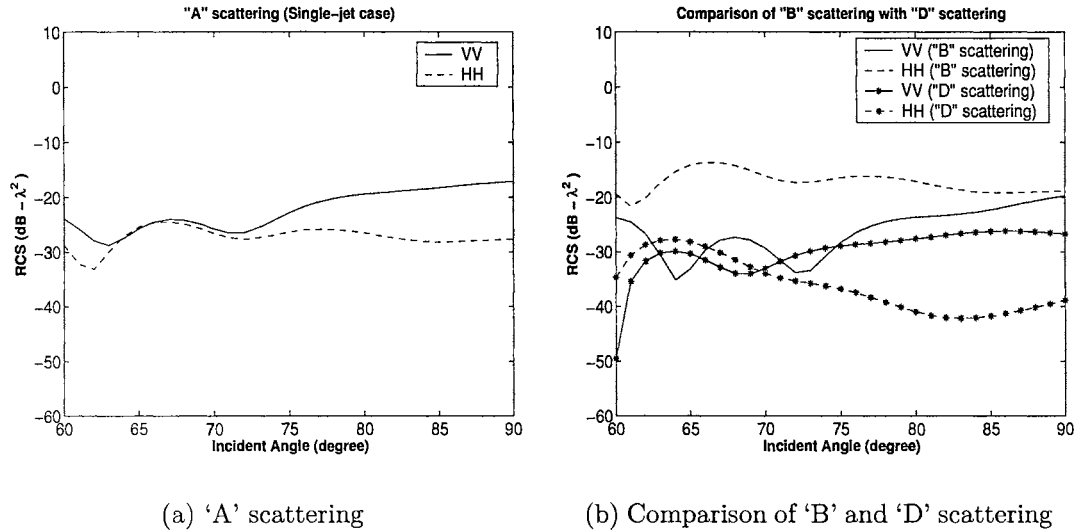
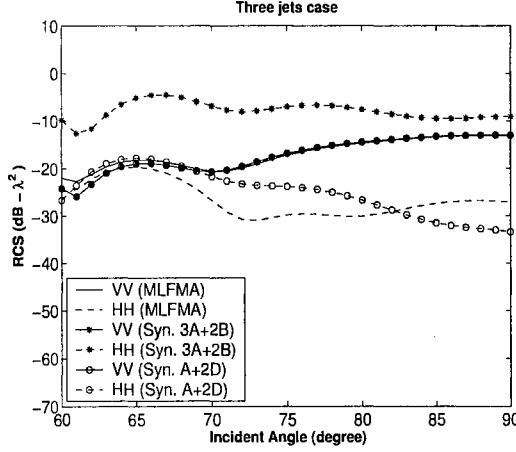
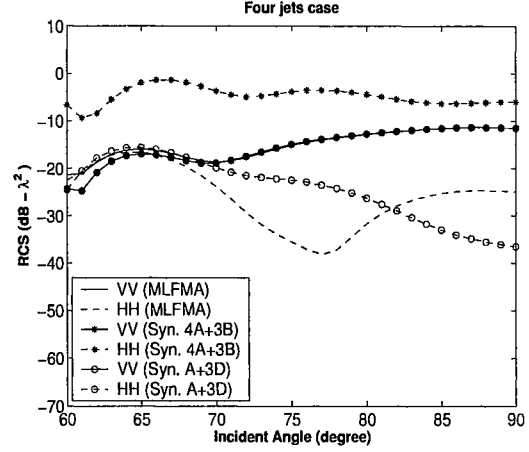


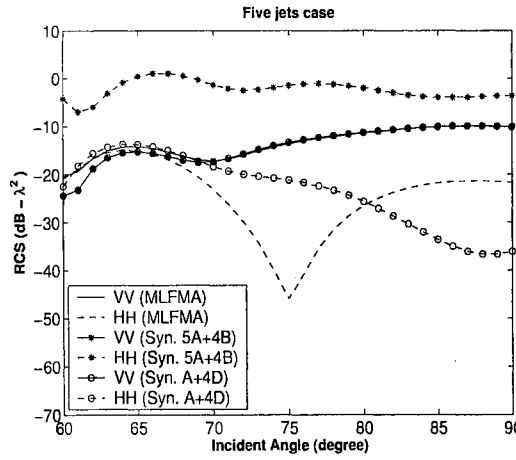
Figure 7.25: Scattering from section A, B, and D respectively.



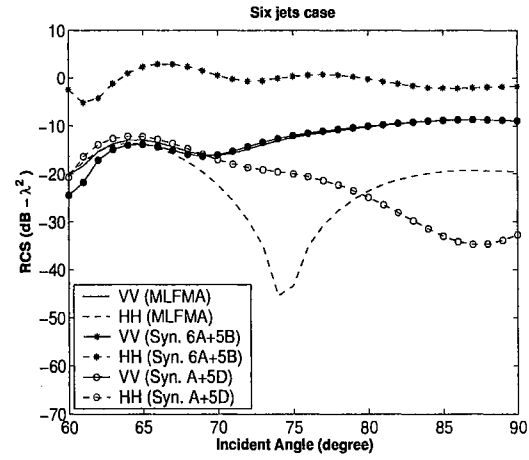
(a) Three-jet case



(b) Four-jet case



(c) Five-jet case



(d) Six-jet case

Figure 7.26: Comparison of ‘B’ and ‘D’ based synthesized scattering with MLFMA scattering.

## 7.6 Scattering from Multi-jet Surfaces with Random-roughness Crests

In this section, two surfaces that have more random multiple jets are examined. The random jets are formed by using different reference profiles at both each jet center and at the center of each cavity region between two adjacent jets. To ease the surface generation, the surfaces are symmetric in the azimuthal dimension. One of these



surfaces is shown in Figure 7.27 (d). It has 7 different jets, with reference profiles 18, 17, 17.5 and 16.5 respectively at the center of each. The concave regions next to those jets are formed with profiles 16.5, 16.5, 16 and 15.5 at the center, respectively. Parts (a), (b), and (c) show surfaces generated with fewer jets. The surface in part (a) has only one jet pair, the surface in part (b) has two jet pairs, and the surface in part (c) has three jet pairs.

Figure 7.28 shows the RCS of these surfaces. Part (a) shows the scattering from the partial surface of Figure 7.27 (a). When the incident angle is less than  $65^\circ$ , the scattering is different from the other three cases in Figure 7.27 (b) through (d). When incident angle ranges from  $65^\circ$  to about  $80^\circ$ , the scattering from all four surfaces shows

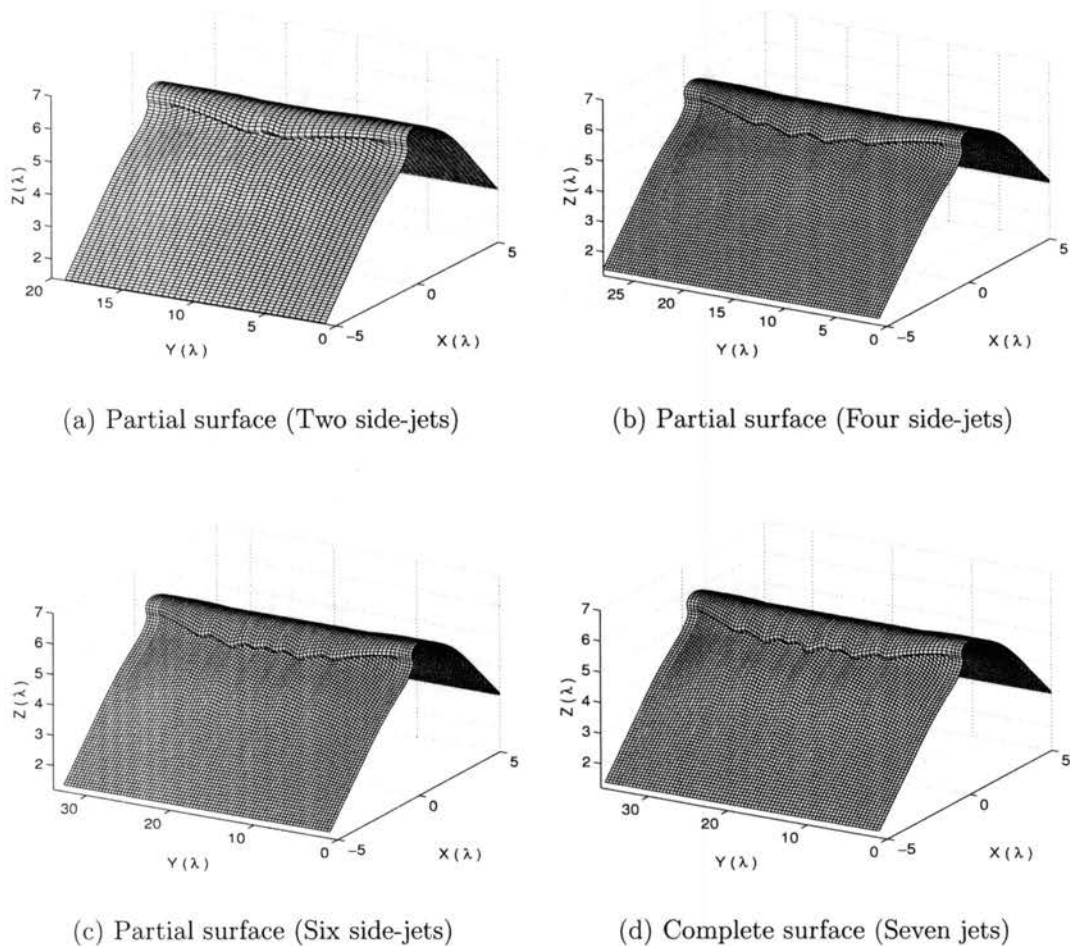


Figure 7.27: Random-roughness crest surfaces (smooth)

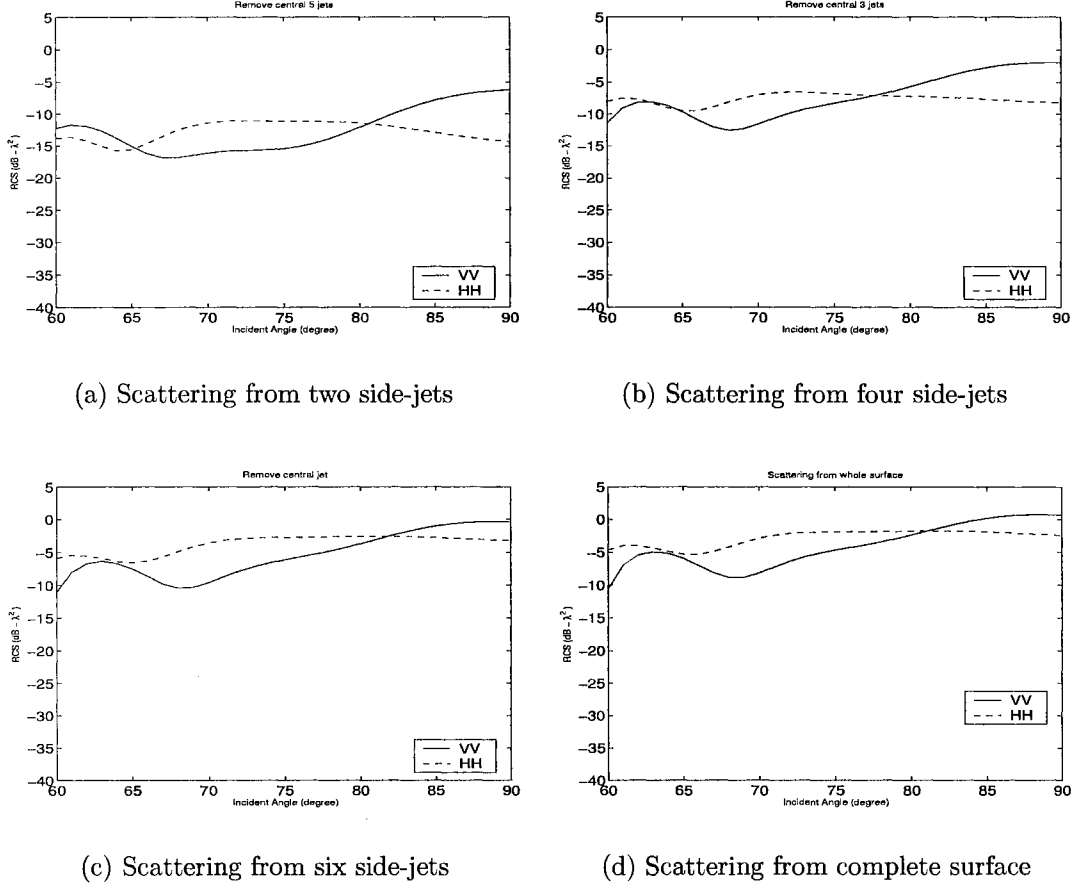
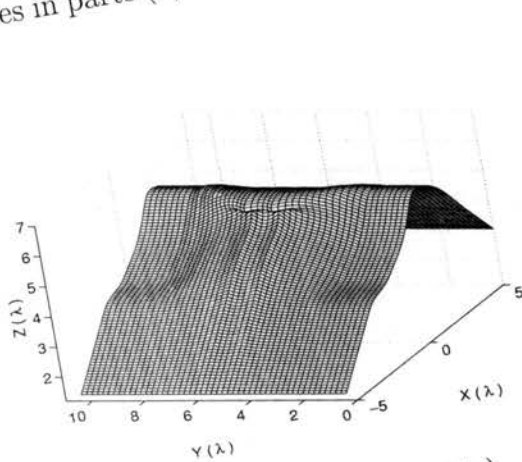


Figure 7.28: RCS of scattering from random-roughness crest surfaces (smooth)

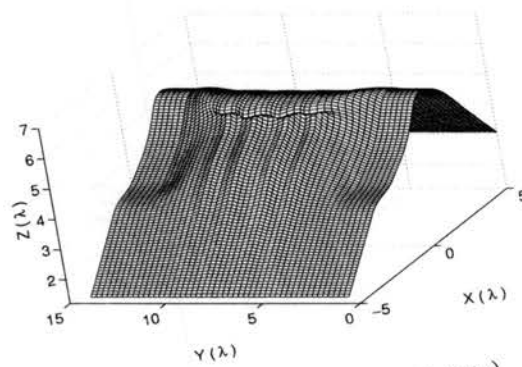
a weak super event ( $HH > VV$  about 3 to 5 dB). When the incident angle exceeds  $80^\circ$ , VV exceeds HH in all four cases. Generally, the RCS fluctuation in each case is less than 5 dB. The overall scattering level increases as the number of jets increases. No strong destructive interference appears in any of these four cases. This results because the variation between the jets is not extreme, and most of the concave cavity regions are shadowed by the bigger jetting area. Significant VV and/or HH cancellation, therefore, is not established.

Figure 7.29 shows another series of random-roughness crest surfaces. The surface in part (e) of this figure is the final surface, which uses reference profiles 18, 16, 17, 15 and 14 at its jet centers (from center to side), and uses reference profiles 15, 15, 14, 13 at the cavity region centers next to the above jets. Figure 7.29 (f) shows the specular

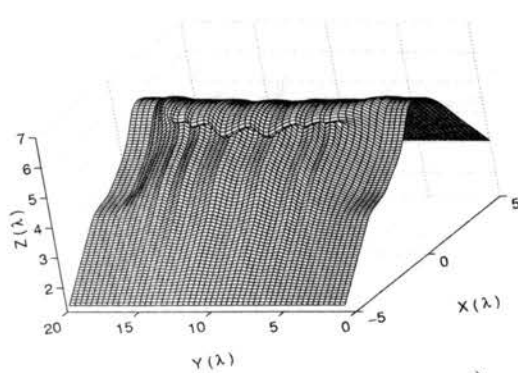
reflection points on this surface corresponding to the upwave looking direction. The surfaces in parts (a) through (d) illustrate the generation of this surface. The upwave-



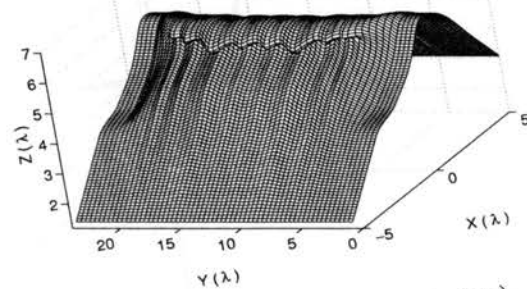
(a) Partial surface (Two side-jets)



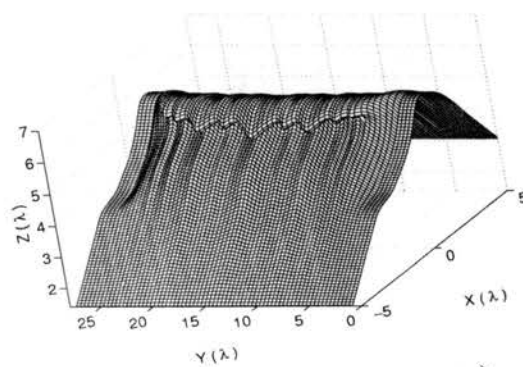
(b) Partial surface (Four side-jets)



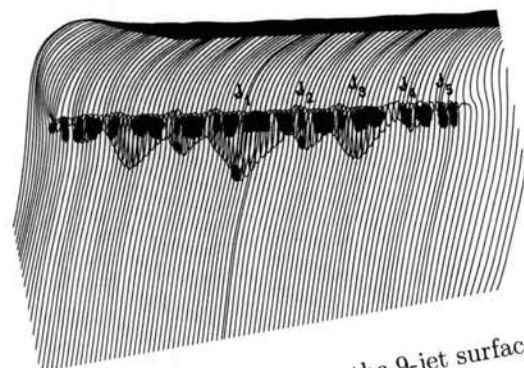
(c) Partial surface (Six side-jets)



(d) Partial surface (Eight side-jets)



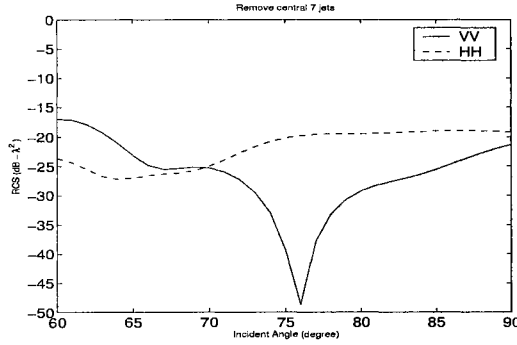
(e) Complete surface (Nine jets)



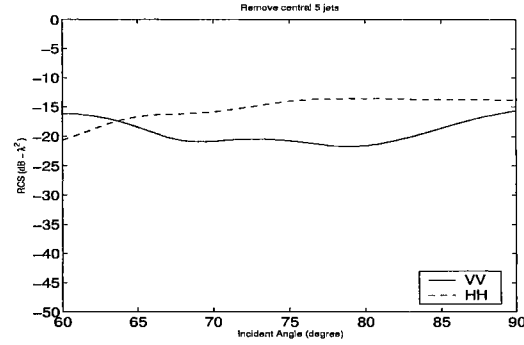
(f) Reflection points on the 9-jet surface

Figure 7.29: Random-roughness crest surfaces (rough)

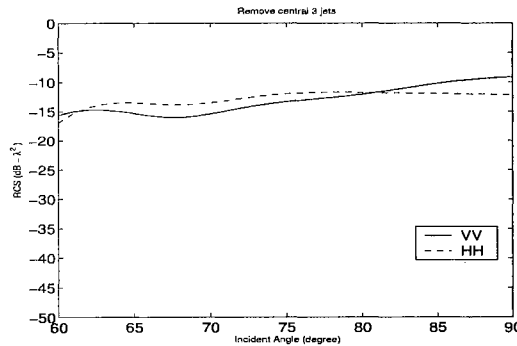
looking backscattering from these surfaces is shown in Figure 7.30. Parts (a) to (e) are the scattering corresponding to the surfaces of Figure 7.29, parts (a) to (e). Part (f) is the scattering from only the central jet, which was found from the difference of the vector scattered fields from the surfaces in parts (e) and (d).



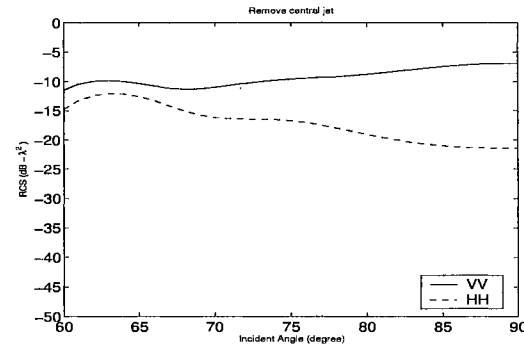
(a) Scattering from two side-jets



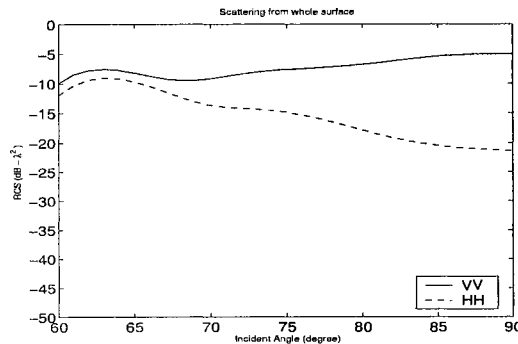
(b) Scattering from four side-jets



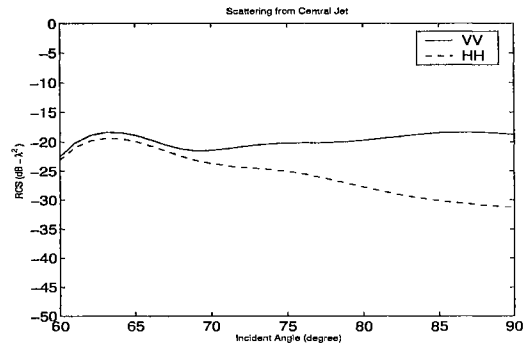
(c) Scattering from six side-jets



(d) Scattering from eight side-jets



(e) Scattering from complete surface



(f) Scattering from the central jet

Figure 7.30: RCS of scattering from random-roughness crest surfaces (rough)

The RCS variation shown in parts (a) to (e) of Figure 7.30 exhibits a clear transition from strong VV destructive interference to strong HH destructive interference as jets are added. For the two side jets case of part (a), the scattering is due to reflection from the convex jetting areas and the concave cavity regions under the jets, giving the VV interference null. The reflection points between and outside of the two jets have little effect. As jets are added in cases (b) through (e), the new jets themselves do not lead to VV destructive interference due to the shadowing of the cavity. The back-reflection from the new jets overwhelms the interference nulls in the original 2-jet scattering. However, the cavity regions between the jets provide the concave reflection point in the plane of the electric field needed to give the HH destructive interference.

As more jets are added in the central area, more reflection points appear on the convex jets and in the overlapped cavity regions between adjacent jets. The reflection from the jetting areas overwhelms the reflection from the previously existing reflection points on the concave areas. The HH interference null appears as concave reflection points appear in the azimuthal direction. The central jet does not strongly affect the backscattering because the reflection from its jetting area is not significantly different from that from the other jets, and the concave section under this jet is totally shadowed.

Note that the fluctuation of the VV and HH backscattering is especially significant at larger incident angles. This is because more reflection points in concave cavity regions may move out of shadowing and become visible as the incidence approaches grazing. Thus more reflections from the concave regions contribute the destructive interference. The jets in the surfaces of Figure 7.29 are considerably rougher than those in Figure 7.27. More reflection points in the concave regions of Figure 7.29 are visible, especially at large incident angles. Therefore, the interference of the reflections from these regions become significant, which leads to stronger scattering variation.

# Chapter 8

## Summary and Conclusions

In this paper, analytical models and numerical techniques to model the electromagnetic scattering from breaking water wave crests have been investigated. In particular, implementations of a 2-D hybrid MM/GTD and 3-D multilevel fast multipole algorithm numerical scattering models were reviewed in detail. A test analysis of the scattering from a flat plate was used to confirm the validity of the numerical models. The numerical techniques were then applied to test surfaces based on the LONGTANK series of the time history of a plunging breaker wave. 3-D test surfaces were formed by azimuthally aligning the individual 2-D LONGTANK crests and interpolating between them to give a continuous surface. The 3-D radar cross-sections were computed using MLFMA. The 3-D extended geometrical optics (EGO) model was able to model the basic scattering mechanism for the simplest test cases. With the LONGTANK profile based test surfaces, the EGO model provided a reasonable prediction of the backscattering before the jet was fully developed, but the model failed when cavity region was shadowed by the developed jetting. A synthesis of the 3-D RCS from the individual 2-D profiles was less accurate due to the azimuthal curvature of the wave.

Both the off-axis backscattering and the bistatic scattering from several 3-D single-jet test wave crest surfaces was found. The scattering variation associated with the

movement of the reflection points in azimuth demonstrated different scattering mechanisms associated with the crest jet features. There was no significant destructive interference in the backscattering from surfaces early in the breaking since the quasi-specular reflection points on the crest have large radii of curvature. Interference nulls formed in both monostatic and bistatic VV scattering from a surface formed near the center of the breaking. The VV null resulted from the destructive interference of the reflections from the convex jetting area and the concave cavity region under the jet, provided that the surface radii of curvature was somewhat smaller than the electromagnetic wavelength. This scattering mechanism was first identified by West [2] in a 2-D backscattering analysis of LONGTANK waves. As the azimuthal angle of the illumination was changed, the specular reflection points on the wave moved from the center of the jet/cavity region to the wave side, thereby changing the magnitude and incidence angle of the null. The scattering from a surface late in the breaking with a fully formed crest showed that the VV destructive interference was affected by the shadowing of the cavity underneath the jet. A VV interference null did not occur when looking upwave since the concave reflection point in the cavity was shadowed, and could not interfere with the direct jet scattering. As the incidence was moved in azimuth, the concave region became visible. Reflections from this region then interfered with those from convex jet, and the VV null therefore formed. With the most extreme jetting, the null did not form until the azimuth extended to  $8^\circ$ . On the other hand, a significant HH interference null was observed when the azimuthal angle was  $13^\circ$ . This is the first time that an HH destructive interference null has been observed. The mechanism of this HH destructive interference is essentially the same as the one that more commonly leads to VV destructive interference. The wave jet forms reflection points where the surface is concave in the plane of the electric field at one point and convex in the plane of the electric field at another point. The radii of curvature at these points was small compared to the electromagnetic wavelength,

so all conditions needed to give destructive interference were met.

Multiple-jet 3-D test surfaces were also synthesized using the interpolated LONG-TANK profiles. The test surfaces include various crest features such as the duplication of individual jet structures, small, medium, and rough ripples in the azimuthal direction along the jet, and random roughness crest structure. A numerical computation of the backscattering from these test surfaces was performed. Two scattered-field coherent synthesis schemes were designed to compare the effect of the reflection from the cavity regions between jets, and to identify the multiple interaction that occurs between individual jet features.

Both the VV and HH destructive interference phenomena were observed in various multiple-jet cases. The mechanisms of the destructive interference are similar to those that occurred in the single-jet cases described above. The actual interference therefore strongly depends upon the crest features. In particular, the structures of both the jet maxima and the cavity between adjacent jets are important. Reflections from these areas interfere each other, thus leading to interference effects that may be constructive or destructive, strong or weak, depending upon the exact geometry. The jet shadowing plays a critical role in backscattering from the multiple-jet wave crests. The larger jetting areas may shadow the reflections from cavity regions both below the jets or between adjacent jets. When the reflections from cavity regions are totally shadowed, significant interference does not occur. In the case of the most complex wave crest with random roughness, the cavities are only partially shadowed, and the shadowing reduces as the incidence approaches grazing. Because of this, the interference effects vary, usually becoming stronger, as the incident angle increases.

In the case of the surfaces generated by identically duplicating a single jet structure multiple times, the backscattering may depend linearly upon the number of jets included, provided that the reflections from the cavity regions between adjacent jets do not introduce significant interference. The dependence fails when the reflections



from the cavity regions between adjacent jets are significant, which usually was accompanied by an HH null formed by the destructive interference in the azimuthal dimension.

# Bibliography

- [1] J. C. West and Z. Zhao, "Electromagnetic modeling of multipath scattering from breaking water waves with rough faces," *IEEE Trans. Geosci. Remote Sens.*, vol. 40, pp. 583–592, Mar. 2002.
- [2] J. C. West, "LGA sea-spike backscattering from plunging breaker crests," *IEEE Trans. Geosci. Remote Sens.*, vol. 40, pp. 523–526, Feb. 2002.
- [3] Y. Liu and W. J. Pierson, "Comparisons of scatterometric models for the am on ers-1: the possibility of systematic azimuth angle biases of wind speed and direction," *IEEE Trans. Geosci. Remote Sens.*, vol. 32, pp. 626–35, 1994.
- [4] S. V. Nghiem, F. K. Li, and G. Neumann, "The dependence of ocean backscatter at ku-band on oceanic and atmospheric parameters," *IEEE Trans. Geosci. Remote Sens.*, vol. 35, pp. 581–600, 1997.
- [5] Y. Quilfen, B. Chapron, T. Elfouhaily, K. Katsaros, and J. Tournadre, "Observation of tropical cyclones by high-resolution scatterometry," *J. Geophys. Res.*, vol. 103, pp. 7767–86, 1998.
- [6] S. Austin and W. J. Pierson, "Mesoscale and synoptic-scale effects on the validation of nscat winds by means of data buoy reports," *J. Geophys. Res.*, vol. 104, pp. 11 437–47, 1999.
- [7] W. J. Plant, "Effects of wind variability on scatterometry at low wind speeds," *J. Geophys. Res.*, vol. 105, pp. 16 899–910, 2000.
- [8] F. T. Ulaby, R. K. Moore, and A. K. Fung, *Microwave Remote Sensing: Active and Passive*, vol. 2. Norwood, Massachusetts: Artech House, 1982.
- [9] D. B. Trizna, J. P. Hansen, P. Hwang, and J. Wu, "Laboratory studies of radar sea spikes at low grazing angles," *J. Geophys. Res.*, vol. 96, pp. 12529–12537, July 1991.
- [10] D. R. Lyzenga, A. L. Maffett, and R. A. Shuchman, "The contribution of wedge scattering to the radar cross section of the ocean surface," *IEEE Trans. Geosci. Remote Sens.*, vol. GE-21, pp. 502–505, Oct. 1983.
- [11] J. R. Duncan, W. C. Keller, and J. W. Wright, "Fetch and wind speed dependence of doppler spectra," *Radio Sci.*, vol. 9, pp. 808–819, 1974.

- [12] A. T. Jessup, W. C. Keller, and W. K. Melville, "Measurements of sea spikes in microwave backscatter at moderate incidence," *J. Geophys. Res.*, vol. 95, pp. 9679–88, 1990.
- [13] W. J. Plant, "A model for microwave doppler sea return at high incidence angles: Bragg scattering from bound, tilted waves," *J. Geophys. Res.*, vol. 102, pp. 21,131–21,146, Sept. 1997.
- [14] L. B. Wetzel, "On microwave scattering by breaking ocean waves," in *Wave Dynamics and Radio Probing of the Ocean Surface* (O. M. Phillips and K. Hasselmann, eds.), pp. 273–284, New York: Plenum Press, 1986.
- [15] D. B. Trizna, "A model for Brewster angle damping and multipath effects on the microwave radar sea echo at low grazing angles," *IEEE Trans. Geosci. Remote Sens.*, vol. 35, pp. 1232–1244, Sept. 1997.
- [16] D. S. Kwoh, B. M. Lake, and H. Rungaldier, "Microwave scattering from internal wave modulated surface waves: A shipboard real aperture coherent radar study in the Georgia Strait experiment," *J. Geophys. Res.*, vol. 93, no. C10, pp. 12135–12248, 1988.
- [17] A. I. Kalmykov and V. V. Pustovoytenko, "On polarization features of radio signals scattered from the sea surface at small grazing angles," *J. Geophys. Res.*, vol. 81, pp. 1960–1964, Apr. 1976.
- [18] B. L. Lewis and I. D. Olin, "Experimental study and theoretical model of high-resolution radar backscatter from the sea," *Radio Sci.*, vol. 15, pp. 815–828, July 1980.
- [19] P. H. Y. Lee, J. D. Barter, K. L. Beach, C. L. Hindman, B. M. Lake, H. Rungaldier, J. C. Shelton, A. B. Williams, R. Yee, and H. C. Yuen, "X band microwave backscattering from ocean waves," *J. Geophys. Res.*, vol. 100, pp. 2591–2611, Feb. 1995.
- [20] K. D. Ward, C. J. Baker, and S. Watts, "Maritime surveillance radar- part 1: Radar scattering from the ocean surface," *IEE Proceedings*, vol. 137, pp. 51–62, Apr. 1990.
- [21] B. O. Werle, "Sea backscattering, spikes and wave group observations at low grazing angles," *Proceedings of the 1995 IEEE International Radar Conference*, pp. 187–195, May 1995.
- [22] A. Farina, F. Gini, M. V. Greco, and L. Verrazzani, "High resolution sea clutter data: Statistical analysis of recorded live data," *IEE Proceedings-Radar, Sonar, Navigation*, vol. 144, pp. 121–130, June 1997.
- [23] F. L. Posner, "Spiky sea clutter at high range resolutions and very low grazing angles," *IEEE Trans. Aerospace and Electronic Systems.*, vol. 38, pp. 58–73, Jan. 2002.

- [24] A. D. Rozenberg, D. C. Quigley, and W. K. Melville, "Laboratory study of polarized scattering by surface waves at grazing incidence: Part i wind waves," *IEEE Trans. Geosci. Remote Sens.*, vol. 33, pp. 1037–1046, July 1995.
- [25] A. D. Rozenberg, D. C. Quigley, and W. K. Melville, "Laboratory study of polarized microwave scattering by surface waves at grazing incidence: The influence of long waves," *IEEE Trans. Geosci. Remote Sens.*, vol. 34, pp. 1331–1342, Nov. 1996.
- [26] M. A. Sletten, J. C. West, X. Liu, and J. H. Duncan, "Radar investigations of breaking water waves at low grazing angles with simultaneous high-speed optical imagery," *Radio Sci.*, vol. 38, no. 6, 2003. doi:10.1029/2002RS002716.
- [27] F. T. Ulaby, R. K. Moore, and A. K. Fung, *Microwave Remote Sensing: Active and Passive*, vol. 3. Norwood, Massachusetts: Artech House, 1986.
- [28] S. O. Rice, "Reflection of electromagnetic wave from slightly rough surfaces," *Commun. Pure Appl. Math.*, vol. 4, pp. 351–378, Aug. 1951.
- [29] J. W. Wright, "A new model for sea clutter," *IEEE Trans. Antennas Propagat.*, vol. AP-16, pp. 217–223, Mar. 1968.
- [30] V. I. Tatarskii and V. V. Tatarskii, "Statistical description of rough-surface scattering using the quasi-small-slope approximation for random surfaces with a gaussian multivariate probability distribution," *Waves Random Media*, vol. 4, p. 191, 1994.
- [31] S. T. McDaniel, "A small-slope theory of rough surface scattering," *J. Opt. Soc. Am., A*, vol. 95, pp. 1859–64, 1994.
- [32] J. Shen and A. A. Maradudin, "Multiple scattering of waves from random rough surfaces," *Phys. Rev.*, vol. 22, pp. 4234–40, 1980.
- [33] D. Winebrenner and A. Ishimaru, "Investigation of a surface field phase perturbation technique for scattering from rough surfaces," *Radio Sci.*, vol. 20, pp. 161–170, Mar. 1985.
- [34] D. Winebrenner and A. Ishimaru, "Application of the phase-perturbation technique to randomly rough surfaces," *J. Opt. Soc. Am., A*, vol. 2, pp. 2285–94, 1985.
- [35] R. M. Fitzgerald and A. A. Maradudin, "A reciprocal phase-perturbation theory for rough-surface scattering," *Waves Random Media*, vol. 4, pp. 275–96, 1994.
- [36] C. H. Chan, S. H. Lou, L. Tsang, and J. A. Kong, "Electromagnetic scattering of waves by random rough surface: a finite-difference time-domain approach," *Microwave Opt. Tech. Lett.*, vol. 4, pp. 355–9, 1991.

- [37] K. Pak, L. Tsang, L. Li, and C. H. Chan, "Combined random rough surface and volume scattering based on monte carlo simulations of solutions of maxwell's equations," *Radio Sci.*, vol. 28, pp. 233–8, 1993.
- [38] K. S. Lrause, S. H. Lou, L. Tsang, and C. H. Chan, "Application of the finite element method to monte carlo simulations of random rough surface scattering with neumann boundary conditions," *Microwave Opt. Tech. Lett.*, vol. 4, pp. 255–8, 1991.
- [39] S. H. Lou, L. Tsang, and C. H. Chan, "Application of the finite element method to monte carlo simulations of scattering of waves by random rough surfaces: Penerable case," *Waves Random Media*, vol. 1, pp. 287–301, 1991.
- [40] A. K. Fung, M. R. Shah, and S. Tjuatja, "Numerical simulation fo scattering from three-dimensional randomly rough surfaces," *IEEE Trans. Geosci. Remote Sens.*, vol. 32, pp. 986–94, 1994.
- [41] S. H. Lou, L. Tsang, C. H. Chan, and A. Ishimaru, "A monte carlo simulation of scattering of waves by a random rough surface with the finite element method and the finite difference method," *Microwave Opt. Tech. Lett.*, vol. 3, pp. 150–4, 1990.
- [42] S. H. Lou, L. Tsang, C. Chan, and A. Ishimaru, "Application of the finite element method to mente carlo simulations of scattering of waves by random rough surfaces with the periodic boundary condition," *J. Electro. Waves Appl.*, vol. 5, pp. 835–55, 1991.
- [43] L. Li, C. H. Chan, L. Tsang, K. Pak, and S. H. Lou, "Monte carlo simulations and backscattering enhancement of random metallic rough surfaces at optical frequencies," *J. Electro. Waves Appl.*, vol. 8, pp. 277–93, 1994.
- [44] A. Bayliss, C. I. Goldstein, and E. Turkel, "On accuracy conditions for the numerical computation of waves," *J. computat. Phys.*, vol. 59, pp. 396–404, 1985.
- [45] R. Lee and A. C. Cangellaris, "A study of discretization error in the finite element approximation of wave solution," *IEEE Antennas Propagat. Mag.*, vol. 40, pp. 542–549, May 1992.
- [46] J. W. R. Scott, "Errors due to spatial discretization and numerical precision in the finite-element mentod," *IEEE Antennas Propagat. Mag.*, vol. 42, pp. 1565–1569, Nov. 1994.
- [47] T. Deveze, L. Beaulieu, and W. Tabbara, "A fourth-order scheme for the FDTD algorithm applied to maxwell's equations," in *IEEE AP-S Int. Symp. Dig.*, (Chicago, IL), pp. 346–349, July 1992.
- [48] C. W. Manry, S. L. Broschat, and J. B. Schneider, "Higher-order FDTD methods for large problems," *J. Appl. Comp. Electromagn. Soc.*, vol. 10, no. 2, pp. 17–29, 1995.

- [49] V. Rokhlin, "Rapid solution of integral equations of scattering theory in two dimensions," *J. Comput. Phys.*, vol. 86, pp. 414–439, June 1990.
- [50] R. Coifman, V. Rokhlin, and S. Wandzura, "The fast multipole method for the wave equation: A pedestrian prescription," *IEEE Antennas Propagat. Mag.*, vol. 35, pp. 7–12, June 1993.
- [51] C. C. Lu and W. C. Chew, "A fast algorithm for solving hybrid integral equation," *IEEE Proceedings-H*, vol. 140, pp. 455–460, Dec. 1993.
- [52] J. M. Song and W. C. Chew, "Multilevel fast-multipole algorithm for solving combined field integral equations of electromagnetic scattering," *Microwave Opt. Tech. Lett.*, vol. 10, pp. 14–19, Sept. 1995.
- [53] J. Song, C.-C. Lu, and W. C. Chew, "Multilevel fast multipole algorithm for electromagnetic scattering by large complex objects," *IEEE Trans. Antennas Propagat.*, vol. 45, pp. 1488–1493, Oct. 97.
- [54] M. F. Gyure and M. A. Stalzer, "A prescription for the multilevel Helmholtz FMM," *IEEE Antennas Propagat. Mag.*, vol. 5, pp. 39–47, July 1998.
- [55] E. Michielssen and W. C. Chew, "Fast integral equation solver using plane-wave basis representation along the steepest descent path," in *Proceedings of the 1995 URSI Radio Science Meeting*, (Newport Beach, CA), p. 301, June 1995.
- [56] V. Jandhyala, E. Michielssen, S. Balasubramaniam, and W. C. Chew, "A combined steepest decent-fast multipole algorithm for the fast analysis of three-dimensional scattering by rough surfaces," *IEEE Trans. Geosci. Remote Sens.*, vol. 36, pp. 738–747, May 1998.
- [57] E. Bleszynski, M. Bleszynski, and T. Jaroszewicz, "A fast integral equation solver for electromagnetic scattering problems," in *IEEE AP-S Int. Symp. Dig.*, (Seattle, WA), pp. 416–419, June 1994.
- [58] J. W. J. Pierson and L. Moskowitz, "A proposed spectral form for fully developed wind seas based on the similarity theory of s. a. kitaigorodskii," *J. Geophys. Res.*, vol. 69, no. 24, pp. 5181–5190, 1964.
- [59] R. M. Axline and A. K. Fung, "Numerical computation of scattering from a perfectly conducting slightly rough surface," *IEEE Trans. Antennas Propagat.*, vol. AP-26, pp. 482–488, May 1978.
- [60] G. N and S. E, "Monte carlo calculation for electromagnetic-wave scattering from random rough surfaces," *Phys. Rev. Lett.*, vol. 52, pp. 1798–801, 1984.
- [61] K. Pak, L. Tsang, and C. H. Chan, "Backscattering enhancement of electromagnetic waves from two-dimensional perfectly conducting random rough surfaces based on monte carlo method," *J. Opt. Soc. Am.*, vol. 12, pp. 2491–9, 1995.

- [62] P. Wang, Y. Yao, and M. P. Tulin, "An efficient numerical tank for non-linear water waves, based on the multi-subdomain approach with BEM.," *Int. J. Num. Meth. Fluids*, vol. 20, pp. 1315–1336, June 1995.
- [63] J. H. Duncan, V. Philomin, H. Qiao, and J. Kimmel, "Formation of a spilling breaker," *Phys. Fluids*, vol. 6, pp. 2560–2561, Aug. 1994.
- [64] R. Chen and J. C. West, "Analysis of scattering from rough surface at large incidence angles using a periodic-surface moment method," *IEEE Trans. Geosci. Remote Sens.*, vol. 33, pp. 1206–1213, Sept. 1995.
- [65] J. C. West, J. M. Sturm, and J.-S. Ja, "Low-grazing scattering from breaking water waves using an impedance boundary MM/GTD approach," *IEEE Trans. Antennas Propagat.*, vol. 46, pp. 93–100, Jan. 1998.
- [66] J. C. West and J. M. Sturm, "A hybrid MM/GTD numerical technique for lossy dielectric rough surface scattering calculations." Final Report for AFOSR Summer Faculty Research Program, Rome Laboratory, Hanscom AFB, 1995.
- [67] Z. Zhao, *Numerical Study of Electromagnetic Scattering from Three-Dimensional Water Waves*. PhD thesis, Oklahoma State University, School of Electrical and Computer Engineering, Stillwater, Oklahoma 74078, 2002.
- [68] Z. Zhao and J. C. West, "Two-scale analysis of lga scattering from a 3-d spilling breaker crest," in *Proceedings of the 2003 IEEE AP-S International Symposium*, (July, Ohio), pp. 388–391, 2003.
- [69] J. C. West, "Electromagnetic scattering from finite conductivity wind-roughened water surfaces," *Int. J. Remote Sens.*, vol. 20, no. 17, pp. 3445–3450, 1999.
- [70] J. C. West, "Integral equation formulation for iterative calculation of scattering from lossy rough surfaces," *IEEE Trans. Geosci. Remote Sens.*, vol. 38, pp. 1609–1615, July 2000.
- [71] J. M. Sturm and J. C. West, "Numerical study of shadowing in electromagnetic scattering from rough dielectric surfaces," *IEEE Trans. Geosci. Remote Sens.*, vol. 36, pp. 1477–1484, Sept. 1998.
- [72] Z. Zhao and J. C. West, "Resistive suppression of edge effects in mlfma scattering from finite conductivity surfaces," *IEEE Trans. Antennas Propagat.*, 2004. under review.
- [73] J. C. West, "Resistive treatment of edges in numerical LGA scattering from rough surfaces," in *Proceedings of the 2001 IEEE AP-S International Symposium*, (July 8–13, Boston, Massachusetts), pp. 505–511, 2001.
- [74] J. C. West and S.-J. Ja, "Two-scale treatment of LGA scattering from spilling breaker water waves," *Radio Sci.*, vol. 37, pp. 7–1 – 7–12, July 2002.

- [75] J. C. West, "Effect of shadowing on electromagnetic scattering from rough ocean-wave-like surfaces at small grazing angles," *IEEE Trans. Geosci. Remote Sens.*, vol. 35, pp. 293–301, Mar. 1997.
- [76] J. C. West, "Ray analysis of low-grazing scattering from a breaking water wave," *IEEE Trans. Geosci. Remote Sens.*, vol. 37, pp. 2725–2727, Nov. 1999.
- [77] C. A. Balanis, *Advanced Engineering Electromagnetics*. New York: Wiley, 1989.
- [78] D. Holliday, L. L. DeRaad, and G. J. St-Cyr, "Sea spike backscatter from a steepening wave," *IEEE Trans. Antennas Propagat.*, vol. 46, pp. 108–113, Jan. 1998.
- [79] L. B. Wetzel, "Electromagnetic scattering from the sea at low grazing angles," in *Surface Waves and Fluxes* (G. L. Geernaert and W. L. Plant, eds.), vol. II—Remote Sensing, pp. 109–171, Dordrecht, The Netherlands: Kluwer, 1990.
- [80] S. G. Hanson and V. U. Zavorotny, "Polarization dependency of enhanced multipath radar backscattering from an ocean-like surface," *Waves Random Media*, vol. 5, pp. 159–165, Jan. 1995.
- [81] W. J. Plant, "Microwave sea return at moderate to high incidence angles," *Waves Random Media*, vol. 13, pp. 339–354, Oct. 2003.
- [82] M. I. Skolnik, *Radar Handbook*. New York: McGraw-Hill., 1970.
- [83] M. A. Sletten and J. Wu, "Ultrawideband, polarimetric radar studies of breaking waves at low grazing angles," *Radio Sci.*, vol. 31, pp. 181–192, Jan. 1996.
- [84] M. A. Sletten, D. B. Trizna, and J. P. Hansen, "Ultrawideband radar observations of multipath propagation over the sea surface," *IEEE Trans. Antennas Propagat.*, vol. 44, pp. 646–651, May 1996.
- [85] J. C. West, J. M. Sturm, and M. Sletten, "Small grazing angle radar scattering from a breaking water wave: Demonstration of brewster angle damping," in *Proceedings of the 1996 International Geoscience and Remote Sensing Symposium*, (May 27–31, Lincoln, NE., USA), pp. 2207–2209, 1996.
- [86] D. E. Barrick, "Near-grazing illumination and shadowing of rough surfaces," *Radio Sci.*, vol. 30, pp. 563–580, May 1995.
- [87] D. A. McNamara, C. W. I. Pistorius, and J. A. G. Malherbe, *Introduction to the Uniform Geometrical Theory of Diffraction*. Boston: Artech House, 1990.
- [88] A. Ishimaru, *Wave Propagation and Scattering in Random Media Volume 2: Multiple Scattering, Turbulence, Rough Surfaces, and Remote Sensing*. San Diego, California: Academic Press, Inc., 1978.
- [89] P. Beckmann, "Shadowing of random rough surfaces," *IEEE Trans. Antennas Propagat.*, vol. AP-13, pp. 384–388, May 1965.



- [90] M. L. Sancer, "Shadow-corrected electromagnetic scattering from a randomly rough surface," *IEEE Trans. Antennas Propagat.*, vol. AP-17, pp. 577–585, Sept. 1969.
- [91] O. Airiau, A. Khenchaf, F. Daout, and J. Saillard, "Cross-polarized power returned from a random surface: Application to the rough sea surface," *OCEANS'95 MTS/IEEE 'Challenges of Our Changing Global Environment' Conference Proceedings.*, vol. 3, pp. 1523–27, Oct. 1995.
- [92] H. Mott, *Antennas for Radar and Communications: a polarimetric approach - Wiley Series in Microwave and Optical Engineering - Kai Chang, Series Editor.* New York: Wiley, 1992.
- [93] G. S. Brown, "Backscattering from a Gaussian-distributed perfectly conducting rough surface," *IEEE Trans. Antennas Propagat.*, vol. AP-26, pp. 472–482, May 1978.
- [94] S. L. Durden and J. F. Vesecky, "A numerical study of the separation wavenumber in the two-scale scattering approximation," *IEEE Trans. Geosci. Remote Sens.*, vol. 28, pp. 271–272, Mar. 1990.
- [95] J. T. Johnson, T. S. Robert, J. K. Kong, L. Tsang, and P. K., "A numerical study of the composite surface model for ocean backscattering," *IEEE Trans. Geosci. Remote Sens.*, vol. 36, no. 1, pp. 78–82, 1998.
- [96] J. C. West and B. S. O'Leary, "Numerical calculation of electromagnetic scattering from measured wind-roughened water surfaces," *Int. J. Remote Sens.*, vol. 19, pp. 1377–1393, May 10 1998.
- [97] E. I. Thorsos, "The validity of the Kirchhoff approximation for rough surface scattering using a Gaussian roughness spectrum," *J. Acoust. Soc. Am.*, vol. 83, pp. 78–82, Jan. 1988.
- [98] D. E. Barrick, "A review of scattering from surfaces with different roughness scales," *Radio Sci.*, vol. 3, 1968.
- [99] B. F. Kur'yanov, "The scattering of sound at a rough surface with two types of irregularity," *Sov. Phys. Acoust.*, vol. 8, pp. 252–7, 1963.
- [100] M. L. Burrows, "A reformulated boundary perturbation theory in electromagnetism and its application to a sphere," *Canadian Journal of Physics*, vol. 45, pp. 1729–1742, May 1967.
- [101] G. S. Brown, *A Study of Terrain Scattering Physics*. Rome Air Development Center, Feb. 1981.
- [102] A. Ishimaru and J. S. Chen, "Scattering from very rough metallic and dielectric surfaces: A theory based on the modified kirchhoff approximation," *Waves Random Media*, vol. 1, pp. 21–34, 1991.

- [103] D. Holliday, L. L. DeRaad, and G. J. St-Cyr, "Volterra approximation for low grazing angle shadowing on smooth ocean-like surfaces," *IEEE Trans. Antennas Propagat.*, vol. 43, pp. 1199–1206, Nov. 1995.
- [104] G. S. Brown, "Some asymptotic considerations in low grazing angle scattering from rough surfaces," in *Proceedings of the 1994 URSI Radio Science Meeting*, (University of Washington, Seattle, Washington), p. 153, June 19–24 1994.
- [105] A. G. Voronovich, *Wave Scattering from Rough Surfaces*. Berlin: Springer-Verlag, 1999.
- [106] A. Voronovich, "Small-slope approximation for electromagnetic wave scattering at a rough interface of two dielectric half-spaces," *Waves Random Media*, vol. 4, pp. 337–3678, July 1994.
- [107] E. Thorsos and S. L. Broschat, "A investigation of the small slope approximation for scattering from rough surfaces. part i. theory," *J. Acoust. Soc. Am.*, vol. 97, pp. 2082–2093, 1995.
- [108] S. L. Broschat and E. Thorsos, "A investigation of the small slope approximation for scattering from rough surfaces. part ii. numerical studies," *J. Acoust. Soc. Am.*, vol. 101, pp. 2615–2625, 1997.
- [109] A. G. Voronovich and V. U. Zavorotny, "Theoretical model for scattering of radar signals in  $k_u$ - and c-bands from a rough sea surface with breaking waves," *Waves Random Media*, vol. 11, pp. 247–269, 2001.
- [110] S. L. Broschat, "The phase perturbation approximation of rough surface scattering from a Pierson-Moskowitz sea surface," *IEEE Trans. Geosci. Remote Sens.*, vol. 31, pp. 278–283, Jan. 1993.
- [111] D. R. Voltmer, *Diffraction by Double Curved Convex Surfaces*. PhD thesis, The Ohio State University, 1970.
- [112] W. L. Stutzman and G. A. Thiele, *Antenna Theory and Design*, pp. 587–588. New York: Wiley, 2nd ed., 1998.
- [113] R. G. Kouyoumjian and P. H. Pathak, "A uniform geometrical theory of diffraction for an edge in a perfectly conducting surface," *Proc. IEEE*, vol. 62, pp. 1448–1461, Nov. 1974.
- [114] A. W. Glisson, "Electromagnetic scattering by arbitrary shaped surfaces with impedance boundary conditions," *Radio Sci.*, vol. 27, pp. 935–943, Nov. 1992.
- [115] T. B. A. Senior and J. L. Volakis, "Generalized impedance boundary conditions in scattering," *Proc. IEEE*, vol. 79, pp. 1413–1420, Oct. 1991.

- [116] J. C. West and J. M. Sturm, "A hybrid mm/gtd numerical technique for far-field scattering from impedance boundaries," in *IEEE Antennas and Propagation Society International Symposium*, (July 21–26, Hyatt Regency Hotel, Baltimore, MD), 1996.
- [117] R. Harrington, *Time-Harmonic Electromagnetic Fields*. New York: McGraw-Hill, 1961.
- [118] S.-J. Ja and J. C. West, "Mechanisms of scattering from spilling-breaker water waves," in *Proceedings of the Progress in Electromagnetic Research Symposium*, (July 5–14, Cambridge, Massachusetts), 2000.
- [119] W. D. Burnside, C. L. Yu, and R. J. Marhefka, "A technique to combine the geometrical theory of diffraction and the moment method," *IEEE Trans. Antennas Propagat.*, vol. AP-23, pp. 551–558, July 1975.
- [120] S. Rao, *Electromagnetic Scattering and Radiation of Arbitrarily-shaped Surfaces by Triangular Patch Modeling*. PhD thesis, University Mississippi, 1980.
- [121] S. M. Rao, D. R. Wilton, and A. W. Glisson, "Electromagnetic scattering by surfaces of arbitrary shape," *IEEE Trans. Antennas Propagat.*, vol. 30, pp. 409–418, May 1982.
- [122] Y. Oh and K. Sarabandi, "Improved numerical simulation of electromagnetic wave scattering from perfectly conducting random surfaces," *IEE Proc. – Microw. Antennas Propag.*, vol. 144, pp. 256–260, Aug. 1997.
- [123] J. C. West, "On the control of edge diffraction in numerical rough surface scattering using resistive tapering," *IEEE Trans. Antennas Propagat.*, vol. 51, pp. 3180–3183, Nov. 2003.
- [124] H. Kim and H. Ling, "On the application of fast wavelet transform to the integral-equation solution of electromagnetic scattering problems," *Microwave Opt. Tech. Lett.*, vol. 6, no. 3, pp. 168–173, 1993.
- [125] B. Z. Steinberg and Y. Leviatan, "On the use of wavelet expansions in the method of moments," *IEEE Trans. Antennas Propagat.*, vol. 41, pp. 610–619, May 1993.
- [126] R. L. Wagner and W. C. Chew, "A study of wavelets for the solution of electromagnetic integral equations," *IEEE Trans. Antennas Propagat.*, vol. 43, pp. 802–810, Aug. 1995.
- [127] W. C. Chew, J. M. Jin, C. C. Lu, E. Michielssen, and J. M. Song, "Fast solution methods in electromagnetics," *IEEE Trans. Antennas Propagat.*, vol. 45, no. 3, pp. 533–543, 1997.
- [128] P. Pirinoli, G. Vecchi, and L. Matekovits, "Multiresolution analysis of printed antennas and circuits: A dual-isoscalar approach," *IEEE Trans. Antennas Propagat.*, vol. 49, no. 6, pp. 858–873, 2001.

- [129] N. Soveiko and M. S. Nakhla, "Efficient capacitance extraction computations in wavelet domain," *IEEE Trans. Circuit and System - I*, vol. 47, no. 5, pp. 684–670, 2000.
- [130] G. Arfken, *Mathematical Methods for Physicists, Third edition*. New York: Academic Press, 1985.
- [131] M. Abramowitz and I. A. Stegun, *Handbook of Mathematical Functions, (Applied Mathematics Series)*. Cambridge, MA: National Bureau of Standards, 1972.
- [132] V. Rokhlin, "Diagonal forms of translation operators for helmholtz equation in three dimentions," *Applied and Computational Harmonic Analysis*, vol. 1, pp. 82–93, 1993.
- [133] R. L. Wagner and W. C. Chew, "A ray-propagation fast multipole algorithm," *Microwave and Optical Technology Letters*, vol. 7, pp. 435–438, July 1994.
- [134] L. Tsang, C. H. Chan, K. Pak, and H. Sangani, "Monte-carlo simulations of large-scale problems of random rough surface scattering and applications to grazing incidence with the BMIA/coanonical grid method," *IEEE Trans. Antennas Propagat.*, vol. 43, pp. 851–859, Aug. 1995.
- [135] R. L. Haupt and V. V. Liepa, "Synthesis of tapered resistive strips," *IEEE Trans. Antennas Propagat.*, vol. AP-35, p. 1217, Nov. 1987.
- [136] R. Barrett, M. Berry, T. F. Chan, J. Demmel, J. Donato, J. Dongarra, V. Eijkhout, R. Poza, C. Romine, and H. B. der Vort, *Templates for the Solution of Linear Systems: Building Blocks for Iterative Methods*. Philadelphia, PA: SIAM, 1994.
- [137] L. N. Trefethen and D. Bau, *Numerical Linear Algebra*. Philadelphia, PA: SIAM, 1997.
- [138] J. C. West and J. M. Sturm, "On iterative approaches for electromagnetic rough-surface scattering problems," *IEEE Trans. Antennas Propagat.*, vol. 47, pp. 1281–1288, Aug. 1999.
- [139] K. E. Atkinson and I. G. Graham, "Iterative solution of the linear systems arising from the boundary integral method," *SIAM J. Sci. Statist. Comput.*, vol. 13, pp. 694–722, 1992.
- [140] J.-F. Lee, R. Lee, and R. J. Burkholder, "Loop star basis functions and a robust preconditioner for efie scattering problems," *IEEE Trans. Antennas Propagat.*, vol. 51, no. 8, pp. 1855–63, 2003.
- [141] Z. Zhao and J. C. West, "Low-grazing-angle microwave scattering from a three-dimensional spilling breaker crest: A numerical investigation," *IEEE Trans. Geosci. Remote Sens.*, 2004. under review.

- [142] R. A. Ross, "Radar cross section of rectangular flat plates as a function of aspect angle," *IEEE Trans. Antennas Propagat.*, vol. 14, pp. 329–336, May 1966.
- [143] M. A. Losada, F. L. Martin, and R. Medina, *Wave Kinematics and Dynamics in Front of Reflective Structures*, ch. 12, pp. 282–310. New York: ASCE, 1995.
- [144] K. M. Siegel, "Far field scattering from bodies of revolution," *Appl. Sci. Res. Sec. B*, vol. 7, pp. 293–382, 1958.
- [145] V. G. Nebabin, *Methods and Techniques of Radar Recognition*. Boston: Artech House, 1995.
- [146] D. R. Wehner, *High-Resolution Radar (Second Edition)*. Boston: Artech House, 1995.

VITA

Yanzhong Li

Candidate for the Degree of

Doctor of Philosophy

Thesis: NUMERICAL INVESTIGATION OF MICROWAVE SCATTERING  
FROM BREAKING WATER WAVE CRESTS

Major Field: Electrical Engineering

Biographical:

Personal Data: Born in Shanxian, Shandong, the People's Republic of China,  
September 12, 1968, the son of Zunhe Li and Zongyu Yuan.

Education: Received Bachelor of Science and Master of Science degrees in Electrical Engineering from University of Electronic Science and Technology of China, Chengdu, China in July 1990 and March 1993, respectively. Completed the requirement for the Doctor of Philosophy degree in Electrical Engineering at Oklahoma State University in May 2005.

Professional Experience: Electronic Engineer at the East-China Scientific Instrument Institute from March 1993 to August 1997. Research Assistant at Department of Electronic Engineering, University of Electronic Science and Technology of China, September 1997 to December 2000. Research Assistant at School of Electrical and Computer Engineering, Oklahoma State University, January 2001 to December 2004.

Professional Memberships: Institute for Electrical and Electronics Engineers